Integrated high precision kinematic positioning using GPS and EGNOS observations

Knut Sauer (Dipl. Ing.)

A thesis submitted for the degree of Doctor of Philosophy of the University of London and
Diploma of the Membership of Imperial College London
Department of Civil and Environmental Engineering
Imperial College London, United Kingdom

July 2003

For all the patience with me,
special thanks to my wife Pia...

"Do not look upon this world with fear and
loathing. Bravely face whatever the gods offer."
Morihei Ueshiba, O-Sensei (1883-1969)

Abstract

Satellite positioning using GPS and to a limited extent GLONASS is now widespread within the civilian community. The main observable used for high precision position determination is the carrier phase. Carrier phase measurements are very precise but ambiguous because the whole number of cycles between the receiver antenna and the satellite is unknown and must be determined. Measurements from GPS satellites have been used for high precision position determination in real time in certain environments. However, for some applications, such as position determination in harsh engineering environments, there are disadvantages in just using data from GPS satellites alone. An example of this is due to obstruction of satellites.

Using fewer satellites and the poor geometry of the remaining visible satellites, can severely limit the performance of the system, e.g. integer ambiguities cannot be resolved quickly enough, and the accuracy, reliability, integrity and availability of the solution are reduced. A solution to this problem is to use additional data from other sources.

This research assesses the potential of using of both GPS and EGNOS (European Geostationary Navigation Overlay Service) carrier phase data, transmitted as part of the EGNOS System Test Bed (ESTB). Various issues involved in the integration of data from the two systems including computation of satellite coordinates and clock offset estimation are addressed. This is followed by a detailed discussion of an approach for the generation of double difference observables, ionospheric error estimation as applicable for the single-frequency observations transmitted by the EGNOS satellites, and the determination of integer ambiguities.

Ambiguity determination and ionospheric error parametrisation for medium ($<$ 100 km) and short-range ($<$ 1km) baseline lengths represent the core of the research presented in this thesis. Different algorithms have been implemented and successfully

tested with simulated and real data. The real data was captured using a set of Novatel Millennium/WAAS receivers. The algorithms for the Kalman filter based ionospheric error processing engine to determine a near real-time local ionospheric error model based on the dual frequency GPS data are described in detail. The final ionospheric error parametrisation is based on a new approach using a modified weighted biharmonic spline interpolation to take into account small-scale local and temporal changes in the ionosphere .

The final results show a by 5-10 % increase in the availability of reliable ambiguity determination and position determination accuracy in difficult environments, when GPS and EGNOS data is combined.

Acknowledgements

Table of contents

List of Figures

List of Tables

Chapter 1

Introduction

This chapter describes the general scope of the research carried out on the subject of combining Global Positioning System (GPS) and European Geostationary Navigation Overlay Service (EGNOS) observations for precise positioning and surveying. A high level background of operational aspects of Global Navigation Satellite Systems (GNSS) is given.

This is followed by an outline of the motivation for the research as gathered from initial experiments integrating data from GPS and EGNOS for single point positioning (SPP).

The relevant technical issues connected to the integration of EGNOS satellite data for high precision kinematic positioning are discussed briefly also. This is followed by the definition of the research objectives. Finally the chapter is concluded by the structure and outline of the thesis.

1.1   Background

The potential of high accuracy positioning and navigation using artificial satellites continues to be demonstrated world-wide. GPS is to date the main navigation and positioning space-based system and is already proving to be valuable both to military and civil users.

GPS was launched in the early eighties by the *United States Department of Defence (DoD)* mainly for military applications. The system achieved *Full Operational Capability (FOC)* in 1995 with a constellation of 24 satellites [FRNP, 1999].

Because of the shortcomings in the performance of the system as observed in operation and due to pressure from the civilian community, the system has continued to evolve. New activities have been initiated by the US government to improve the system's performance. GPS is now a joint military and civilian system under the operation of the United States Department of Defence (DoD) and United States Department of Transport (DoT).

The Russian equivalent to GPS is the *GLObalnaya NAvigatsionnaya Sputnikovaya Sistema (GLONASS)*[1]. The system is managed for the Russian Federation Government by the Russian Space Forces. It has two types of navigation signals: the *standard precision navigation signal* and the *high precision navigation signal*. Due to severe financial difficulties the number of satellites in the constellation has reduced significantly since FOC in was declared in 1996. Recent communications suggest an ambitious program for a more advanced system development [cf. WHPR, 2000a].

In the US, Europe and Asia, research and development activities are underway to realise civilian controlled systems, the so-called first and second-generation systems (GNSS-I and GNSS-II). In the USA, the *Wide Area Augmentation System (WAAS)* is now in the implementation stage. GNSS-I developments in Europe include the equivalent to WAAS, the *European Geostationary Navigation Overlay Service (EGNOS)* currently in the development and implementation phase. In Asia, the *Multifunctional Transport Satellite System (MTSAT)* programme is being developed by the Japanese. The major GNSS-II is the European *GALILEO* system currently in the definition stage representing GNSS-II.

GNSS-I are designed as *Spaced Based Augmentation Systems (SBAS)* to improve the general performance parameters (availability, accuracy, integrity, continuity) of GPS and GLONASS. The systems are based on geostationary communication satel-

---

[1]Russ. Global Navigation Satellite System

lites with additional navigation functionality.

GPS as the main satellite positioning system employs two fundamental observables for positioning and navigation, the *code-phase* (pseudo-ranges from code phase observations) and the *carrier-phase*. In this context the term *"pseudo"* is used to represent the clock bias contaminating the range measurement due to the lack of synchronisation between the satellite and the receiver time frame.

The robust and readily accessible but coarse pseudo-range is the basic observable for navigation and is a measure of the distance between the satellite at the time of transmission and the receiver at the time of reception of the signal. Measurements to at least 4 satellites enables the determination of the 3D position and time at a user location (cf. Figure 1.1).
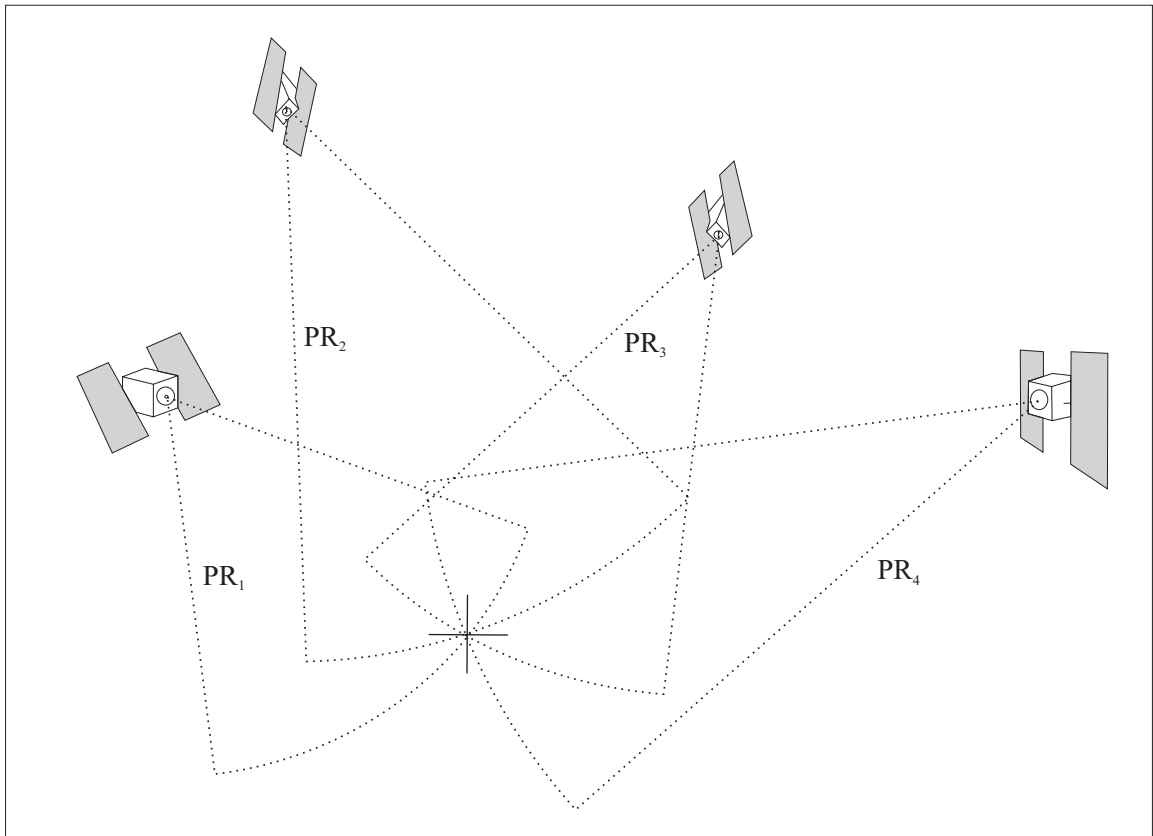
Figure 1.1: The receiver position is determined at the intersection of PR_1, PR_2 ... PR_n

Used in instantaneous stand-alone mode GPS is capable of providing positioning accuracy at the 10m level [cf. Lollock, 2001; DoD, 2001b]. Utilising differential techniques (i.e. in relative mode) should lead to significant more accurate positioning (better than 5 metres).

The level of accuracy achievable by stand-alone and differential techniques using the pseudo-range observable is adequate for many applications such as en-route navigation through to Category I (CAT I) precision approach (PA) phases of flight, mid-ocean to harbour vessel navigation and most land navigation requirements (cf. Table 1.1).

Table 1.1: Performance requirements for different applications (source FRNP [1999])

Field of application	Accuracy requirement
Aviation	
non-precision approach	300m
precision approach (CAT I)	17.1m/4.1m
precision approach (CAT II)	5.2m/1.7m
precision approach (CAT III)	4.1m/0.6m
Marine transport	
safety of navigation (large/small ships)	8-20m
recourse exploration	1-5m
engineering and construction	0.1-5m
Land transport	
route guidance	5-20m
accident and emergency responds	30m
public safety	10m
collision avoidance	1m
train control	2m
Engineering and surveying (relative/absolute accuracy)	
static survey	0.001m/0.002m
geodetic survey	0.001m/0.002m
kinematic survey	0.002m/0.005m

For applications requiring higher levels of accuracy (sub-metre and better) the more precise and accurate carrier-phase observable has to be used. Examples of such applications (cf. Table 1.1) include aircraft landing, engineering surveying including

structural deformation monitoring, geodynamic investigations and the determination of tide gauge benchmark positions for monitoring the mean sea level.

The carrier-phase observable is derived from the measurement of the difference between the phase of the signal arriving from the satellite, and the phase of the signal generated locally in the receiver. The direct measurement consists of a phase reading and the fractional part of the whole (integer) number of cycles in the range between the satellite and the receiver.

Unfortunately, the receiver has no knowledge of the number of whole wavelengths at *lock-on* time. However the receiver keeps counting the number of wavelengths to be added or subtracted as the *receiver-satellite* range changes. The whole number of cycles referred to as *integer ambiguity* must be resolved to determine the more precise range between the receiver and the satellite.

In general the determination of integer ambiguities itself is not a trivial task. A wide variety of different resolution techniques have been developed during the last twenty years [eg. Counselman and Gourevitch, 1981; Remondi, 1984, 1986, 1992; Dong and Bock, 1989; Goad, 1990; Euler and Goad, 1991; Mader, 1992; Blewitt and Lichten, 1992; Euler and Landau, 1992; de Jonge and Tiberius, 1994; Mevart, 1995; Rothacher and Mevart, 1996]. The complexity of such algorithms depends on the type of applications. Distinction between the following modes of applications is usually made:

- **Static mode:** Both the roving and reference receiver are kept for a certain time ($> 1h$) at one position.

- **Fast static mode:** The roving receiver is kept for several minutes ($\approx 20min$) at the one position, before moving on to the next.

- **On-the-fly:** The roving receiver moves constantly.

It is important to note that the complexity of the algorithms increases in the order above.

If carrier-phase measurements were error-free and the geometrical constellation perfect, then the determination of ambiguities would be trivial. However, various factors in the operational environment may result in ambiguity determination being a very difficult task. These factors are summarised below.

- Since the signal leaving the satellite travels through the Earth's atmosphere, different types of atmospheric refraction (i.e. tropospheric, ionospheric) and interference/reflections (i.e. multipath[2], intentional interference or jamming[3] and frequency interference[4]) may corrupt the signal and even render it unintelligible. If the level of unaccounted atmospheric contribution or noise exceeds the level of a few wavelengths, the task of finding the correct integer ambiguity becomes very difficult and sometimes impossible.

- The ambiguities often cannot be resolved quickly enough, for example in vehicle positioning where there are frequent obstructions leading to the occurrence of cycle slips (e.g. bridges, lampposts etc.). This is problematic for approaches reliant on cycle-slip free historical data.

- Other navigation system errors (e.g. receiver noise, remaining orbit and clock errors) exceed a tolerable limit and the required levels of reliability and/or integrity of the solution are not met, e.g. for *safety-of-life* critical applications such as precision approach and landing of aircraft.

- Because of satellite masking (i.e. satellite signals are blocked and not enough simultaneous observations are available) the matrices representing the observa-

---

[2]Multipath describes reflections due to surfaces in the vicinity of the receiving antennae.

[3]Intentional interference or jamming is the emission of sufficiently powerful radio frequency energy. This is either realised as emission of a signal close to the GPS spectrum, or if more sophisticated, as emission of a GPS like signal (civil receivers are particular vulnerable since there is no significant development of anti jamming technology in the civil sector).

[4]Interference from radio frequency (RF) transmitters emitting unwanted signal power in the frequency band as used by GPS (e.g. Ultra wide-band Radar and communications, Broadcast television at Very High Frequency (VHF), Personal Electronic devices, Mobile satellite services etc.)

tion equation become singular or badly scaled. This is often true in urban areas and on building sites.

While GPS can satisfy many requirements, its performance can be improved by both better error modelling and augmentation with other radio navigation systems (cf. Table 1.2). Table 1.2[5] gives a compilation of the most important ground and space based radio navigation and augmentation systems.

Furthermore there is a growing number of other positioning approaches, such as the use of traditional surveying, inertial techniques, dead-reckoning systems and map matching. These techniques are not considered in the research presented here.

This research has considered in detail various technical issues surrounding the combined use of data from GPS and EGNOS to improve GPS performance, particulary in harsh engineering and urban environments. The research also includes the modelling of ionospheric refraction based on dual-frequency observations transmitted by GPS satellites and applicable for single frequency observations. Furthermore the impact of additional EGNOS data has been studied in terms of rate of successful ambiguity determination and the final accuracy of the determined baseline vector.

The process as conducted in the research presented includes a preliminary study of relevant technical issues and the impact of additional observations as originated from EGNOS satellites. This is followed by the core research addressing the combined usage of GPS and EGNOS carrier phase observations for high precision kinematic positioning.

The following Section 1.2 summarises the research aims and objectives.

---

[5]For used acronyms in Table 1.2 the reader is referred to the List of Acronyms at Page 195ff.

Table 1.2: Different space and ground-based radio navigation/augmentation systems

System type	System accuracy/ comment
Ground Based Radio Navigation Systems and Augmentation Systems	
Loran C(Long RAnge Navigation)	2-D Navigation, uses accurately timed transmissions from three or more transmitting stations from which position may be computed.	best between 17-19m average around 150m
Chayca	Russian equivalent to Loran C	
Distance Measuring Equipment(DME)	Determination of positions using a two-way two-frequency algorithm to determine ranges and positions	Currently the main navigation tool for final phases of flight. Coverage and number of simultaneous users is limited.
TACAN	military (NATO)equivalent to DME	
Radio beacon DGNSS	Differential GPS (GNSS) corrections are transmitted via radio beacons to provide RTCM type corrections	This is an augmentation system for existing satellite navigation systems.
GSM/USTM	Positioning based on mobile phone technology based on three approaches (1) network based (2) handset based (3) hybrid	The positioning accuracy ≈ 50-100m. By 2005 all mobile phones in the US will be able to provide positions.
Space Based Radio Navigation Systems	
GPS	System based on a 24 satellite MEO constellation using CDMA. "One-way" ranges are determined and used to compute user location.	Stand-alone accuracy ≈ 10m. Significant improvements can be expected with recent modernisation activities.
GLONASS	Russian equivalent but using FDMA	Ageing constellation, i.e because of insufficient number of launches
GNSS II (Galileo)	Galileo is an European Initiative in the definition and development stage.	System performance is expected to be superior to GPS
Space Based Augmentation Systems	
EGNOS/WAAS/MTSAT	Provides mainly differential corrections and integrity information's for GPS/GLONASS. Based on geostationary orbiting satellite (i.e. EGNOS → Inmarsat AOR-E, IOR-W, Artemis)	Augmentation systems, positioning accuracy up to 1m.

1.2 Aims and Objectives

Given the background the aim of this research has been to carry out qualitative and quantitative evaluation of potential benefits of combining GPS and EGNOS code and carrier-phase observations for the purpose of high precision navigation and kinematic surveying.

The following objectives were formulated to achieve this aim.

- **Preliminary evaluation of technical issues:** This includes qualitative in-depth evaluation of technical issues as connected with the combination of observations from two different space based navigation systems, including the differences in spatial and temporal reference frames.

- **Integrated navigation and single point positioning:** Quantitative evaluation of the impact of combining GPS and EGNOS pseudo-range observations for navigation and single point positioning under simulated harsh engineering or urban conditions (i.e. high level of satellite masking).

- **Near real-time ionospheric modelling for kinematic positioning:** The modelling of ionospheric slant delays to correct the single frequency EGNOS carrier-phase observations is the core research topic. Initially, an in depth study of physical and mathematical properties of the Earth's ionosphere should be conducted. Subsequently existing ionospheric models should be studied and evaluated. The model to be developed should be based on an optimal use of all available ionospheric information including the utilisation of externally derived ionospheric models. The algorithms developed should also capture the temporal as well as the spatial distribution of a local ionosphere.

- **Evaluation of algorithms for ambiguity determination:** Finally, the research is aimed at the determination of kinematic 3-D positions at a very high level of accuracy and reliability. This involves reliable ambiguity determination. A number of existing algorithms for ambiguity determination should be imple-

mented and tested. A selection should be made for enhancement to be used to process integrated GPS/EGNOS data. Algorithms are to be tested for baseline length up to 100 km.

- **Validation:** The algorithms and the methodology developed should be tested using both simulated and real data. This should involve the development of a suitable model for software simulation to generate realistic data. Furthermore a field experiment should capture real GPS/EGNOS data.

1.3 Thesis outline

The introduction in Chapter 1 gives the background to the study, its aims and objectives and the structure of the thesis.

Chapter 2 discusses the technical parameters and performances of GPS and EGNOS. This includes ongoing and planned modernisation activities and the corresponding prospective gains in terms of navigation performance parameters. The key differences between both systems will be explained.

Chapter 3 gives the functional models for both the pseudo-range and the carrier-phase observables. Particular attention is paid to the physical and mathematical characteristics of the Earth's ionosphere and the corresponding impact on space based navigation systems.

Chapter 4 discusses the preliminary research to identify the potential benefit of combining GPS and EGNOS pseudo-range data for single point positioning and navigation.

Chapter 5 documents a new approach for the parametrisation of local ionospheric refraction using high quality code and carrier-phase observations.

Chapter 6 details the validation strategy based on simulated and real data. Different approaches for ambiguity determination have been adapted and applied. The results shows the superiority of the LAMBDA approach in particular for medium and

longer baselines. This chapter concludes with final results for baseline computation integrating EGNOS carrier-phase observations and the computed local ionospheric error model. The computation is based on the implementation of the LAMBDA method for ambiguity determination.

The thesis is finalised with conclusions and recommendations for further research activities in Chapter 7.

<div align="right">

Chapter 2

</div>

Global Navigation Satellite Systems *(GNSS)*

Space based satellite navigation systems are continuing to be recognised as important tools for world-wide navigation, positioning and surveying. The list of applications ranges from in-car navigation and fleet management, marine and air navigation, to precise surveying for deformation monitoring.

Several systems have been or are being developed with different purposes and intentions. This includes GPS, GLONASS, EGNOS and Galileo. The following chapter describes the current status, ongoing modernisation activities and development of various systems. GPS modernisation activities are covered in detail. System architectural and operational concepts are mentioned only briefly, because of extensive coverage in the available literature. For EGNOS the system-design as well as operational aspects are discussed in-depth. Finally the chapter summarises important and relevant aspects of GLONASS and GALILEO.

2.1 Global Positioning System *(GPS)*

The *NAVigation System with Time and Ranging Global Positioning System (NAVS-TAR GPS)* developed since 1973 is recognised as the major space based navigation system. Primarily developed for military use, it is now run jointly by the United

States Department of Defence (DoD) and the United States Department of Transport (DoT). The system reached its Full Operational Capability (FOC) in 1995, with a nominal constellation of 24 satellites. This enables any user worldwide to receive signals from at least four satellites at any time.

For in-depth descriptions of the various aspects of GPS, the reader is referred to the following documents. DoD [1995], DoD [2001b] and DoD [2001a] are official documents giving technical details and specifications on the GPS *Standard Positioning Service (SPS)*. Parkinson et al. [1996]; Seeber [1993]; Teunissen and Kleusberg [1998]; Leick [1995]; Hoffmann-Wellenhof et al. [1997] give scientific and engineering background of satellite positioning in general and of GPS in particular.

Since the system achieved FOC, there have been continued activities aimed at improving the navigation performance. This has arguably been driven by the shortcomings of the deployed system as observed in operation and pressure from the civilian community. The significant developments since 17th July 1995 (FOC) can be summarised as follows.

- Improvements within the ground segment resulting in better navigation data determination and prediction models. For example, the accuracy and quality of the satellite orbit and clock parameters have seen considerable improvement.

- The introduction of higher specification satellites (Blocks IIA and IIR) into the constellation.

- The removal of Selective Availability (SA) (dither and epsilon) with effect from 04.05 UTC on May 2000 [cf. WHPR, 2000b,a]

The impact of these developments has been to improve the system performance. For example the mean User Equivalent Range Error (UERE) budget has improved from $\sim$33 m (with SA) to $\sim$7.25 m during the period 1993 to 2000 [cf. DoD, 2001b; Lollock, 2001].

The system consists of the following segments:

- **Space segment:** This segment consists of the active satellite constellation described by the distribution of a number of spacecraft. Different types of spacecraft with different technical and performance parameters are currently in operation reflecting the developments in technology over the last ten years.

- **Control segment:** This segment includes facilities for orbit prediction, time keeping, system control and monitoring.

- **User segment:** This includes the Standard Positioning Service (SPS) and the Precise Positioning Service (PPS) with service definitions and service performance parameters. Furthermore it includes receiver technology and corresponding user relevant standards.

2.1.1 GPS segment descriptions

2.1.1.1 Space segment

The GPS space segment consists nominally of a constellation of 24 operational Block II satellites (Block II, IIA, and IIR). The spacecraft are placed in a near-circular orbit. Tables 2.1 and 2.2 show the status (as of 31.10.2001) of the GPS constellation and the signal characteristics respectively. The mean space vehicle life-span (Table 2.1) is based on operational experience (for those satellite types which have been in operation for a considerable period of time) and estimated life expectancy (for those satellite types either in the early years of operation or still to be launched) [cf. Lollock, 2001].

Table 2.1: The GPS Constellation as of November 2001

Orbital Configuration	
	Full Operation Capability (FOC)
	24 (28)[a] SVs
	6 orbital planes
	4 SVs per plane
	55 degree orbital inclination
	orbital radius of $\approx$26560 Km
Satellite distribution	
SV Types	**Mean SV Life-span (years)**
3 (4)[a] Block II SVs [1989[b]]	8.6 [based on operational experience]
16 (18)[a] Block IIA SVs [1990[b]]	10.6 [based on operational experience]
5 (6)[a] Block IIR SVs [1996[b]]	10 [estimated lifespan][c]

[a]Nominal Constellation plus SV's in additional positions as of 31.10.2001 in brackets
[b]Year of first launch
[c]cf. Lollock [2001]

Table 2.2: The current GPS signal characteristics

Definition and Characteristics	
Carrier Frequencies L1: 1575.42 MHz ($\hat{=}19.05cm$) L2: 1127.60 MHz ($\hat{=}24.45cm$)	Code Division Multiple Access (CDMA)
Code Frequencies (Gold code) C/A-Code: 1.023 MHz (on L1)	
Code Frequencies (pseudo random) P-Code: 10.23 MHz (on L1/L2)	Restricted to military use only it requires specially designed receiver devices
Navigation message	Ephemeris, SV clock parameters, ionospheric parameters, SV health
Artificial signal degradation	
Anti Spoofing (AS)	AS is the encryption of the P-Code to Y-Code, The AS keys are required from the DoT to access the P-Code signal

2.1.1.2 Ground segment

The GPS Control Segment (CS) consists of four major components: a Master Control Station (MCS), Backup Master Control Station (BMCS), four ground antennas, and six monitor stations. The MCS is located at Schriever Air Force Base, Colorado, and is the central control node for the GPS satellite constellation. The MCS is responsible for all aspects of constellation command.

In the event of a prolonged MCS outage, GPS operations can be moved to the contractor-owned BMCS located at Gaithersburg, Maryland. When required, personnel from the MCS are deployed at the BMCS within 24 hours. The BMCS is tested operationally approximately four times per year to ensure system capability.

The tracking data is transmitted to the MCS where extensive modelling algorithms are applied for orbit and clock prediction. Satellite ephemeris, clock parameters and other navigation data (ionospheric parameters, satellite health) are up-linked via Ground Antennas (GA) and S-Band (Meteo-Band) to the satellites. Locations and functionality are summarised in Table 2.3.

2.1.1.3 User segment

The system offers two different positioning services; the *Precise Positioning Service (PPS)*, and the *Standard Positioning Service (SPS)*. The Precise Positioning Service (PPS) is restricted mainly to military users. This is ensured via encryption using Anti Spoofing (AS). As this research is concerned with civil applications only, PPS is not considered any further.

The GPS SPS performance is specified by a number of navigation performance parameters including coverage, service availability, service reliability and accuracy [cf. DoD, 1995, 2001a]. These parameters are directly relevant for the user of GPS navigation and timing services. They are defined below:

- **Availability of Position Dilution of Precision (PDOP)**: The percentage

Table 2.3: GPS ground segment

Master Control Station	
Schriever Airforce base (MCS), Colorado and Gaitherburg, Maryland (Backup MCS)	•Routine satellite bus and payload status monitoring •Satellite maintenance and anomaly resolution •Management of SPS performance in support of all performance standards •Navigation data upload operations as required to sustain performance in accordance with accuracy performance standards •Prompt detection and response to service failures
Monitor Stations	
Colorado Springs, Hawaii, Cape Canaveral(FL), Ascension Islands, Diego Garcia, Kwajalein	•Near real-time ranging measurement data for MCS •Support of near continuous monitoring of constellation performance
Ground Antennas	
Diego Garcia, Kwajalein, Cape Canaveral(FL), Ascension	•Near real-time Telemetry, Tracking and Commanding •Interface between SVs and MCS

of time over a specified time interval that the Position Dilution of Precision (PDOP) is less than or equal to a specified value. The meaning of this value is discussed in detail in Section 4.1.

- **Service Reliability:** The percentage of time over a specified time interval that the instantaneous *Signal-in-Space (SIS)* SPS *User Range Error (URE)* is maintained within a specified reliability threshold at any given point within the service volume, for all healthy GPS satellites. The likelihood of the reliability threshold being broken is referred to as the Probability of Hazardously Misleading Information (HMI).

- **Service Availability:** The percentage of time over a specified time interval that the predicted position accuracy is less than a specified value for any point within the service volume.

- **Positioning Accuracy:** The statistical difference between position measurements and a surveyed benchmark for any point within the service volume over a specified time interval. Time Transfer Accuracy relative to the Coordinated Universal Time (UTC) maintained by the United States Naval Observatory (USNO) is the difference at a specified probability between user UTC time estimates and UTC_{UNSO} at any point within the service volume over a specified time interval.

Table 2.4 gives the currently specified SPS performance levels. The *"Accuracy Standard"* vectors refer to the SIS values only. Errors introduced due to the operational environment are not considered [cf. DoD, 2001b].

Table 2.4: Estimated current SPS performance levels. The *"accuracy standard"* values for the signal-in-space value only. Error introduced by operational environment are not included. [cf. DoD, 2001b]

PDOP Availability Standard	
	98% global position Dilution of Precision (PDOP) of 6 or less
	88% worst site PDOP of 6 or less
Service Availability Standard	
	99% horizontal (average location)
	99% vertical (average location)
	90% horizontal (worst-case location)
	90% vertical (worst-case location)
Service Reliability Standard	
	99.94% global average
	99.79% worst case single point average
SPS SIS URE Standard	
	6 m URE across the entire constellation [1σ]
Accuracy Standard	
Global Average	13 m 95%, 1σ horizontal error
	22 m 95%, 1σ vertical error
Worst Site Accuracy	36 m 95%, 1σ horizontal error
	77 m 95%, 1σ vertical error
Time Transfer Accuracy	40 nanoseconds 95% of the time

As the user is affected by the combination of all navigation errors, a good understanding of the operational environment is required. These components are not

directly related to the system operation and will be described in Chapter 3. The parameters as defined in DoD [2001b] provide the basic interface between the system operator and the system user.

Looking at the approach of specifying the service parameters reveals one major disadvantage. For example the values as given in Table 2.4 give only the order of magnitude the system is expected to achieve. *"Safety-critical"* applications such as civil aviation would require real-time or near-real-time measures (i.e. integrity monitoring). The GPS SPS currently does not include these measures. This functionality is expected to be performed by augmentation systems such as WAAS and EGNOS (cf. Section 2.2).

2.1.2 GPS - Modernisation

Because of the huge potential market for satellite navigation services, the end of the *"cold war"*, expected competition from the Galileo system and the technological developments in security related areas, the US government has put in place initiatives aimed at enhancing the performance of the system whilst still maintaining its crucial military role. Since 1996 several official announcements have been made in support of this.

Notable examples have been the *Accuracy Improvement Initiative (AII)* and the decision to stop degrading GPS accuracy. The AII is aimed at improving the navigation performance for the restricted *Precise Positioning Service (PPS)*. The main objective of the AII is to carry out an exhaustive analysis of the performance of the operational (ground) control system. This has already led to the upgrade of the *operational control segment (OCS)* to support the Block IIR *"autonav"* functionality [cf. Malys et al., 1997]. With the removal of the effects of SA, the AII is expected to benefit both PPS and SPS users.

The following sub-sections summarise the planned modernisation activities using information from official sources. The activities are described for the space, ground and user segment. This is concluded with a high level assessment of the impact of

the modernisation activities at system and user levels.

2.1.2.1 Space segment

Tables 2.6 and 2.5 show the planned satellite launch program for the GPS constellation and the signal characteristics respectively. According to the *Federal Radio Navigation Plan (FRNP), "the DoD will maintain a 24-satellite constellation. Replacement satellites will be launched on an expected failure strategy"* [FRNP, 1999].

Table 2.5: Planned Satellite Launch Activities

SV Types	Launch Time-Frame	Capabilities
6 unmodified Block IIR satellites	2000-2003	Current Capabilities (cf. Chapter 2)
12 modified Block IIR satellites	2003-2006	C/A code on the L2 carrier frequency -new military ME code on L1 and L2 carrier frequencies
13 Block IIF satellites	2005-2010	IIR Modified capabilities + 3rd civil frequency (L5)
11 Block IIF satellites	2007-2014	IIR Modified capabilities + 3rd civil frequency (L5)

To realise the proposed changes (see Table 2.5), new generations of satellites are currently under development. These are the modified Block IIR satellites with the capability for a second C/A code on L2 frequency and Block IIF satellites with the capability for the third civilian frequency L5 (for safety-critical applications). According to Lollock [2001] a progressive launch strategy will result in an *Initial Operational Capability (IOC)* for 2012 and FOC for 2014. For military applications the M_E code will be fully available in 2008.

Table 2.6: Planned modernisation of the GPS signals

Current Frequency Plan	Planned Frequency Plan (additional)	Capabilities
Carrier-Frequencies		
L1: 1575.42 MHz	Additional civilian Frequency	-6 dB higher power relative to L1
L2: 1227.60 MHz	L5: 1176.45 MHz	-20 MHz broadcast bandwidth
	"Safety-of-life" service frequency protection, ARNS -Band (IOC-2012 FOC-2014)	-Improved signal Cross-Correlation properties
Code-Frequencies (pseudo random)		
P-Code: 10.23 MHz (on L1/L2)	M_E Code (L1/L2) (IOC-2008 FOC-2010)	M_E Code designed to enhance system security and to improve anti-jamming
Code-Frequencies (gold code)		
C/A-Code: 1.023 MHz (on L1)	C/A Code on L2 (1127.60 MHz)	dual frequency ionospheric correction (improved UERE and better accuracy)
Navigation message		
	Ephemeris, SV clock parameters, ionospheric parameters, SV health	On L1 , L2 and L5

2.1.2.2 Control segment

To support the changes in the space segment and to exploit the enhancement to a full extent, changes in the ground (control) segment are necessary. These are mainly aimed at better tracking and derivation of navigation data (high accuracy and integrity). The planned activities include the following [Malys et al., 1997; FRNP, 1999; Lollock, 2001].

- Upgrade of Monitor Station and Ground Antennas with new digital receivers.

- Replacement of existing MCS mainframe computer with a distributed architec-

ture.

- Addition of the so-called Air Force Satellite Control Network.

- Enlargement of the tracking network by incorporating the *National Imagery and Mapping Agency (NIMA)* tracking stations.

- Addition of full Block IIR and IIF command and control functionality.

- Refinement and improvement of the navigation data algorithms and models, including an update of the MCS Kalman filter estimation process.

- A new upload strategy to reduce the orbit prediction error.

- Control capabilities for M-code and L5.

- Incremental software versions and hardware upgrades to support modernisation requirements.

The above activities are expected to improve the contribution to the *Navigation System Error (NSE)* by the control segment (i.e. orbit and clock errors) from 0.75 m to 0.4 m for zero age orbital and clock estimates. The corresponding figures for navigation data prediction after 24 hours are 1.5 m and 1.3 m.

2.1.2.3 User segment

Table 2.7 gives an estimate of the typical user range errors (m, 1σ) [cf. Sandhoo et al., 2000] as a result of the planned modernisation activities. Even after switching off selective availability it is clear that the modernisation from Block II through Block IIR to Block IIF will bring continued improvement on the expected performance (at least in terms of accuracy).

Other significant benefits will include the following.

- Better integrity through improvement in robustness of the system.

Table 2.7: Different stages of GPS modernisation and the expected impact to the user

Error Source	Without SA	+ two C/A (L1/L2)	+ two C/A (L1/L2) + OCS Mod.
Clock and Ephemeris Error [m]	2.30	2.30	1.25
Ionospheric Error [m]	7.00	0.01	0.01
Tropospheric Error [m]	0.20	0.20	0.20
Receiver measurement Error	0.60	0.60	0.60
Multipath [m]	1.50	1.50	1.50
Total UERE error budget [m]	7.50	2.80	2.00
Stand-alone Horizontal Accuracy [m] 95% (HDOP 3)	**22.5**	**8.5**	**6.00**

- Better real-time integer ambiguity resolution (e.g. tri-laning, three carrier phase ambiguity resolution). Therefore, real-time sub-centimetre accuracy for engineering and scientific applications should be more readily achievable with a higher reliability. The implications for the presented research are discussed in Section 2.3.1.2.

- Reduced transmission rates for DGPS corrections, because SA is set to zero.

- The feasibility of worldwide dual frequency aircraft navigation through the en-route to precision approach phases of flight.

2.1.3 GPS III programme

The GPS III programme has the objective to preserve and build on the successes of GPS by creating a new architecture according to the *GPS Operational Requirements Document* [cf. ORD, 1998]. It will assure the delivery of enhanced position, velocity, and timing signals, and related services to meet the requirements of the next generation of GPS users.

The *GPS III* programme includes an integrated space segment and control segment system that incorporates the *Nuclear Detonation Detection System (NUDET)*

and defines the Signal-in-Space (SIS) to user equipment interface.

The system should provide a best value solution with the flexibility to anticipate and respond to future military and civilian needs. The GPS III security infrastructure should provide user access to and protection of the entire system. It should facilitate the incorporation of additional mission capabilities (i.e. *Blue Force Tracking (BFT)*, *Search and Rescue (SAR)* missions, etc.).

The following time line has been given by Lollock [2001] for the realisation of the GPS III programme.

- ***System architecture and requirements development (2002-2004):*** A study between government and industry (Lockheed Martin, Boeing and Spectrum Astro) is being carried out to build a performance based set of technical requirements including the identification of potential architectural solutions.

- ***Public-industry interaction (2002-2004):*** To define a set of operational requirements in the civil sector has been identified through public/industry interaction.

- ***Architecture Definition (2004-2006):*** This is to carry out a first round of technical interchange between the partners. It should result in successful first *Preliminary Alternative Reviews* with Boeing and Lockheed. Multiple architectures will be identified within various frameworks i.e. - a GPS stand alone system - a GPS with augmentations and various levels of integration.

- ***Production and Deployment (2007 onwards):*** This includes the complete design, production and test of spacecraft, the in-orbit placement and the corresponding changes in the control segment. FOC is expected around 2020.

2.2   European Geostationary Navigation Overlay Service (EGNOS)

The development of EGNOS started in the early nineties. It is a joint effort of the *Tripartite Group (ETG)*, comprising the *European Space Agency (ESA)*, *European*

Community (EC) and EUROCONTROL.

The system has now undergone a definition and design phase and is currently (2002) in the implementation and validation phase. The system is expected to reach *FOC* in 2004[1].

EGNOS has been designed to improve the performance of GPS significantly. It will provide potential users with the following services.

- **GEO Ranging (R-GEO):** Transmission of GPS-like L1 band signals from 3 GEO satellites for the FOC phase to improve availability.

- **Integrity Channel (GIC):** Broadcast of GPS/EGNOS integrity information as required for civil aviation up to *CAT I precision approach.*

- **Wide Area Differential (WAD):** This includes the broadcast of differential corrections (i.e. slow clock, ionospheric and ephemeris corrections) and will enhance accuracy performance of GPS/GLONASS significantly.

The core service will be provided in the *European Civil Aviation Coverage (ECAC)* (cf. Figure 2.1) coverage area. As for GPS a subdivision into *Space, Control* and *User* segment has been applied.

2.2.1 Space segment

The EGNOS space segment is comprised of three Geostationary transponders integrated as part of the INMARSAT (Series 3) Atlantic Ocean Region East (AOR-E) and Indian Ocean Region (IOR) and the ESA Artemis spacecrafts (cf. Figure 2.1). The satellites are put in a geostationary or geosynchronous orbit of about 37000 km (cf. Section 3.3.4)

INMARSAT IOR-W(21.5^{o}E) and INMARSAT AOR-E(-15.5^{o}W): The spacecraft (F1 and F2 series) were launched in August 1996 were jointly built

---

[1]Source: European Space Agency (ESA) - EGNOS programme; http://www.esa.int/egnos
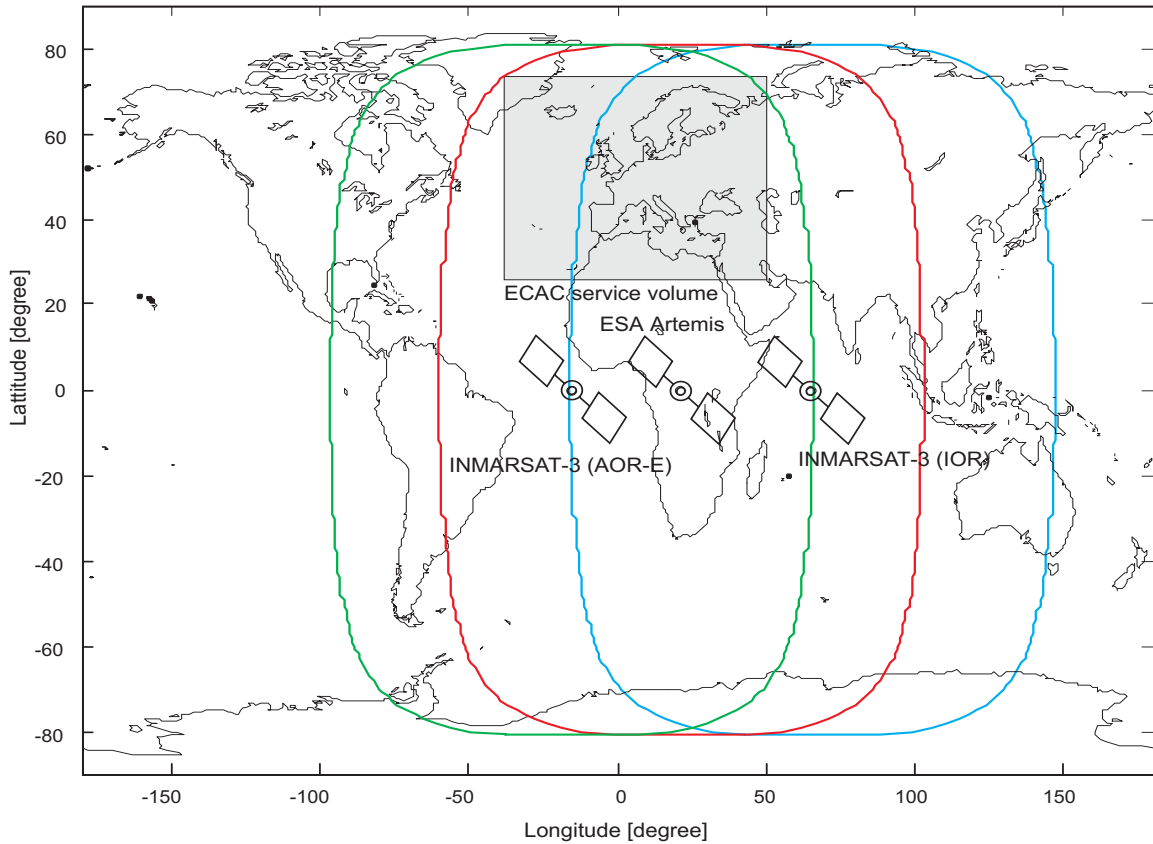
Figure 2.1: EGNOS/INMARSAT-3 Satellite coverage and ECAC-service volume

by *Lockheed Martin Astro Space* (now Lockheed Martin Missiles & Space) in the USA and the European company *Matra Marconi Space* (now Astrium). The former was responsible for the basic spacecraft, whereas the latter developed the communications payload.

The F1 spacecraft was launched by Atlas 2A carrier rocked from Cape Canaveral and the F2 spacecraft by a Proton carrier rocked from Tyuratam (Baikonur Cosmodrome), Kazakhstan[2]. The primary purpose is communication with a payload able to generate a global beam and a maximum of seven spot-beams to be directed as required to make extra communications capacity available in

---

[2]Source: National Space Science Data Center (NSSDC) at the National Aeronautic and Space Administration (NASA) Goddard Space Flight Center Greenbelt, Maryland 20771, USA; http://nssdc.gsfc.nasa.gov

areas where demand from users is high. The additional navigation payload is
included to support the EGNOS functionality using an L1 transponder.

ESA Artemis(21.5ᵒE): The artemis satellite was launched on Thursday 12 July
2001 from Kourou by an Ariane 5 carrier rocket. Due to a malfunction on the
launcher's upper stage the spacecraft was placed in a wrong orbit ($\sim$17000km).
However on 31th January 2003 a recovery mission successfully put the satellite
in its nominal geostationary orbit[3].

The primary purpose of this mission enhanced voice and data communications
between mobile terminals mainly for cars, trucks, trains and boats. Furthermore
an additional navigation payload is included, broadcasting accurate navigation
information as an element of EGNOS. The spacecraft is capable of sending and
receiving high data rate communications directly between satellites.

2.2.2 Ground segment

The EGNOS ground segment is similar to that of GPS (cf. Section 2.1.1). The
current EGNOS architecture baseline for the ground segment consists of 34 *Ranging
and Integrity Monitoring Stations (RIMS)*, 4 *Mission Control Centre (MCC)* and 7
Navigation Land Earth Stations (NLES).

The following facilities have been assigned to support the system operation.

Ranging and Integrity Monitoring Stations (RIMS):
The RIMS perform code and phase measurements from the monitored GPS and
EGNOS spacecraft. Furthermore, one of them is responsible for monitoring the
time offset between UTC and *EGNOS Network Time (ENT)*. Upon the results
the integration/steering of all RIMS Cesium and Rubidium time standards to-
wards GPS time is performed. Same RIMS channels (so called channel B) are
used to collect independent raw data for independent check of the message com-

---

[3]Source: European Space Agency (ESA) - Artemis programme; http://telecom.esa.int/artemis/

puted with channel A. The third network of RIMS (channel C) the so called *Evil Waveform Failure Modes.*

Mission Control Centre (MCC):
The MCC performs the estimation of GPS/GLONASS satellite clock corrections and confidence levels and RIMS clock bias, the satellite orbit corrections and confidence levels for GPS, GLONASS and GEO satellites. Furthermore, the MCC computes the ionospheric model for the European Civil Aviation Conference (ECAC). The entire EGNOS ground segment, EGNOS mission performance and Air Traffic Control interface are monitored.

Navigation Land Earth Stations (NLES):
The NLES generate the GPS-like signal to be transmitted to the GEO-transponder (cf. Section 2.2.3.2). The up-link signal is to be synchronised with ENT. Finally an integrity check for transmitted L1-code/carrier signal is performed.

Since February 2000 the EGNOS System Test Bed (ESTB) has been operational to support EGNOS development. Being a full scale prototype, ESTB reflects the final validation phase of EGNOS. It provides potential users with a continuous GPS augmentation service to evaluate prospective applications. Data as transmitted by the ESTB has been used in this research.

2.2.3 EGNOS - User segment and service description

The user segment will comprise receivers capable of receiving data as transmitted by the different services provided by EGNOS. To ensure interoperability with other wide area augmentation systems the *"Minimum Operational Performance Standards for GPS Wide Area Augmentation System Airborne Equipment"* [cf. RTCA-DO-299, 1996] issued by the Radio Technical Commission for Aviation (RTCA) is applied for the EGNOS message types. Furthermore the EGNOS message is compliant with the International Civil Aviation Organisation (ICAO) Oceanic Area Control Center I (OAC-I) Standards and Recommended Practices (SARPS). The three services are

described below.

2.2.3.1 Wide Area Differential (WAD) service

The EGNOS Wide Area Differential (WAD) service in general can be subdivided in the transmission of three different types of correction.

- **Fast corrections:** These are necessary to correct the fast changing errors, i.e. the satellite clock error. They are transmitted as range correction values ready to be applied directly to the range measurements. Since Selective Availability (SA) is no longer active they have lost importance. Furthermore messages contain an integrity indicator, i.e. User Differential Range Error Indicator (UDREI)(cf. Section 2.2.3.3). The fast corrections are contained in the EGNOS message types 2-7.

- **Slow corrections:** Slow corrections account for slowly varying errors such as erroneous satellite position, caused by errors in the ephemeris and the degradation of the satellite position calculations with the time. Slowly varying components of the satellite clock errors are transmitted as well. The actual corrections are provided as message type 25, containing satellite position correction $(\delta X, \delta Y, \delta Z)$, satellite *rate-of-position-change* corrections $(\dot{\delta X}, \dot{\delta Y}, \dot{\delta Z})$ and the satellite clock bias (a_{f0}).

- **Ionospheric Corrections:** The *EGNOS System Test Bed (ESTB)* ionospheric correction messages are related to an interpolation grid (message type 18) above the Earth's surface. They are transmitted as *Ionospheric Grid Points (IGP)*. The corresponding message type 26 provides an ionospheric delay value for the *Grid Ionospheric Vertical Delay (GIVD)* and the *Grid Ionospheric Vertical Error (GIVE)* an indicator which provides a bound on the accuracy of the broadcast ionospheric delay.

  Details and possible utilisation of these corrections for the research are discussed in Section 3.4.10.

2.2.3.2 GEO Ranging service

The ranging service as provided to potential EGNOS users is realised by a signal broadcast which is designed to minimise the necessary modifications on standard GPS receiver technology. The GPS frequency and the GPS-type modulation, including the C/A Pseudo Random Noise (PRN) code, are adapted to generate a GPS look-alike signal. Furthermore, the code-phase timing is maintained as close as possible to GPS time to ensure the desired ranging service.

Therefore, EGNOS satellites broadcast on a single carrier frequency of 1575.42 MHz (GPS L1). In addition to the usual GPS 1023-bit/second PRN code a 250 bit/second code is modulated to facilitate the additional navigation payload as required for the other EGNOS service components. The 1023-bit is of the same family as the GPS gold code (cf. Table 2.2). Whereas the first 37 PRN codes are reserved for GPS, the WAAS and the EGNOS PRN codes start from 120.

The fact that EGNOS satellites transmit a GPS look-alike signal is the reason behind the proposal in this research to utilise the L1 code and carrier observations for navigation and kinematic positioning.

2.2.3.3 GNSS Integrity channel

The general purpose of integrity monitoring realised in EGNOS for GPS and GLONASS is the protection of the particular system against errors which exceed a specified bound. The requirements as applicable here are very stringent in particular for applications in the field of civil aviation. The following definition of integrity in the context of SBAS is given in Roturier et al. [2001]:

"A measure of the trust which can be placed in the correctness of the information supplied by the total system. Integrity includes the ability of a system to provide timely and valid warnings to the user (alerts)."

Within EGNOS integrity monitoring, compliant with the regulations of the ICAO, has been implemented and is currently in the testing phase. The SBAS should be able to address the following integrity issues [Roturier et al., 2001; Ober, 2001].

- Failures in the GPS/GLONASS/GEO space segment (i.e. drifting or biased pseudo-ranges or so-called "Evil Waveform Failure Modes" as defined in OAC-I SARPS) should be detected and corrected/excluded by the identification of faulty satellite measurements using the network of ground reference stations.

- Transmission of faulty or erroneous differential corrections induced by either undetected failures in the ground segment or through processing of corrupted data (noise or algorithmic process).

Further the following parameters are defined in the context of system integrity.

- **Time-to-Alarm:** Is the maximal time to be allocated to warn the user that an event of integrity failure has happened.

- **Horizontal and Vertical Alarm Limit:** Specify the out-of tolerance condition in the user position domain. An event of integrity failure is given if these levels are exceeded.

The integrity information as provided by EGNOS are broadcasted as the following integrity indicators [Roturier et al., 2001]:

- The variance (σ_{UDRE}) describing the User Differential Range Error (UDRE) for each ranging source after application of fast and long-term corrections, and excluding atmospheric effects and receiver errors.

- The variance (σ_{UIRE}) describing the L1 residual User Ionospheric Range Error (UIRE) for each ranging source after application of ionospheric corrections. This variance is determined from the variance (σ_{GIVE}) of an ionospheric model based on the broadcast GIVE

The development of specific algorithms to achieve integrity monitoring for GNSS is a separate field of research. They are beyond the scope of this research.

2.3 Other recent developments

2.3.1 GALILEO

2.3.1.1 Status and planned activities

GALILEO is a joint project development of the European Union. Currently it is in its definition phase with an expected FOC around 2008. The space segment is planned as a constellation of approximately 30 Medium Earth Orbit (MEO) satellites. Different navigation related services are envisaged. According to the most recent publications [cf. Hein et al., 2002] the transmission of various service levels on three frequency bands (E1, E2, E5) is envisaged. The implications for this research are discussed briefly in Section 2.3.1.2. The following time line[4] for the definition, development, validation and deployment of GALILEO has been defined.

- ***Ongoing definition phase:*** A GALILEO Mission High Level Definition document is underway and should be published at the end of 2002.

- ***Development and validation phase (2002 - 2005):***This phase covers the detailed definition and subsequent manufacture of the various system components: satellites, ground components and receivers. A minimal space and terrestrial infrastructure should be launched to allow validation and necessary adjustment. During this phase receiver technology and local elements should be developed. Furthermore, the requirements as imposed by the *International Telecommunication Union (ITU)* to ensure the frequency allocations for the proposed frequency bands should be fulfilled.

---

[4]source: European Commission - Energy and Transport; http://www.europa.eu.int

- **_Constellation deployment phase (2006 - 2007):_** The deployment phase will involve a gradual launch of all operational satellites into orbit from 2006 onwards and the development of the required full operational ground infrastructure.

- **_Commercial deployment and application (2008 onwards):_** This includes the development of applications and receiver technology on a industrial scale. Although the main applications are expected in civil aviation, transportation, fleet management/control and in the civil services, applications in high performance surveying are also envisaged.

2.3.1.2 Implications for this research

Several technical and operational issues proposed within GALILEO will have implications on issues discussed later in the thesis. Since the scope of this research covers applications of existing systems, these points are mentioned only in brief.

- **Satellite Availability:** Including a further satellite constellation using a similar technical design would increase satellite availability dramatically. Furthermore this would have a significant impact on integrity and positioning accuracy [Ochieng et al., 2001].

- **Ionospheric Refraction:** According to the physical properties of the ionosphere (cf. Section 3.4) using frequency bands further apart would increase the efficiency and accuracy of ionospheric modelling significantly. Furthermore, linear combinations of three frequencies would have a significant impact too.

- **Ambiguity Determination:** The employment of a third carrier frequency would have a dramatic impact on ambiguity determination and its reliability. Approaches described, for example, by Vollath et al. [1999] propose a stepwise ambiguity determination based on extra-wide and wide-laning (cf. Section 3.2.2).

2.3.2 GLONASS

The Russian equivalent to GPS *GLONASS*[5] uses similar principles in terms of data transmission and positioning as GPS. The space segment of the system has been planned with 24 satellites in three orbital planes at an altitude of 19100 km. Since 1982 over 70 satellites have been placed into orbit. The constellation reached FOC mid 1996. However, due to severe financial and technical problems the constellation could not be maintained at the FOC level over the years. Figure 2.2[6] shows the development of the GLONASS constellation between the first launch (12. October 1982) and February 2002. At the time of writing the number of operational satellites has dropped down to twelve.

Unlike GPS, each GLONASS satellite transmits its own frequency to allow the
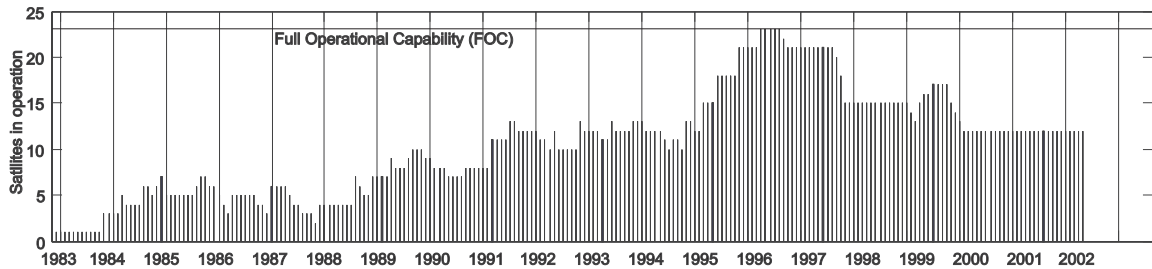
Figure 2.2: Development of GLONASS constellation between first launch (October 12th 1982) and February 2002

discrimination between different spacecraft. The technique is called *Frequency Division Multiple Access (FDMA)*. Therefore, the frequencies for the L1 band lie between 1602.5625 and 1615.5 MHz and for the L2 band between 1246.4375 and 1256.5 MHz. The individual frequency depends on the GLONASS channel (satellite) number, which takes the value 1 to 24. GLONASS satellites transmit their orbit information in a different spatial and temporal frame than GPS. For details about GLONASS and the corresponding reference frames the reader is referred to CSIC [1998a] and CSIC [1998b].

---

[5]GLObalnaya NAvigatsionnaya Sputnikovaya Sistema; russ. global navigation satellite system

[6]Source: Coordination Scientific Information Centre CSIC (Moscow), Russian Space Forces, Ministry of Defense; http://www.rssi.ru/SFCSIC/english.html

2.4 Summary

After addressing the various technical, operational and performance aspects of the various systems it was decided to proceed with the research utilising EGNOS L1 code and carrier observations to augment GPS. This is justified by the fact that although EGNOS is still under development it is the most suitable system in terms of European coverage and practical applicability exploiting the ESTB.

GLONASS could have been another option, but extrapolating the current development in the GLONASS constellation indicates that the number of available satellites will be minimal in the near future.

The fact that Galileo has not been considered any further was based on the lack of suitable software and hardware simulator engines during the major part of this research. The author's work at TRIMBLE Navigation is now assessing the possibilities of high precision and high reliability carrier phase processing using hardware simulated Galileo observations.

The next chapter will describe the functional models applicable to GPS and EGNOS observations. Error correction models will be described in detail.

Chapter 3

Functional models for GPS and EGNOS observables

This chapter looks at the models and algorithms used together with GPS and EGNOS observables to determine positional information. It addresses in particular the need to model and correct for various navigation system errors taking into account the system and operational differences between GPS and EGNOS.

A particular focus is set on the benefit of combining GPS dual frequency and EGNOS single frequency observations. The utilisation of EGNOS single frequency observation requires a particular focus on the effects of the ionosphere. Therefore, the physical and mathematical properties of the ionosphere are discussed in-depth, as well as existing models to quantify its effects.

3.1   Fundamental observations

In principle three basic observables can be identified in positioning using GPS and EGNOS; pseudo-ranges from code measurements, carrier-phases and pseudo-range differences from Doppler measurements. Because of relatively high standard deviation (several hundreds of metres) the Doppler measurement is not commonly used for high precision positioning. Examples of possible quality statistics of pseudo-range and carrier-phase measurements are given in Table 4.4.

3.1.1 The code pseudo-range observable

The measured time period needed to autocorrelate the receiver generated replica signal and the code generated by the satellite RF-module leads to the pseudo-range or code-phase measurement. Hence the time of transmission (in the satellite time frame) and the time of reception (in the receiver time frame) can be determined.

Assuming fully synchronised satellite and receiver clocks and ignoring any propagation delays, the time difference between transmission and reception would equal the signal travel time. Because satellite and receiver clocks are physically two different devices with different performance parameters, the satellite and the receiver time frame are *not* synchronised. Therefore, the measurement is called *"pseudo"*-range. A derivation of the code phase (pseudo-range) PR_i^k observation equation is given in Seeber [1993].

$$PR_i^k = \rho_i^k + c\delta_{i,clock} + c\delta_{clock}^k + I_i^k + T_i^k + \delta_{i,orbit}^k + \delta_{i,multipath}^k + \varepsilon_{i,PR}^k \qquad (3.1)$$

where

PR_i^k	is the measured range [m] i.e. as output of the receiver
ρ_i^k	is the topocentric distance between satellite k and receiver i in an Earth Centred Inertial (ECI) system [m]
δ_{clock}^k	satellite clock error [s]
$\delta_{i,clock}$	receiver clock error[s]
c	speed of light in vacuum (299,729,458.0 m/s)
I_i^k	range delay due to ionospheric refraction [m]
T_i^k	range delay due to tropospheric refraction [m]
$\delta_{i,orbit}^k$	satellite orbit error [m]
$\delta_{i,multipath}^k$	multipath error [m]
$\varepsilon_{i,\varphi}^k$	observation noise and remaining un-modelled effects [m]

In Equation 3.1 the left-hand side represents the physical measurement i.e. as output by the receiver. The right-hand side represents the decomposed parameters to be modelled as described in the following sections.

3.1.2 The carrier-phase observable

The *carrier-phase* observable denotes the part of one full wavelength in the transmitted signal. The observable is derived as the phase difference between the receiver generated reference signal (replica) in the receiver time frame and the satellite generated signal (in the satellite time frame).

The receiver "*locks on*" (i.e. starts counting the change of cycles) at the point of maximum auto-correlation and continues to measure the phase changes [cf. Townsend et al., 1995]. Since at the point of "*lock on*" the number of cycles in the receiver counter is arbitrarily chosen, the integer valued number of cycles between the receiver and the satellite is ambiguous (i.e. unknown). The key to high precision positioning is the correct determination of this integer valued number of cycles referred to as integer ambiguity.

A derivation of the carrier phase pseudo-range Φ_i^k observation equation is given in Seeber [1993].

$$\Phi_i^k = \rho_i^k + c(\frac{N_i^k}{f_{CR}}) + c\delta_{i,clock} + c\delta_{clock}^k - I_i^k + T_i^k + \delta_{i,orbit}^k + \delta_{i,multipath}^k + \varepsilon_{i,\Phi}^k \quad (3.2)$$

where (see also Formula 3.1)

Φ_i^k	is the measured carrier phase [m] i.e. as output of the receiver
N_i^k	real-valued ambiguity term; $N_i^k = \bar{N}_i^k + \phi_i - \phi^k$ [cycles]
ϕ_i, ϕ^k	initial phase at receiver, and satellite respectively [cycles]
$\bar{N}_i^k$	integer-valued ambiguity term [cycles]

$$f_{CR} \quad \text{carrier frequency:} \quad \text{L1-band} = 1575.42 = 77 \times 20.46 MHz$$
$$\text{L2-band} = 1227.60 = 66 \times 20.46 MHz$$

3.2 Modelling the observables

3.2.1 Derivation of double difference (DD) observations

The utilisation of differencing techniques is described in general in Hoffmann-Wellenhof et al. [1997]. Further extensive descriptions of differencing techniques can be found in Rothacher and Mevart [1996].

The application of these techniques significantly reduces or eliminates errors which are common either to different stations (e.g. satellite clock bias) or common to different satellites (e.g. receiver clock bias). Other errors (e.g. ionospheric range and satellite orbit bias) have a certain spatial distribution, and are significantly reduced for short baseline vectors ($< 30km$), but for longer baselines such errors decorrelate. Hence, the significance of differencing techniques for these error sources depends on the length of the baseline vector.

Among a number of possible combinations, the *single difference(SD)*, the *double difference (DD)* and the *triple difference (TD)* observables can be formed. Out of these, the DD is the one adopted for high precision applications and therefore described in more detail here. The TD observable applies differencing between consecutive epochs. It is commonly used for data screening and cycleslip detection. The other positive impact of this observable is that integer ambiguity is eliminated in addition to biases common to receivers and to satellites. However the three-step differencing strategy introduces significant noise via error propagation. For this reason, this observable is usually not used for the final baseline processing.

The following sequence of formulas is derived for combinations of carrier-phase observations but valid for code observations as well.

Two variations of the SD observable can be defined; between one satellite and two receivers i, j (across receivers) and between one receiver and two satellites k, l (across satellites). These are given by expressions 3.3 and 3.4 respectively.

$$\Delta\Phi_{i,j}^{k} = \Phi_i^k - \Phi_j^k \tag{3.3}$$

$$\nabla\Phi_i^{k,l} = \Phi_i^k - \Phi_i^l \tag{3.4}$$

Where

Δ denotes the differencing operator (across receivers)

∇ denotes the differencing operator (across satellites).

Whereas the satellite clock error is eliminated by differencing across receivers, the receiver clock error is eliminated by differencing across satellites. These two SD observables can be combined to form the DD observable (i.e. differencing across satellites and receivers).

$$\Delta\nabla\Phi_{i,j}^{k,l} = \Delta\Phi_{i,j}^k - \nabla\Phi_i^{k,l} \tag{3.5}$$

Referring to the carrier phase observation equation given by expression 3.2, the corresponding observation equation for the DD observable can be expressed as

$$\Delta\nabla\Phi_{i,j}^{k,l} = \rho_i^k - \rho_i^l - \rho_j^k + \rho_j^l + c(\frac{N_{i,j}^{k,l}}{f_{CR}}) + I_{i,j}^{k,l} + T_{i,j}^{k,l} + \delta_{multipath} + \varepsilon_\Phi \tag{3.6}$$

This leads to the observation equation which is considered in the final processing algorithm. Its positive characteristics include the cancellation of receiver and satellite clock errors. The DD observable for the pseudo range observation can be written in a similar manner. As stated earlier the influence of spatially correlated errors such as the ionospheric and tropospheric refraction as well as orbit errors are reduced to a level depending on the baseline length.

3.2.2   Linear combinations of observations on different frequencies

Whereas the previous section described linear combinations of observations between different satellites and receivers, this section describes the application of linear combinations between observations on different frequencies. Such combinations could be formulated to eliminate model parameters such as the ionospheric delay, or to transform ambiguity parameters (e.g. wide and narrow lane ambiguities).

3.2.2.1   Ionospheric free linear combination

Constructed from either the L1 and L2 carrier-phase observations or from the P1 and P2 code-phase observations, the *ionospheric free linear combination* is, as the name implies, not affected by the ionosphere. As the representation of the effect of the ionosphere is based on linear approximations using a Taylor-series expansion (cf. Section 3.4.4), this is particularly true for first order effects. Higher order effects may remain, but because they are an order of magnitude smaller they are commonly neglected. The ionospheric free linear combination usually is referred to as L_3.

For example Hoffmann-Wellenhof et al. [1997], de Jonge [1998] and Schaer [1999] show that for the linear combination for the carrier-phase observations given by

$$\Phi^k_{i,L_3} = \eta_{1,L_3} \Phi^k_{i,L_1} + \eta_{2,L_3} \Phi^k_{i,L_2} \qquad (3.7)$$

where η_{1,L_3} and η_{2,L_3} are arbitrary factors given by,

$$\begin{aligned} \eta_{1,L_3} &= +f^2_{L1}/(f^2_{L1} - f^2_{L2}) \approx +2.546 \\ \eta_{2,L_3} &= -f^2_{L2}/(f^2_{L1} - f^2_{L2}) \approx -1.546 \end{aligned} \qquad (3.8)$$

the first order effect of ionospheric refraction is eliminated. The ionospheric free linear combination of the code-phase observations can be derived in a similar manner. This linear combination is commonly used because of its ability to deal with the effects of the ionosphere. However it has a number disadvantages, including:

- The observation noise σ_{L_3} caused by error propagation is almost three times higher than for L_1 only.

$$\sigma_{L_3} = \sqrt{\eta_{1,L_3}^2 \sigma_{L_1}^2 + \eta_{2,L_3}^2 \sigma_{L_2}^2} \approx 3\sigma_{L_1} \tag{3.9}$$

- The resulting ambiguity parameter is not integer valued anymore. This has consequences for ambiguity determination algorithms (i.e. search algorithms). Hence the ionospheric free linear combination is used for determination of initial parameters. For the final baseline computation the L_1 ambiguities are solved for independently.

3.2.2.2 Wide-lane linear combination

Rewriting Equation 3.7 using the wide-lane coefficients η_{1,L_5} and η_{2,L_5} where,

$$\begin{aligned}
\eta_{1,L_5} &= +f_{L1}/(f_{L1} - f_{L2}) = +77/17 \approx +4.529 \\
\eta_{2,L_5} &= -f_{L2}/(f_{L1} - f_{L2}) = -60/17 \approx -3.529
\end{aligned} \tag{3.10}$$

leads to

$$\Phi_{i,L_5}^k = \eta_{1,L_5}\Phi_{i,L_1}^k + \eta_{2,L_5}\Phi_{i,L_2}^k \tag{3.11}$$

Equation 3.11 is the so-called *wide-lane* linear combination. Combining the double-difference observation equations for L1 and L2 (Equation 3.6) in this manner leads to.

$$\nabla\triangle L_5 = \nabla\triangle\rho + \lambda_{L_5}\nabla\triangle N_{L_5} - \xi_5\nabla\triangle I + \nabla\triangle T \tag{3.12}$$

Where

$$\begin{aligned}
\xi_5 & \quad = -f_1/f_2 \approx 1.283 \text{ is the wide-lane ionospheric conversion factor} \\
\lambda_{L_5} & \quad = c/(f_1 - f_2) \approx 862mm \text{ is the wide-land wave lenth}
\end{aligned}$$

This linear combination is of much importance for ambiguity determination because:

- The wide lane ambiguities remain integer valued. Which ensures an efficient use of search techniques reliant on the integer nature of the ambiguity (cf. Section 6).

- The ionospheric error expressed in L_5 cycles is considerably smaller compared to the corresponding errors for L_1 and L_2. Hence the determination of L_5 ambiguities is less sensitive to ionospheric bias.

The disadvantage again lies in the higher level of measurement noise as a result of error propagation, due to the combination of observables.

3.2.2.3   Melbourne-Wübbena linear combination

Another important linear combination is the so-called *"Melbourne-Wübbena"* linear combination introduced independently by Melbourne [1985] and Wübbena [1985]. It yields the linear combination between the dual-frequency code and carrier observations. This linear combination is commonly referred to as L_6 and can be written using the coefficients in Equation 3.10 in the following manner.

$$\Phi^k_{i,L_6} = \eta_{1,L_5}\Phi^k_{i,L_1} + \eta_{2,L_5}\Phi^k_{i,L_2} + \eta_{3,L_5}PR^k_{i,L_1} + \eta_{4,L_5}PR^k_{i,L_2} \qquad (3.13)$$

The coefficients η_{3,L_5} and η_{4,L_5} are determined as follows.

$$\begin{aligned}
\eta_{3,L_5} &= -f_{L1}/(f_{L1} + f_{L2}) = -77/137 \approx -0.562 \\
\eta_{4,L_5} &= -f_{L2}/(f_{L1} + f_{L2}) = -60/137 \approx -0.438
\end{aligned} \qquad (3.14)$$

It can be seen that the L_6 linear combination removes the effects of the clock offsets and the ionosphere as well as the ambiguities. High quality code observations are required for the reliable determination of the ambiguities.

3.2.3 Ambiguity determination

High accuracy satellite positioning relies on the use of the more precise carrier phase measurements. This requires accurate and reliable determination of the integer ambiguities (i.e. DD-ambiguities in the case of double difference observations). Ambiguity determination is a complex field of research. A high level description of the general concept is given here. The literature refers (see below) to two distinct strategies.

- **Static mode** denotes the observation technique where receivers occupy one position for longer time-spans of between 20 minutes (*"fast static"*) and several hours (i.e. for measurements and networks in geodynamics and geodetic referencing). For baseline lengths of less than 30 km, the process of ambiguity estimation is relatively easy and the double differenced ambiguities obtained by a *"simple"* least squares estimation should be real valued but very close to the integer value. Rounding or bootstrapping should reveal the correct integer ambiguity. This is true because for the longer observation time span the error components in the observation equation can be separated from the model parameters (i.e. ambiguities and vector components) to be estimated.

- **Real-time**, kinematic or *"on the fly"* refers to techniques where the receiver is *"on the move"* i.e. the receiver movement between epochs is expected to be larger than the expected standard deviation in the position. In such applications observations are gathered continuously. The ambiguities are either determined and used until a cycle-slip (cf. Section 3.7) occurs and then the strategy tries to resolve the integer ambiguities again or the ambiguities are determined on an epoch-by-epoch basis (*"single-epoch"* algorithms). In difficult environments with a high level of measurement errors and the regular occurrence of cycle-slips, and for baselines longer than 30 km it is difficult to determine reliable ambiguities. Such conditions require more sophisticated algorithms.

Over the last ten years, a range of different algorithms have been proposed for both, the static and the kinematic cases. Algorithms for both fields of application are

documented for example in the following publications: Counselman and Gourevitch [1981]; Remondi [1984]; Dong and Bock [1989]; Goad [1990]; Euler and Goad [1991]; Mader [1992]; Blewitt and Lichten [1992]; Euler and Landau [1992]; de Jonge and Tiberius [1994]; Mevart [1995]; Rothacher and Mevart [1996].

More recent publications [eg. Corbett and Cross, 1995; Han, 1997; Al-Hafi, 1998; Grejner-Brzezinska et al., 1998; Iz et al., 1998; Teunissen, 1998; Bonillo-Martínez et al., 1999; Kim and Langley, 1999] generally discuss refinements and application aspects of these methods.

In general, this wide range of existing models for processing GPS observations differs in complexity and diversity. A very high level definition of the linearised functional model between the unknowns and the observables can be given as follows:

$$y = Ab + \varepsilon \quad b \in R^n \tag{3.15}$$

Where y denotes the observations in data space containing the (i.e. "*observed - computed*") single or dual frequency DD carrier-phases. The vector b denotes the set of unknowns in the parameter space, A the corresponding design matrix (i.e. the functional relationships between the model parameters and the observations) and ε the system noise.

According to the nature of DD observations, some approaches such as de Jonge and Tiberius [1994]) distinguish at this point between the integer valued (i.e. DD-ambiguities) and the real valued components (i.e. baseline components) of the unknown parameter vector. Therefore, a real valued and an integer valued parameter space is defined as.

$$y = Aa + Bb + \varepsilon \quad a \in Z^n, \quad b \in R^3 \tag{3.16}$$

Where

A	is the design matrix for the integer valued parameters
a	is the vector of the integer valued parameters (e.g. ambiguities)
B	is the design matrix for the real valued parameters
b	is the vector of the real valued parameters (e.g. baseline vector)

Applying the least square principle, all different models can be solved as the following minimisation problem, given by.

$$\min_{a,b} (y - Aa - Bb) \, Q_y^{-1} \, (y - Aa - Bb) \quad a \in Z^n, \quad b \in R^3 \tag{3.17}$$

Where

Q_y	is the variance-covariance matrix of the observations

The different approaches in general, rely on the following basic four steps [cf. Al-Hafi, 1998] are illustrated in Figure 3.1:

- **Initial position:** Computation of initial position and definition of either a mathematical or a physical search space or volume that contains the correct position.

- **Test positions:** Computation of a number of test positions based on search space or volume centred by its initial position.

- **Search algorithm:** Working out a search strategy to evaluate the most likely ambiguity combination. The search is realised either in the ambiguity space or in the position space.

- **Validation algorithm:** Statistical testing of ambiguity combinations.

Linear combination of
DD code and carrier-phase
observations

Initial position

Test positions

Search algorithm

Validation algorithm

Validated DD ambiguity
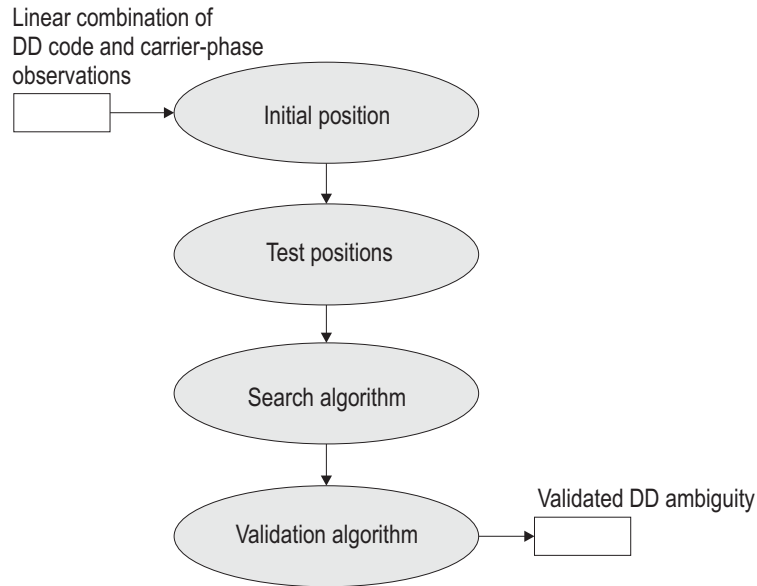
Figure 3.1: High-level processing scheme for ambiguity determination algorithms

3.2.3.1   Approaches for ambiguity determination

A selection of important approaches is discussed in more detail below. A comparative assessment of different approaches for ambiguity determination carried out during this research is given in Section 3.2.4. This assessment involves the implementation of a number of approaches for code and carrier phase processing. The analysis takes into account the differences between GPS and EGNOS architectures.

Sequential least squares filtering (SLSF):   The idea of using different sequential least squares (LSQ) filtering techniques such as *Kalman* and *Bayesian* filters to process GPS observations was first proposed by Brown and Hwang [1983]. It is based on a sequential LSQ adjustment using the statistical properties of the previous *"filter-run"* in the following one. Other authors [eg. Goad, 1990; Euler and Goad, 1991; Goad, 1992; Gross et al., 1998; Mohamed and Schwarz, 1999] subsequently revised the idea and discussed various aspects for GPS carrier-phase processing. The theory of filtering in optimal estimation can be found in Gelb [1974] and in Brown and Hwang [1997]. A brief description of Kalman filter theory is given in Section 5.2.1. Implementations

of LSQ filters may be found in static processing as well as in kinematic applications to determine preliminary baseline components.

Ambiguity Function Method (AFM): This method originates in radio interferometry and is based on the *Ambiguity Function Concept*. The concept was first considered in radar technology by Woodward [1964]. Subsequently Counselman and Gourevitch [1981] used it for processing GPS observations. Further investigations have been carried out by Remondi [1984], Mader [1992], Corbett and Cross [1995] and Al-Hafi [1998]. The algorithm operates in the position space. It attempts to infer the carrier-phase observations for each individual test position. The test position with the highest level of inference (highest ambiguity function value) is considered to be the most likely one. Since the cosine value of the carrier phase observable is used within the Ambiguity function, the unknown ambiguity term has no influence. Hence the method is completely resistant to cycle slips. The method may be applied for the static as well for the kinematic case.

Least Squares AMbiguity Decorrelation Adjustment (LAMBDA): The method was proposed by Teunissen [1993] and successfully gained importance at theoretical and practical levels. Diverse publications have since revised the method and discussed various aspects [cf. de Jonge and Tiberius, 1994; de Jonge, 1994; Teunissen and Tiberius, 1994; Teunissen et al., 1995; Tiberius and de Jonge, 1995; Teunissen, 1997; Teunissen et al., 1997b,a; Joosten et al., 1999]. Hoffmann-Wellenhof et al. [1997] and, Strang and Borre [1998] reflect different views on this method and give valuable descriptions.

The main innovations of this approach are the discrimination between real valued baseline parameters and integer valued ambiguities in the parameter space and the so-called *"Z-transformation"*. The transformation reshapes the extremely elongated search space into a search space with almost the shape of a sphere. The result is a numerical highly efficient and reliable search algorithm. It is implemented in many processing packages for the kinematic and the static case.

Fast Ambiguity Resolution Approach (FARA): This method was proposed by Frei and Beutler [1990]. Subsequently, it has been refined by Frei [1991] and Frei and Schubernigg [1992]. Mevart [1995] discusses the method in the context of other ambiguity determination approaches. Like the LAMBDA approach, it is based on statistical properties given through an initial adjustment. The method is implemented in the Bernese GPS software processing engine [cf. Rothacher and Mevart, 1996] as well in the Leica SKI Pro software which has been used in this research to validate the final results (cf. Section 6.1). The method is applied for the static and the kinematic case.

A comparative assessment is given in Section 3.2.4, to evaluate the properties and the relevance of the methods as described above with respect to ambiguity determination when observations from GPS and EGNOS are combined.

3.2.4   Integrated ambiguity determination - comparative assessment

The algorithms as introduced in Section 3.2.3 except the FARA method were implemented in code and adapted to accommodate differences imposed by the utilisation of EGNOS carrier-phase observations. The FARA algorithm is included in the comparison because it is the approach used in the LEICA processing engine.

Based on the main algorithmic steps and preliminary processing, a comparative assessment has been carried out to evaluate these algorithms. This high level assessment is based on the process defined by Al-Hafi [1998]. The assessment considers practical experiences relevant for the application of EGNOS carrier-phase observations. Table 3.1 assembles the knowledge as acquired in preliminary processing and analysis.

The methods have been evaluated using the following criteria:

- **Required observation conditions:** This considers the types of observation needed by the algorithm to perform reliably.

- **Minimum required observation time span:** The time and/or the number of epochs needed to determine reliable ambiguities.

49

- **Initial vector solution:** Type of solution required to define the location of an initial search space.

- **Search space determination:** The algorithm required to determine the size of the search space and the way its size is adapted during the computation.

- **Required cycle slip detection:** The need for reliable detection and repair of cycle sips during the preprocessing.

- **Optimisation criterion:** The mathematical criterion to find the most likely solution.

- **Size of residuals:** The magnitude of residuals as experienced during the preliminary data processing.

The purpose of this preliminary assessment was an exhaustive study of possible approaches for the algorithms to determine the unknown ambiguities. The numerical results leading to the results shown in the following table, can be found in Sauer [2000].

Table 3.1: Comparative assessment of different ambiguity determination approaches

Comparison criterion	**SLSF**	**LAMBDA**	**AFM**	**FARA**
Required observation conditions:	L1/L2 Code and carrier observations (optimal case)	single/dual L1/L2 carrier-phase observations	single/dual L1/L2 carrier-phase observations	single/dual L1/L2 carrier-phase observations
Minimum observation period	approx. 20 epochs for initialisation of filter then instantaneous solution possible	Minimum of two epochs required	single epoch solution possible with good preliminary vector estimates	for fast static ($< 20min$) applications developed, but possible with few periods
Initial vector solution	Code	Carrier-float	Code	Carrier-float
Search space determination	Statistical properties of previous estimation given by $P_{k-1|k-1}$	Hyper-ellipsoid given by transformed variance covariance matrix Q_{zz} stepwise down scaling using significance levels	Initial search cube Stepwise down scaling of grid size (Δ_{xyz}) $\Rightarrow$ size of search space $\Downarrow$	Initial search space given by Q_{xx}, then stepwise down-scaling using confidence levels
Cycle slip detection	required	required	not sensitive	required
Optimisation Criterion.	$minP^2_{k|k}$	$minQ^2_{\hat{x}\hat{x}}$	$maxAFV$	$minQ^2_{\hat{x}\hat{x}}$
Residuals from first experimental series	small residuals because ionosphere is largely removed	small residuals (dual frequency linear combination)	small residuals (dual-frequency linear combination)	small residuals (dual-frequency linear combination)

3.3   Computation of satellite coordinates

Satellite coordinates appear as functional parameters within the linearised observation equation. The coordinates which are time dependent, have to be computed with sufficient accuracy as they are usually held fixed in the process to determine the receiver coordinates. This requires well-defined relationships between the spatial reference frames for the satellite and the receiver positions. This is also true for the temporal reference frames.

The following sections give a brief overview of the orbital constellations of GPS and EGNOS as well as the corresponding spatial and temporal reference frames. An in-depth discussion of the derivation of satellite coordinates from the parameters as broadcasted within the EGNOS navigation message, is included also.

3.3.1   Temporal reference frames

GPS time is given by its *Composite Clock (CC)*. The CC or *"paper"* clock is formed statistically from two sources.

- **Time Standards on board GPS spacecrafts:** Each Block II/IIA satellite carries two cesium (Cs) and two rubidium (Rb) atomic clocks with a fundamental clock frequency of 10.23 MHz.

- **Time Standards in all monitor stations:** Temperature controlled cesium time standards.

GPS system time, in turn, is referenced to the Master Clock (MC) at the USNO and steered to UTC(USNO), i.e. the system time does deviate by more than one microsecond (except for leap seconds) from UTC. The GPS Master Control Station (MCS) continuously runs a Kalman filter to estimate the satellite clock behaviour represented as a second order polynomial. The corresponding coefficients are transmitted via the navigation message to the user segment. They are usually referred to as bias, a_0 [s], drift, a_1 [s/s] and drift-rate or aging, a_2 [s/s^2] [cf. DoD, 2001a].

In a similar manner to GPS, the EGNOS Network Time (ENT) is derived as composite clock from the EGNOS control segment's RIMS clocks. In addition, EGNOS will estimate the difference between UTC(BIPM) (as maintained by Bureau International des Poids et Mesures (BIPM)) and UTC(USNO). This will enable the estimation of ENT-UTC (as absolute values) which is also planned to be broadcast in the EGNOS-Message type 12[1].

The EGNOS satellite clock behaviour is estimated in a similar manner to GPS. The polynomial coefficients are transmitted as part of the EGNOS message type 9 (cf. Section 3.3.4.2)

3.3.2 Spatial reference frames

For navigation on Earth, it is necessary to adopt a Conventional Terrestrial Reference System (CTRS). A CTRS is realised through a set of cartesian equatorial coordinates assigned to a network of stations to define a geodetic reference frame. Two particular geodetic reference frames are of importance:

- **World Geodetic System (WGS84):** WGS84 is realised and maintained by the National Imagery and Mapping Agency (NIMA) for GPS. The original WGS84 reference frame was established in 1987 through measurements performed using a set of TRANSIT[2] station coordinates. The current realisation is WGS84 (G1150), which was adopted in January 2002. The accuracy of each station component is estimated to be about 1 cm (1σ)[3].

- **International Terrestrial Reference Frame (ITRF):** The ITRF was spec-

---

[1]Information based on personal communication with Claudio Rinaldi ESA-ESTB helpdesk

[2]Navy Navigation Satellite System, also known as TRANSIT, was the world's first operational satellite navigation system. Transit was conceived in the early 1960s to support the precise navigation requirements of the United States Navy's fleet ballistic missile submarines. Since 1962, when the first navigation sets were installed in ballistic missile submarines and aircraft carriers, the system has been used for many other navigation related applications and is now decommissioned.

[3]source: http://www.nima.mil/GandG/

ified by the International Union of Geodesy and Geophysics (IUGG) at its 20th
General Assembly in Vienna in 1991. Particular realisations of the ITRF are
indicated by a numerical suffix indicating the year. The ITRF94 is the reference
frame constructed in 1995 using all data available through 1994. The ITRF2000
is the most recent and is widely used. The accuracy of each station component
is estimated to be about 0.2 cm (1σ)[4].

The agreement between WGS 84 (GI150) and ITRF2000 is within 1 cm and the
difference is regarded as statistically insignificant [cf. Merrigan et al., 2002].

3.3.3   Orbit constellation for GPS satellites

GPS satellites are placed in a near-circular *medium Earth orbit.* The satellites are
evenly distributed in six orbital planes with orbital inclination to the celestial equator
of 55 degrees. The orbital altitude is about 20200km corresponding to an orbital
radius (semi-major axis) of 26000km . This ensures an orbit repeatability of almost
12 hours.

Details about the orbit determination and representation are extensively described
in Montenbruck and Gill [2000]. Algorithms to compute the positions of GPS satellites
are well known and documented. Explanations can be found for example in Leick
[1995], Hoffmann-Wellenhof et al. [1997] and Seeber [1993].

In order to compute the satellite positions, two different sources can be used
depending on the required accuracy.

- **Broadcast ephemeris:** This is a set of *Keplerian elements*[5] as transmitted in
  the GPS navigation message (Subframes 1-5). Details of the data structure and
  the corresponding algorithm can be found in DoD [1995]. The quality of satellite

---

[4]source: http://lareg.ensg.ign.fr/ITRF/

[5]Keplerian elements, named after Johannes Kepler (1571-1630). Parameters describing motion
of a celestial body (satellite) around it's central body (Earth).

coordinates as derived from broadcast orbits is of the order 1-2 m, depending on the number of uploads per day in the MCS [cf. Hoffmann-Wellenhof et al., 1997; DoD, 2001b].

- **Precise orbits:** This is a set of time tagged post processed satellite positions, usually published by the International GPS Service for Geodynamics (IGS), using *"SP3"*[cf. Spofford and Remondi, 1993] formatted files to represent satellite coordinates at an interval of 15 minutes. The satellite coordinates at a given epoch can be determined (in the millimetre range) using a 15th-order *"Lagrange"*[6] interpolator [Hoffmann-Wellenhof et al., 1997].

The impact of the quality of computed satellite coordinates to the final baseline standard deviations and corresponding residuals is a function of the baseline length.

3.3.4   Geostationary Earth Orbit constellation

3.3.4.1   General remarks on the geostationary orbit

Geostationary satellites keep an essentially fixed position relative to the Earth's surface. This is because the spacecraft is introduced into an almost circular orbit above the equator at an altitude of $\sim 42164.0 km$. Applying *"Kepler's law"* the satellite matches the Earth rotation rate of $\sim 1/23^h 56^m$.

Because of irregularities in Earth's gravity field, lunisolar gravity and solar radiation pressure, the satellites are actively controlled (using the on-board propulsion system) by the satellite operator within a window of $100 - 150 km$ diametre [cf. Montenbruck and Gill, 2000]. As result, the satellite oscillates around the geostationary point $+x_0, +y_0, +z_0$ (cf. Figure 3.2). λ_0 in Figure 3.2 denotes the geostationary longitude (i.e. $65.5^o E$, $15.5^o W$, $15.0^o E$ for EGNOS satellites) from the Greenwich meridian Θ.

---

[6]The algorithm is named after Joseph-Louis Lagrange (1736-1813).
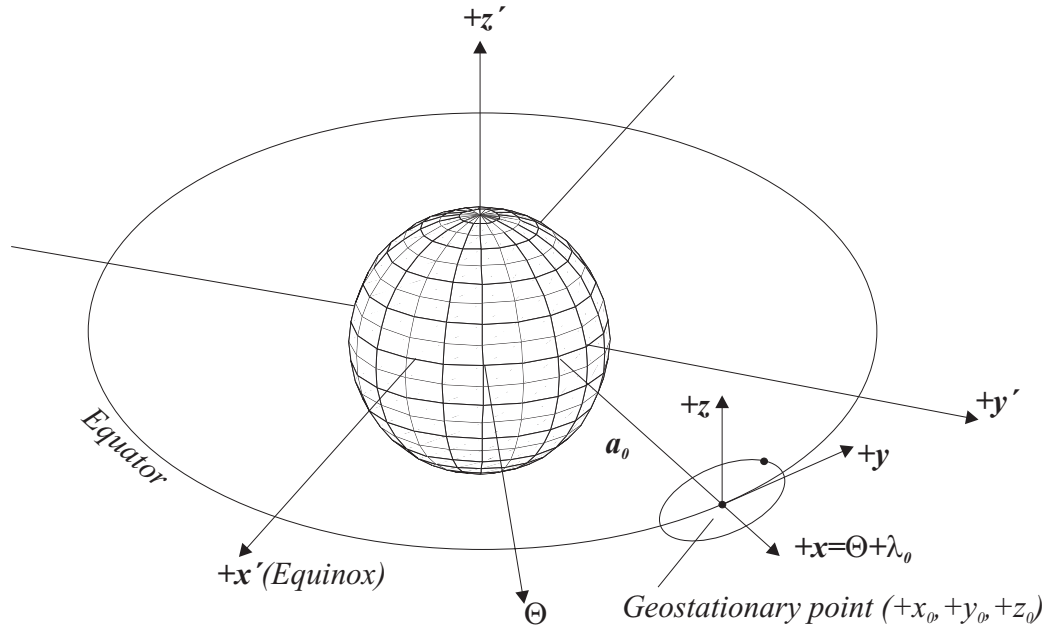
Figure 3.2: Theoretical satellite motion in the vicinity of the geostationary point

Figure 3.3 shows computed satellite positions for the time span between the 21th of March 2001 and the 29th of March 2001 for PRN 120. It can be seen that the satellite oscillates within a window of $\sim 63km \times 120km$.

The quality of orbit determination is a function of the number of participating tracking stations and the quality of corresponding tracking observations. For the GEO satellites currently operating within the ESTB, the satellite ephemeris and clock corrections produced by the MCC should result in a satellite residual error (clock and orbit) for the worst user location of less than 1.00 m (Root Mean Square (RMS))[7]. This figure applies outside periods of satellite manoeuvres.

3.3.4.2   Computation of satellite position and clock offsets for EGNOS satellites

The satellite position for the geostationary satellites are broadcast as time tagged positions (X, Y, Z), velocities $(\dot{X}, \dot{Y}, \dot{Z})$ and accelerations $(\ddot{X}, \ddot{Y}, \ddot{Z})$. Furthermore, to account for satellite clock instabilities, the *clock bias* (a_{gf0}) and the *relative frequency*

---

[7]Information based on personal communication with Claudio Rinaldi ESA-ESTB helpdesk
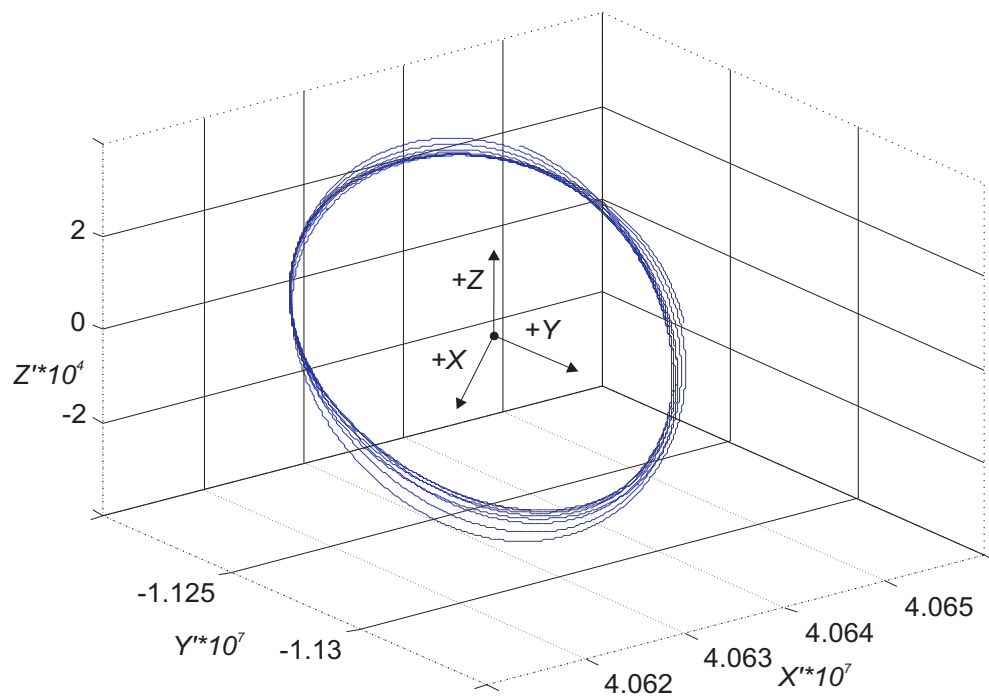
Figure 3.3: Satellite motion in the vicinity of the geostationary point for PRN 120 based on real broadcast ephemeris for the time span between 21th of March 2001 and 29th of March 2001

bias (a_{gf0}) are broadcast and decoded as well. According to RTCA-DO-299 [1996] the satellite coordinates in the satellite time frame (t) are computed as follows:

$$
\begin{bmatrix} X(t) \\ Y(t) \\ Z(t) \end{bmatrix} = \begin{bmatrix} X(t_0) \\ Y(t_0) \\ Z(t_0) \end{bmatrix} + \begin{bmatrix} \dot{X}(t_0) \\ \dot{Y}(t_0) \\ \dot{Z}(t_0) \end{bmatrix} (t - t_0) + \frac{1}{2} \begin{bmatrix} \ddot{X}(t_0) \\ \ddot{Y}(t_0) \\ \ddot{Z}(t_0) \end{bmatrix} (t - t_0)^2 \qquad (3.18)
$$

Where the time $t(t_{rec})$ in the satellite time frame is a function of the receiver time t_{rec} and the satellite clock offset and is computed as follow.

$$
t(t_{rec}) = t(t_{rec}) + a_{Gf0} + a_{Gf1}(t_{rec} - t_0) \qquad (3.19)
$$

t_0 is the time of the coordinate set broadcast.

3.3.5   Integrated GPS/EGNOS orbit data format

To enable integrated processing using the logged GPS ephemeris based on *Keplerian elements* and the GEO ephemeris based on satellite positions, velocities and accelerations, a common format was created in a preliminary processing step. The commonly used format for precise ephemeris "*SP3*" [Spofford and Remondi, 1993] was used.

The preprocessing software developed, propagates and smoothes the GPS and the GEO ephemeris to common time tags and creates an SP3 file for both systems. Figure 3.4 illustrates the high level design of the software module as implemented for the orbit computation.

The orbit smoothing is realised by a 10th-order *Lagrange* interpolation [Press et al., 1992]. Interpolation at the cm-level [Hoffmann-Wellenhof et al., 1997] is possible, with this approach.

The following Equations 3.20 to 3.21 give the algorithms used to evaluate the satellite coordinates in WGS84 $(X_{WGS84}, Y_{WGS84}, Y_{WGS84})$ at the required epoch t. The values $X_{WGS84}(t_1...t_N), Y_{WGS84}(t_1...t_N), Y_{WGS84}(t_1...t_N)$ denote the tabulated values

of the satellite positions at the time $t_1...t_N$ as given in the SP3 file and used for the interpolation.

$$X_{WGS84}(t) = \frac{(t-t_2)(t-t_3)...(t-t_N)}{(t_1-t_2)(t_1-t_3)...(t_1-t_N)} X_{WGS84}(t_1) + \frac{(t-t_1)(t-t_3)...(t-t_N)}{(t_2-t_1)(t_1-t_3)...(t_1-t_N)} X_{WGS84}(t_2)$$
$$+... + \frac{(t-t_1)(t-t_2)...(t-t_{N-1})}{(t_N-t_1)(t_N-t_2)...(t_N-t_{N-1})} X_{WGS84}(t_N) \qquad N = 10$$

$$(3.20)$$

$$Y_{WGS84}(t) = \frac{(t-t_2)(t-t_3)...(t-t_N)}{(t_1-t_2)(t_1-t_3)...(t_1-t_N)} Y_{WGS84}(t_1) + \frac{(t-t_1)(t-t_3)...(t-t_N)}{(t_2-t_1)(t_1-t_3)...(t_1-t_N)} Y_{WGS84}(t_2)$$
$$+... + \frac{(t-t_1)(t-t_2)...(t-t_{N-1})}{(t_N-t_1)(t_N-t_2)...(t_N-t_{N-1})} Y_{WGS84}(t_N) \qquad N = 10$$

$$(3.21)$$

$$Y_{WGS84}(t) = \frac{(t-t_2)(t-t_3)...(t-t_N)}{(t_1-t_2)(t_1-t_3)...(t_1-t_N)} Z_{WGS84}(t_1) + \frac{(t-t_1)(t-t_3)...(t-t_N)}{(t_2-t_1)(t_1-t_3)...(t_1-t_N)} Z_{WGS84}(t_2)$$
$$+... + \frac{(t-t_1)(t-t_2)...(t-t_{N-1})}{(t_N-t_1)(t_N-t_2)...(t_N-t_{N-1})} Z_{WGS84}(t_N) \qquad N = 10$$

$$(3.22)$$

3.3.6   The quality of orbit computation and orbit prediction and their impact

The quality of orbit determination and orbit computation has a great influence on the quality of the computed baseline coordinates. Beser and Parkinson [1982] give the following approximation for the baseline accuracy ($\sigma_{baseline}$) as a function of the baseline length (d) and the orbit accuracy (σ_{orbit}).

$$\sigma_{baseline} \approx \frac{d[m]}{20000[m]} \cdot \sigma_{orbit} \tag{3.23}$$

Figure 3.5 depicts the computed theoretical baseline quality of $\sigma_{orbit} \approx 0.005m$ from precise ephemeris, $\sigma_{orbit} \approx 2m$ from broadcast ephemeris and $\sigma_{orbit} \approx 20m$ from broadcast ephemeris (one upload/day only).

To evaluate the direct influence on the baseline quality ($\sigma_{baseline}$) the baseline
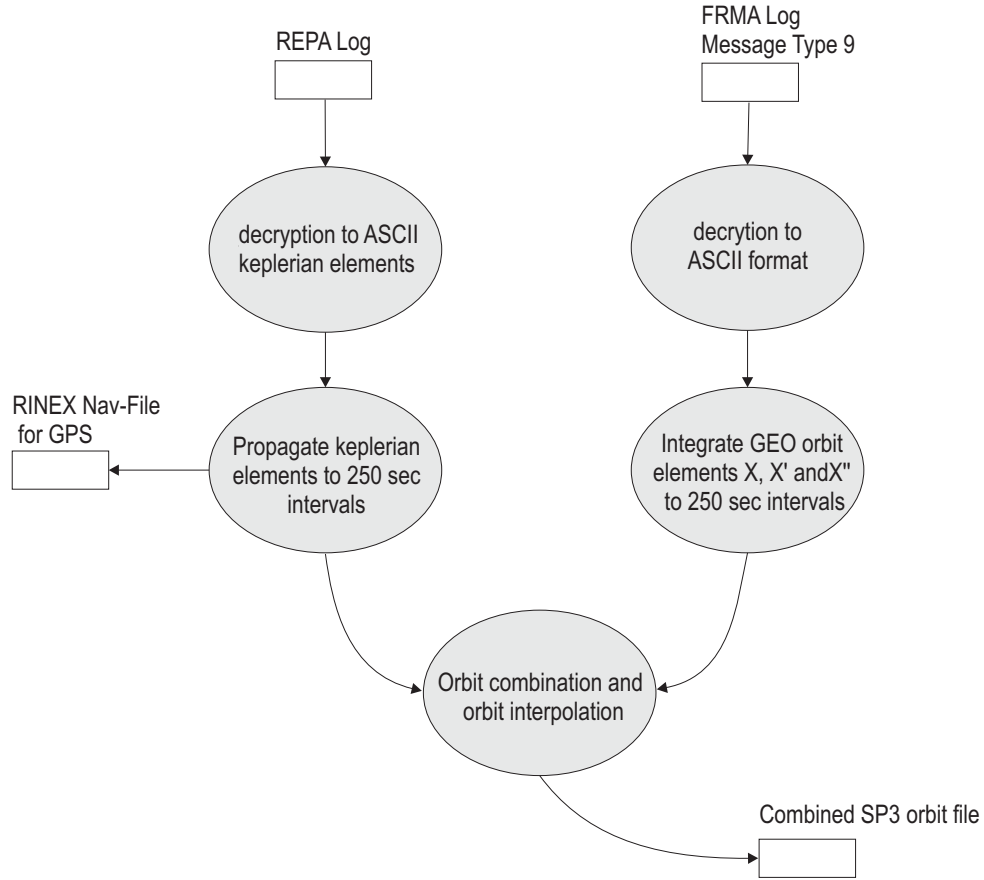
Figure 3.4: High level design of combined SP3 generation module

vector and the corresponding residuals for the baseline HUXL/HERS ($d \approx 79km$) from the test network (cf. Section 6.1) were computed using precise and broadcast orbits. Significant differences can be seen in the computed observation residuals for the L1-code (Figure 3.6) and the L1-carrier phase (Figure 3.7) as well as in the computed baseline quality (Table 3.2).

Table 3.2: Standard deviations($\sigma_X, \sigma_Y, \sigma_Z$) for the baseline vector computation (HUXL/HERS)

baseline component	using broadcast ephemeris	using precise ephemeris
σ_X [m]	0.0019	0.0015
σ_Y [m]	0.0011	0.0008
σ_Z [m]	0.0021	0.0017
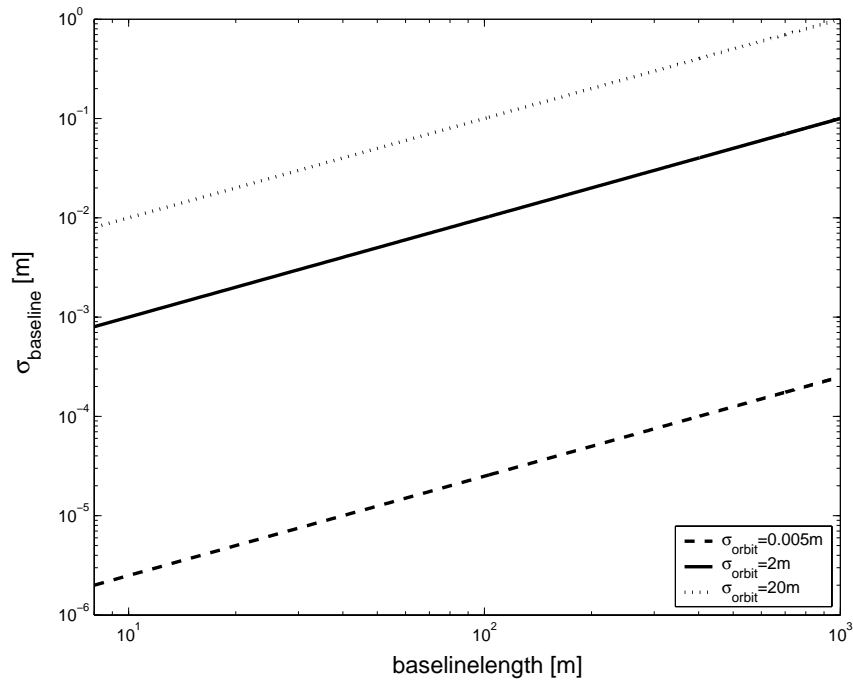
Figure 3.5: Theoretical baseline accuracy $\sigma_{baseline}$ as function of the orbital accuracy $\sigma_{orbit} = 0.005m, 2m, 20m$
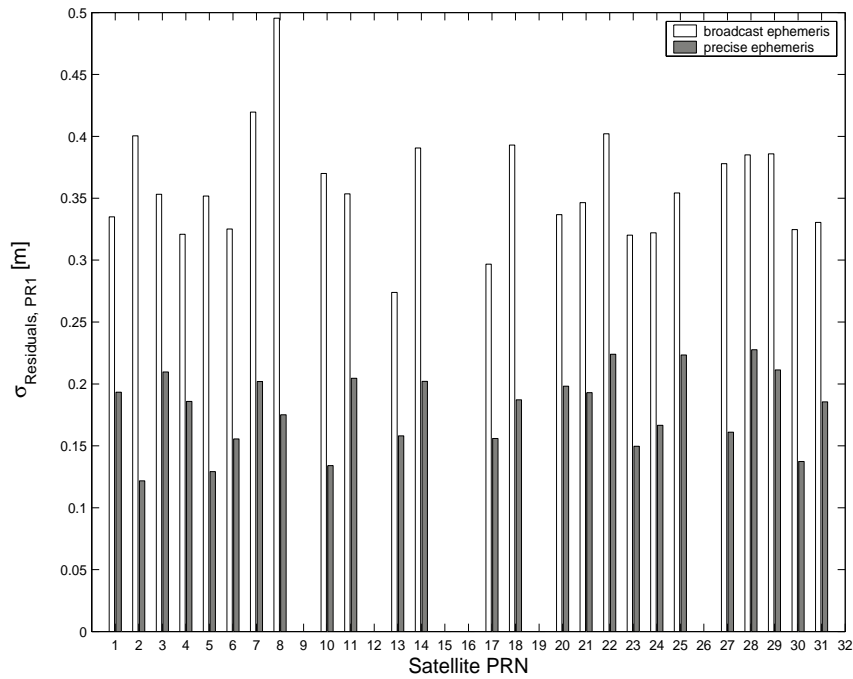
Figure 3.6: Standard deviation for pseudo-range residuals $\sigma_{Residuals,PR}[\text{m}]$ for baseline HUXL/HERS March 22nd 10.00-22.00 UTC
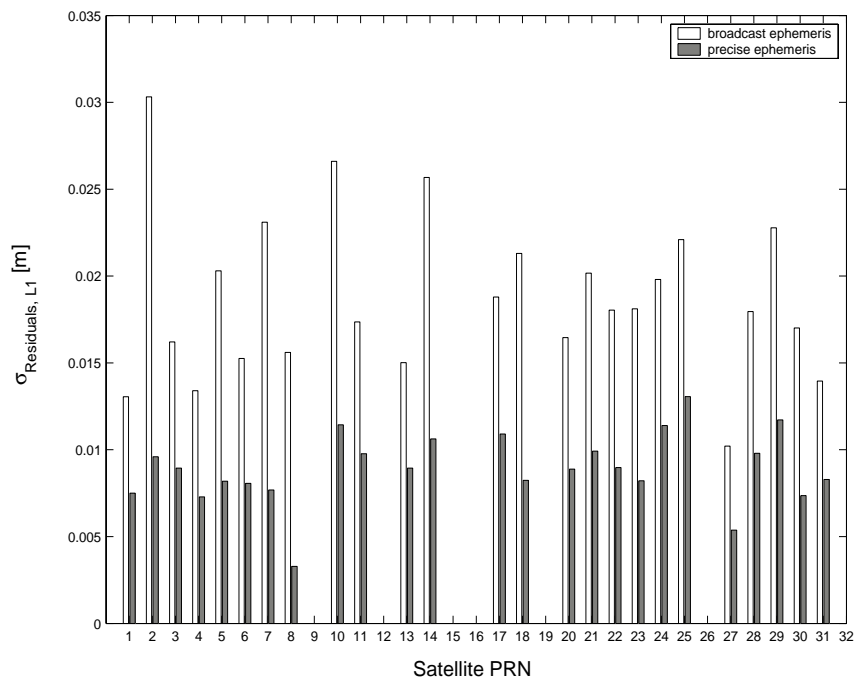
Figure 3.7: Standard deviation for carrier-phase residuals $\sigma_{Residuals,Carr}[\mathrm{m}]$ for baseline HUXL/HERS March 22nd 10.00-22.00 UTC

3.4 Ionospheric refraction

3.4.1 The ionosphere and radio-communication - General remarks

The ionosphere is the region of Earth's atmosphere between 50 and 1000km in altitude. The lower boundary follows the upper side of the *mesosphere*. The upper boundary is not well defined as it thins out into the *plasmasphere* and subsequently into the interplanetary plasma [Langley, 1998].

Radio waves travelling through the atmosphere are affected by the existence of charged particles especially in the upper part of the ionosphere. The level of impact depends on the frequency. As a *"rule-of-thumb"* it could be said, that the higher the frequency the less the impact of the ionosphere on the propagation of radio-waves. If the frequency is below a certain threshold (*"critical"* or plasma frequency) the signal would not be able to penetrate the ionosphere at all. Within the ionosphere itself the level of impact is a function of the maximum electron density.

Radio communication on Earth uses frequencies below 30 MHz because they are reflected by the ionosphere. Hence information can be transmitted around the globe. This effect was discovered by Marconi[8] in 1902. Later research by Heaviside[9] and by Kennelly[10] suggested the existence of reflective-refractive properties within the ionosphere (*"Heaviside-layer"*).

As the influence on the ionosphere decreases with a rising frequency, space based navigation systems require the use of frequencies exceeding 100 MHz. However, technical feasibility limits an infinite rise in frequency. Furthermore the signal power attenuation of higher frequencies within the troposphere could become significant [Seeber, 1993].

---

[8]Guglielmo Marconi (1874-1937), Italian electrical engineer who proved that radio waves can be transmitted around the globe without the need of *line-of-sight* between transmitter and receiver

[9]Oliver Heaviside (1850-1925), English electrical engineer

[10]Arthur Kennelly (1861-1939), Irish-American electrical engineer

3.4.2 Ionisation process

At ionospheric altitudes the atmospheric density has decreased significantly and the radiation energy (extreme ultraviolet (EUV) and X-ray) mainly emitted by the sun reaches a level where it induces a process called *photo-ionisation.* The process separates atoms and molecules causing a high concentration of free electrons. These affect the propagation of electromagnetic waves at frequencies located in the L1 and the L2 band. As the altitude increases further, the probability of photo-ionisation decreases again because the density of gaseous particles (i.e. atoms and molecules) is no longer sufficient. Further details about the physical and chemical processes within the ionosphere are given in Davies [1990].

In Davies [1990] the ionosphere is subdivided into the D, E, F1 and F2 layers. The ionospheric activity reaches a maximum in the F2 layer. In the D, E and F1 layers a high level of recombination, counteracts the ionisation process. As a first order approximation the so called *"Chapman profile"* describes the density of ion pairs as a function of the altitude along the ray path. This is commonly referred to as *Total Electron Content (TEC).* The corresponding function in Equation 3.24 describes the simple case of a parallel, monochromatic beam of solar radiation ionising a homogenous gas in a 2-dimensional shell [cf. Davies, 1990; Schaer, 1999].

$$TEC = N_0 e^{(1-z-\chi e^{-z})} \qquad with \qquad z = \frac{h - h_0}{\Delta h} \qquad (3.24)$$

where

TEC	Total electron content
N_0	is the maximum electron density of the Chapman profile referred to $\chi = 0$ deg
χ	is the solar zenith distance
e	base of the natural exponential function (2.71828182845905)
h	height above Earth surface at which the electron density

Electron density in $\log_{10}N_E(m^{-3})$
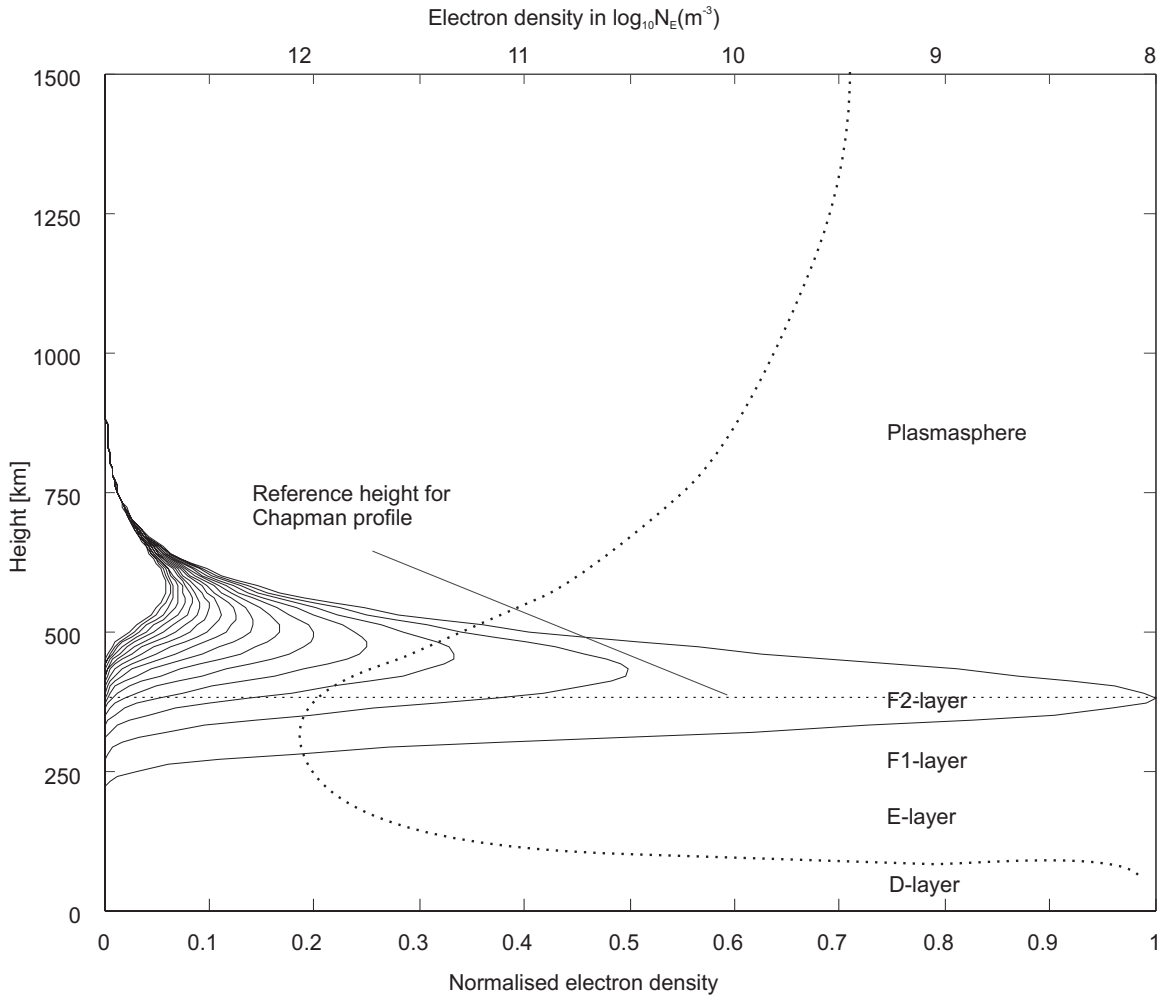
Figure 3.8: Simulated Chapman profile (normalised electron density) left curves and typical vertical profile of the ionosphere after Davies [1990]

along the profile to be evaluated

h_0 is the height of maximum electron density N_0 above Earth surface at $\chi = 0$ deg

Δh scale height

Figure 3.8 illustrates the different layers in the ionosphere versus the corresponding computed normalised density distribution function, based on Equation 3.24 (left continuous curves). The profile has been computed for h_0=350 km and for $\chi = 0^o...85^o$

in 5° increments. The dotted curve on the right depicts a typical vertical profile of the ionosphere as given in Davies [1990]. Whereas the curve on the right represents a description of the ionosphere based on physical properties, the Chapman profile represents its mathematical approximation.

According to Schaer [1999] a more general definition for the TEC can be given as the integral of the electron density N_e per m^2 along the slant ray-path between transmitter and receiver.

$$TEC = \int N_e(\rho)d\rho \qquad (3.25)$$

The spatial distribution of charged particles in the ionosphere is determined by photochemical and transportation processes. The following global and local phenomena are of significance.

Large scale phenomena: Are mainly caused by the magnetic field and its circular and lateral movement with respect to the geographic pole. This is the reason why global ionospheric models (cf. Section 3.4.8) use geomagnetic coordinates to represent the spatial distribution of the ionosphere.

Medium-and small-scale phenomena: Are mainly caused by severe disturbances in the magnetic field (magnetic storms) or intense solar eruptions (ionospheric storms). These phenomena show periods of 10 minutes to 3 hours and wavelengths between a few hundreds to 1000 km for the medium scale phenomena. Small scale phenomena show periods of several minutes and wavelengths of a few tens of km. These irregularities may result in significant growth in the local electron content.

Ionospheric scintillation: Is caused by irregularities of the ionospheric electron density along the ray path. The effects are usually rather small except in the equatorial region, where after sunset they could distort radio signals to a level of up to several dB.

Travelling Ionospheric Disturbances (TID): This phenomenon is based on so-called Atmospheric Gravity Waves (AGW) i.e. moving wavelike irregularities

in the gravity field. Mainly they start in the North and South auroral regions but may travel down to mid-latitude or even equatorial regions. These coherent frontal disturbances travel large distances through the ionosphere and are very difficult to predict. Research suggests that the fourier-transform of scatter radar observations [cf. Balthazor and Moffett, 1997] should show indications of Travelling Ionospheric Disturbances.

3.4.3 Solar activity

The ionisation process in Earth's ionosphere is mainly related to the level of solar radiation. Solar radiation, in turn, depends on solar activities such as physical and chemical processes in the sun and on the celestial constellation between the sun and the Earth (i.e. solar and Earth rotation, Earth revolution). The number of so-called *sunspots* is used to quantify solar activity based on visual observations. Sunspots appear as dark spots on the surface of the sun. Temperatures in the dark centres of sunspots drop to about 3700 K (compared to 5700 K for the surrounding photosphere). Sunspots are magnetic regions of the sun with magnetic field strengths thousands of times stronger than the Earth's magnetic field.

Sunspots have been observed by the *Solar Influences Data Analysis Center (SIDC)*[11] for almost the last 250 years. Although the way sunspots are counted is slightly arbitrary, it gives a valuable long-term indicator of solar activity. Figure 3.9 shows the periodicity in the occurrence of sunspots of 80, 22 and 11-years.

The so-called *"cycle 23"* (cf. Figure 3.10) which occured during the 2000-2001 period has been subjected to GPS related research [cf. Kunches, 2000; Hansen et al., 2000]. This period of increased solar activity caused significantly higher levels of ionospheric refraction. Results showed increased uncertainties in GPS measurements as a result of increased ionospheric refraction. Kunches [2000] has reported up to 100% drop in positioning accuracy using single frequency measurements.

---

[11]Solar Influences Data Analysis Center (SIDC) at the Royal Observatory of Belgium; http://sidc.oma.be

The high solar activity has also introduced increased uncertainties in local, regional and global ionospheric models. This is true in particular for areas of higher local ionospheric activities.

3.4.4   Wave propagation and ionosphere

Various publications [Saastamoinen, 1973; Davies, 1990; Brunner and Gu, 1991] describe the properties of radio-waves travelling through the atmosphere.

The simplest approach of describing radio wave propagation in general is to solve for the refractive index, η. based on *"Snell's Law"*. This physical principle describes the relationship between angles and velocities of incidence and refraction for a wave impinging on a dielectric. It is based on the boundary condition that a wave is continuous across the boundary. This requires that the phase of the wave is constant in any given plane.

η describes the ratio between v_1 the speed of light in the medium the ray-path comes from and v_2 the speed of light in the medium being entered.

$$\eta_{medium_2, medium_1} = \frac{v_2}{v_1} = \frac{\sin(\alpha_2)}{\sin(\alpha_1)} \tag{3.26}$$

Where
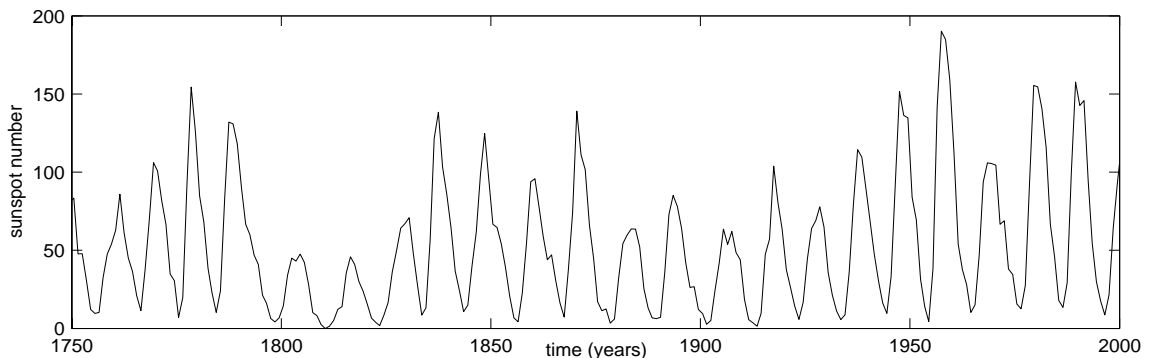
Figure 3.9: Sunspot number since 1750 as measure of solar activity (source: SIDC; 2001)
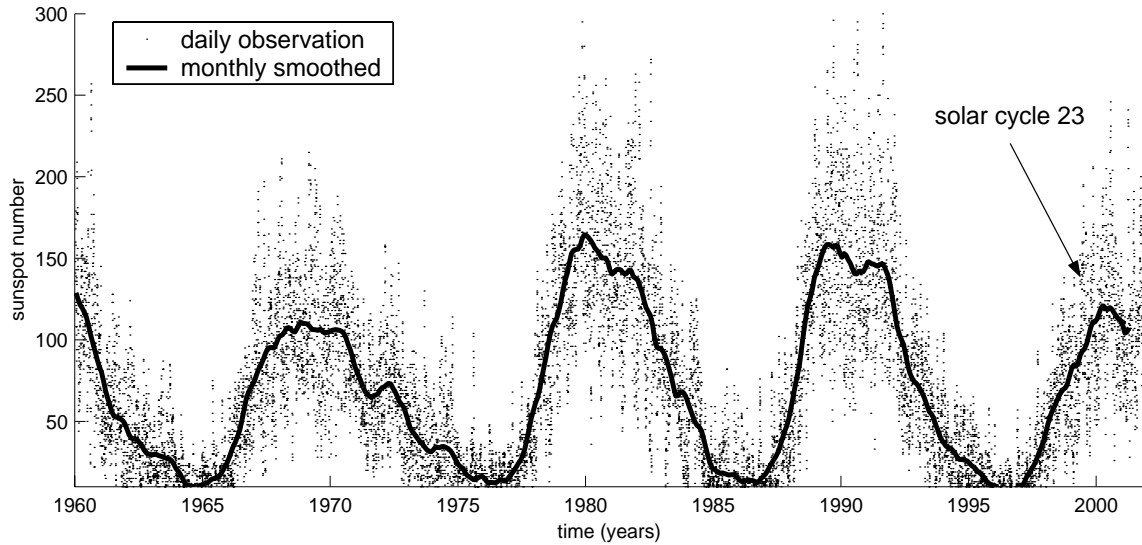
Figure 3.10: Daily observed and monthly smoothed sunspot number for the period 1960-today (source: SIDC; 2001)

α_1, α_2 represent the angles of incidence and refraction respectively.

According to *"Fermat's Principle"*[12] the measured path length, L_c, of a radio wave which propagates along the path L through the atmosphere is given by Saastamoinen [1973].

$$L_c = \int_L \eta(\rho)d\rho \qquad (3.27)$$

Where

$\eta(\rho)$ is the refractive index as function

---

[12]Pierre de Fermat(1601-1665) Although he pursued mathematics as an amateur, his work in number theory was of such exceptional quality and erudition that he is generally regarded as one of the greatest mathematicians of all time. "Fermat's Principle" states that a ray path bends according to the refractive index as a function of the position along the ray path.

of the position ρ along the path L

Since the refractive index depends on the frequency, the ionosphere is a *"dispersive"* medium, i.e. its effects on radio waves are frequency dependent. This is particularly true for frequencies used in satellite navigation systems.

According to this definition, the troposphere (cf. Section 3.5) would be dispersive too, but the effects based on dispersiveness are orders of magnitude smaller. Hence the troposphere is considered as non-dispersive in the context of satellite navigation.

A general expression for η, refractive index, in the ionosphere based on a power series expansion is given by Seeber [1993]:

$$\eta = 1 - \frac{c_x}{2f^2}N_e \pm \frac{c_x c_y}{2f^3}N_e H_0 \cos\xi - \frac{c_x^2}{8f^4}N_e^4 + ... \tag{3.28}$$

Where the constants C_x and C_y can be given as:

$$C_x = \frac{e^2}{4\pi^2\varepsilon_0 m_e} \approx 80.6 \times 10^{16} ms^{-2}TECU^{-1}$$

$$C_y = \frac{\mu_0 e}{2\pi m_e} \tag{3.29}$$

Where:

H_0	is the geomagnetic field strength
ξ	is the angle between the propagation direction of the electromagnetic wave and the electromagnetic field vector
ε_0	is the dielectric constant for the vacuum
e	is the charge of one electron
m_e	is the mass of one electron
μ_0	is the permeability of vacuum
N_e	is the electron content.

The third and fourth order terms in Equation 3.28 are usually ignored because they are several orders of magnitude smaller than the second order term.

Using the definition in Equation 3.25 and integrating along the ray-path leads to the slant ionospheric range delay for the phase measurement I_{phase}:

$$I_{phase} = -\frac{40.3}{f^2} \int N_e(\rho)d\rho[m]$$ (3.30)

Based on Equation 3.30 it can be seen that ranges based on phase measurements, i.e. in GPS, are measured *"too short"*. Whereas ranges based on code measurements depend on the group frequency and are therefore measured *"too long"*. For first order approximation ionospheric effects on code and carrier frequencies are equal in magnitude but of opposite sign.

3.4.5   The ionospheric observable based on dual frequency observations

Based on the integral given in Equation 3.30 and on carrier-phase measurements (Equation 3.2) on the two different frequencies f_1 and f_2, the resulting ionospheric delay $\Delta\Phi_{iono,L1}$ in metres for the first carrier frequency can be written as follows.

$$\Delta\Phi_{iono,L1} = \frac{f_{L1}^2}{f_{L2}^2 - f_{L1}^2}\left(\Phi_{L1} - \lambda_{L1}N_{L2} - \frac{f_{L1}}{f_{L2}}(\Phi_{L2} - \lambda_{L2}N_{L2})\right)$$ (3.31)

Where:

λ_{L1} is the wavelength of the first carrier $\approx 0.19029m$

λ_{L2} is the wavelength of the second carrier $\approx 0.24421m$

The corresponding error components as given in Equation 3.2 have been omitted. Note that these errors have to be modelled to compute the ionospheric phase delay accordingly.

In a similar manner the ionospheric delay for the code measurements can be written, as:

$$\Delta PR_{iono,L1} = \frac{f_{L1}^2}{f_{L2}^2 - f_{L1}^2} \left(PR_{L1} - \frac{f_{L1}}{f_{L2}} PR_{L2} \right) \tag{3.32}$$

3.4.6 Methods to model and parameterise the ionosphere

3.4.6.1 General remarks

In general ionospheric models are grouped into physical and mathematical models. Four types of models are described below.

- **Physical-theoretical** models are based on the physical laws describing the spatial and temporal behaviour of the ionosphere. They are of general validity but they do not represent small scale variations as required for radio navigation purposes. For this reason such models have not been considered any further for this research.

- **Physical-empirical** models are based on actual observations of the ionosphere. The observations originate, for example, from incoherent scatter radars[13], ionosondes[14] and dual-frequency GPS observations. The *physical-empirical* models described in Sections 3.4.6.2 and 3.4.6.4 are of particular practical interest.

- **Mathematical-deterministic** models are based on physical properties but represented by rather simple mathematical functionalities. They are often "tailored" to a required application. Examples of such models are described in Section 3.4.6.3, 3.4.6.6 and 3.4.6.5.

---

[13]The *"incoherent"* scatter echo is the result of the scattering of electromagnetic energy, emitted by a radar antenna, by electrons in the ionospheric plasma. Most of the power is due to scattering from electron density fluctuations caused by the presence of ions. The frequency spectrum of the received signal provides information about their temperature, composition and velocity.

[14]Iono-sondes are analytical devices that measure directly the reflected energy as a function of frequency and electron content.

- **Mathematical-stochastic** models are based on a rather large number of observations (i.e. GPS dual frequency observations). The statistical properties of the measurements are used to describe spatial and temporal ionospheric behaviour. Section 3.4.6.7 describes an advanced approach referred to as *"ionospheric tomography"*.

The models above in general try to describe the ionosphere as a function of time and location. Of particular interest in the context of radio navigation is the induced range delay along the direct *line-of-sight* or *slant* range between the satellite and the receiver. The slant delay is computed from the vertical delay above using an appropriate mapping function. Different mapping functions are described in Section 3.4.6.3.

3.4.6.2 International Reference Ionosphere (IRI)

The International Reference Ionosphere (IRI) is an international project sponsored by the *Committee on Space Research (COSPAR)* and the *International Union of Radio Science (URSI)*. These organisations formed a working group in the late sixties to produce a physical-empirical standard model of the ionosphere. The IRI attempts to represent the global ionosphere based on all available data sets [cf. Rawer et al., 1978; Bilitza, 2001].

Several versions of the model have been released in recent years (IRI90, IRI95, IRI2001) reflecting the improvement in the original data sources and the computation. For a given location, time and date, IRI describes the electron content, electron density, electron temperature, ion temperature and the ion composition in the altitude range from about 50 km to about 2000 km. It provides monthly averages in the non-auroral ionosphere for magnetically quiet conditions. The model does not describe small scale (temporal and spatial) magnetic irregularities.

The major data sources are the worldwide network of iono-sondes, incoherent scatter radars, ISIS and Alouette topside sounders, as operated be the *International Geophysical Union (IGU)*, and in situ instruments on several satellites and rockets

as operated by the *National Aeronautic and Space Administration (NASA)* and the *European Space Agency (ESA)*.

In the context of radio-navigation it provides a valuable reference and validation tool for large scale measurements.

3.4.6.3   The Single Layer model and mapping functions

As described in Section 3.4.2 most of ionospheric activity takes place in the F2 layer (300-400km).

Based on this fact, it has been proposed by several publications [cf. Klobuchar, 1987; Davies, 1990; Schaer, 1999; RTCA-DO-299, 1996] to approximate the ionosphere by an infinitesimally thin ionospheric layer. The main parameter of the single layer approach is given by the ionospheric shell height usually between 300 and 400 km altitude. The influence and the validity of the shell height highly depends on the solar and geomagnetic activity and has been studied extensively by Komjathy [1997] and Schaer [1999]. Furthermore, these publications discuss algorithms to determine the optimal shell height.

The primary interest of most satellite navigation related applications lies in the total slant ionospheric delay rather than a complete ionospheric profile, which would be way too expensive in terms of required observations and computational effort. There is only secondary interest in the vertical distribution as given by a complete 3D ionospheric model (see Section 3.4.6.7).

To relate the total vertical ionospheric delay as represented by the ionospheric model and the required slant delay between satellite and receiver, a *mapping function* is used. The general form of the mapping function can be written as follow.

$$F = \frac{TEC_{slant}}{TEC_{vertical}} \tag{3.33}$$

Figure 3.11 describes the geometric relationships between the mapping function

F, the shell height H (usually chosen between 300 and 400km), the zenith angle Z and the Earth radius.
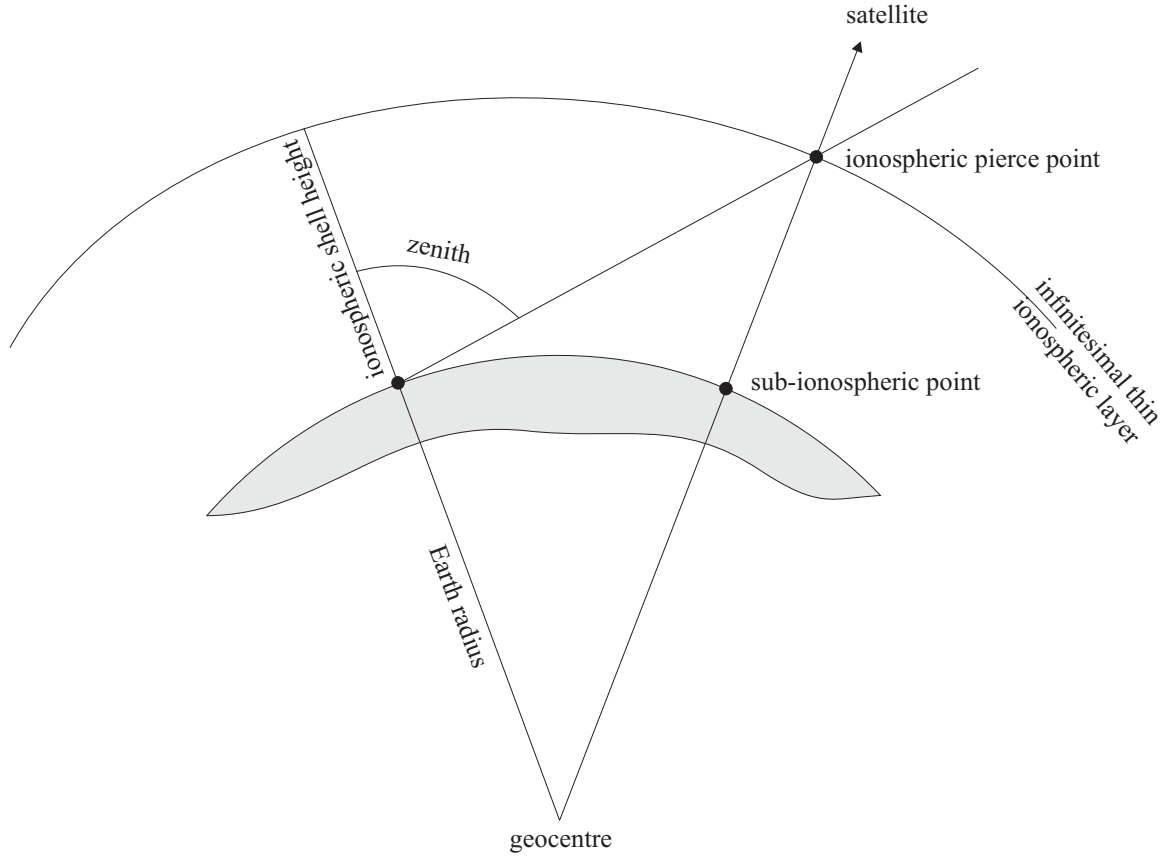
Figure 3.11: Geometry of single layer model using a infinitesimally thin shell

The publications as mentioned above propose the following different mapping functions.

Q-factor mapping function (QFMF): Based on a third order polynomial which is fitted through a uniformly structured ionospheric shell between 200 and 600 km [cf. Clynch et al., 1989]:

$$F_{QFMF}(E) = \sum_{i=3}^{3} q_i \left(\frac{E}{90}\right)^{2i} \tag{3.34}$$

Where $q_{0...3}$ take values of $1.0206, 0.4663, 3.5005, -1.8415$. E denotes the eleva-

tion in degrees.

Single Layer Mapping Function (SLMF): Based on integration along the chapman profile (Equation 3.24). An expression for the SLMF is given by Mannucci et al. [1993]. Taking the TEC definition in Equation 3.25 and setting $\delta h \rightarrow 0$ leads to:

$$F_{SLMF}(E) = \frac{1}{\cos\left(\arcsin\left[\cos(E)\frac{R_{Earth}}{R_{Earth}+h}\right]\right)} \tag{3.35}$$

Broadcast model mapping function (BMMF): Proposed by Klobuchar [1987], this is a polynomial approximation of the standard geometric mapping function. The function deviates from the exact value as given by the original mapping function by no more than 2%. It assumes an ionospheric shell height of 350 km. The standard mapping function to be used with the GPS broadcast ionospheric model is given as follows.

$$F_{BMMF}(E) = 1 + 2\left(\frac{96-E}{90}\right)^3 \tag{3.36}$$

According to Schaer [1999] there is no obvious advantage of using either the QFMF or the BMMF. The single layer mapping function has been used for the research because of both its simplicity and the rather low computational demand.

3.4.6.4   Broadcast model

Also based on physical-empirical considerations the *"Broadcast model"* approximates the ionosphere assuming a *"half daily-cosine"* like behaviour. The vertical TEC distribution in TECU $TEC_{vert}(\phi_m, \lambda_{fix})$ is a function of ϕ_m and λ_m (the geomagnetic latitude and the sun-fixed longitude respectively) and can be expressed as follows [Klobuchar, 1987; Hoffmann-Wellenhof et al., 1997].

$$TEC_{vert}(\phi_m, \lambda_{fix}) = \begin{cases} TEC_{\min} + TEC_{amp}(\phi_m)\cos\lambda'_{fix} & if\ \left|\lambda'_{fix}\right| < \frac{\pi}{2} \\ TEC_{\min} \end{cases} \tag{3.37}$$

where

$TEC_{amp}(\phi_m)$ is the TEC amplitude as a function of ϕ_m

$TEC_{\min}$ is the minimum TEC value at night time corresponding to 5ns delay on L1

λ'_{fix} $= 2\pi(\lambda_{fix} - \lambda_0)/\tau(\phi_m)$ whereas λ_0 the solar fixed latitude of the diurnal maximum is (i.e. $2h \sim \frac{\pi}{12}$)

The shape of $TEC_{amp}(\phi_m)$ is represented by a third order polynomial using eight coefficients (i.e. $\alpha_0...\alpha_3$; $\beta_0...\beta_3$). These coefficients are transmitted as part of the GPS navigation message. The Broadcast model is derived from a world wide empirical "Bent"-model with a validity of 2-10 days. The model describes the ionospheric electron density as a function of latitude, longitude, time, season, and solar flux (cf. Section 3.4.3). The topside is represented by a parabola and three exponential profile segments, and the bottom side by a bi-parabola [Bent et al., 1972].

The associated mapping function relating the vertical to the corresponding slant delay is described in Section 3.4.6.3.

Common experience shows that the broadcast model provides a correction for about 50% RMS of the ionospheric range error. To validate the differences the derived vertical corrections have been compared with the corrections derived by the post-processed "CODE model"[15]. Numerical details on the models above are given in Section 3.4.11.

3.4.6.5 Taylor series expansion

One commonly used approach to determine and represent a local TEC distribution is the application of a two dimensional Taylor series expansion of the following form.

---

[15]The CODE model refers to the global ionospheric model produced on a daily basis by the Center for Orbit determination in Europe (CODE), http://www.cx.unibe.ch/aiub/ionosphere.html

The TEC is represented by a truncated Taylor series expansion as a function of the geographic latitude ϕ, and the sun fixed longitude λ_{fix}.

$$TEC_{vert}(\phi, \lambda_{fix}) = \sum_{i=0}^{n} \sum_{k=0}^{m} E_{ik}(\phi - \phi_0)^n (\lambda_{fix} - \lambda_{fix,0})^m \tag{3.38}$$

Where,

$\phi_0, \lambda_{fix,0}$ is the origin of development (latitude, longitude)

E_{ik} are the coefficients of the Taylor series

Further details can be found in Wild [1994] and Komjathy [1997]. These publications describe how to determine and validate the Taylor coefficients during the modelling stage based, on a network of GPS dual frequency receivers.

3.4.6.6   Spherical harmonics expansion

The application of spherical harmonics expansion has been proposed by Schaer et al. [1995] and Schaer [1999] to represent the TEC distribution on a global scale.

This mathematical deterministic approach originates in physical geodesy to represent Earth gravity field. It relates a rather simple mathematical model in the model space to a number of physical measurements. Further details can be found in Vaniček and Krakiwski [1982] and Torge [1991]. The method is not suitable to represent a local ionosphere but is mentioned here for completeness.

$$TEC_{vert}(\phi, \lambda_{fix}) = \sum_{n=0}^{n_{\max}} \sum_{m=0}^{n} \tilde{P}_{nm}(\phi) \left(\tilde{C}_{nm} \cos(m\lambda_{fix}) + \tilde{S}_{nm} \sin(m\lambda_{fix}) \right) \tag{3.39}$$

Where,

n_{max} is the degree of spherical harmonics expansion

$\tilde{P}_{nm}$ is the normalised Legendre polynomial (degree n, order m)

$\tilde{C}_{nm}, \tilde{S}_{nm}$ are the unknown zonal and sectorial coefficients of the spherical harmonics function to be determined or the parameters representing the global ionosphere

3.4.6.7 3D ionospheric tomography

Based on a mathematical-stochastical approach, ionospheric tomography is an attempt to reconstruct a local TEC distribution. It is based on the decomposition of the ionosphere into 3-dimensional cells (assuming a constant electron content for each cell). The cell size is related to the sensitivity of the data and electron density. Using the linear combination L_5 (cf. Section 3.2.2) between the L_1 and L_2 carrier phase observations, a general observation equation can be written as follows [cf. Hernández-Pajares et al., 1999].

$$L_5(t+\tau) - L_5(t) = \kappa \sum_i \sum_j \sum_k (N_e)_{i,j,k} \left[\Delta s_{i,j,k}^{t+\tau} - \Delta s_{i,j,k}^t \right] \qquad (3.40)$$

Where,

$L_5(t+\tau) - L_5(t)$ is the linear combination between L_1 and L_2 at time t and at time $t+\tau$

κ $= K \left[1/f_2^2 - 1/f_2^1 \right] \approx 1.0506 m / 10^{17} electrons/m^2$

K is the proportionality factor based on Equation 3.29 and 3.30

N_e is the electron density per cell to be modelled

$\Delta s_{i,j,k}^{t+\tau} - \Delta s_{i,j,k}^t$ is the difference of the length of the ray path between both instances in time

Several publications give details about the use of 3D ionospheric tomography based on GPS dual frequency observations [cf. Hansen et al., 1997; Hernández-Pajares et al., 1999, 2000]. 3D-ionospheric tomography is able to describe spatial and temporal ionospheric behaviour to a high level of resolution but relies on a dense network of observing stations. Furthermore, it is rather demanding in terms of computational effort.

3.4.7   Applicability for sparsely distributed data sets

The practical utilisation of the models above is based on the availability of a dense network of observing stations. Although these models are rather demanding in terms of computational effort they are able to describe the ionosphere at a very high level of accuracy.

For the task of modelling local ionosphere for single-frequency EGNOS data based on dual-frequency GPS measurements taken only from a set of two receivers, a much simpler model has been proposed. It is based on the application of a bi-harmonic spline. The details of this approach are described in Chapter 5. This model attempts to use all available data including existing ionospheric models and dual frequency GPS observations. The following section gives an overview of the available ionospheric models.

3.4.8   Available data sets and models to describe the ionosphere

Several agencies and institutions publish ionospheric data and the corresponding models [cf. Feltens and Schaer, 1998; Schaer, 1999]. These mainly differ in their spatial-temporal applicability and resolution as well as in their availability (delay between actual time of model computation and time of publication). In general these models are post-processed and are available with significant time delay. Since the research

carried out is related to real-time processing, such models can be used for referencing and for initialisation only.

The *International GPS Service for Geodynamics (IGS)* coordinates the efforts of different agencies involved in the generation of ionospheric models [Feltens and Schaer, 1998]. The major models are summarised below.

Jet Propulsion Laboratory (JPL): Global Ionospheric Maps (GIM) are generated on an hourly and daily basis using data from up to 100 GPS sites operated by the IGS and others institutions. The vertical TEC is modelled in a solar-geomagnetic reference frame using bi-cubic splines on a spherical grid. A Kalman filter is used to solve for instrumental biases and VTEC on the grid (as stochastic parameters) simultaneously. The standard deviation of the ionospheric estimates is given as approximately 0.79 TECU.

Center for Orbit determination in Europe (CODE): The CODE global ionosphere maps are generated on a daily basis. The TEC is modelled with a spherical harmonic expansion up to degree 12 and order 8 with reference to a solar-geomagnetic reference frame. The 12 2-hour sets of 149 ionosphere parameters per day are derived from GPS data from the global IGS (International GPS Service) network. The density of stations within Europe is particularly high [cf. Schaer, 1999]. The standard deviation of the ionospheric estimates ranges from 0.92 to 1.45 TECU. The model is described further in Section 3.4.9.

Natural Resources Canada (NRCan): NRCan ionosphere maps are generated daily. The grid point values are the mean VTECs estimated in sun-fixed reference frame. 43 station contributing dual frequency GPS data to this model. The standard deviation of the ionospheric estimates is given as approximately 1.74 TECU.

European Space Agency (ESA): The model is from the Ionosphere Monitoring Facility (IONMON). The facility estimates a variable ionospheric profile (height) and the corresponding TEC values every 24 hours. There are 49 stations con-

tributing [cf. Feltens et al., 1999]. The standard deviation of the ionospheric estimates is given with approximately 0.92 TECU.

The CODE model has been used to validate and enhance the real-time local ionospheric model developed in this research (cf. Section 5.3). The reasons include its availability, instant accessability, the density of tracking stations and model quality.

3.4.9   The CODE ionospheric correction model

The CODE model is distributed either by a set of spherical harmonic coefficients determined by the algorithm described in Section 3.4.6.6, or by a grid based model (IONOsphere EXchange Format (IONEX) file for a period of 24 hours). IONEX has been introduced by the IGS and is described in Schaer et al. [1998]. The files contain TEC values and the corresponding standard deviations given with a temporal resolution of 2 hours with a processing related delay of approximately two days. In the spatial domain the resolution is given by the size of the grid with dimensions of $\delta_{Longitude} = 5^o$ and $\delta_{Latitude} = 2.5^o$. A sample file is given in Appendix B.2.

The adjusted standard deviation representing the quality of the mean TEC determination is given by Schaer [1999] and ranges from $0.92 - 1.45$ TECU ($0.14 - 0.23$ m, L1). This model has been used as a reference in a comparison between the Klobuchar model (cf. Section 3.4.6.4) and the EGNOS model (cf. Section 3.4.10). The comparison and numerical examples are given in Section 3.4.11.

3.4.10   The EGNOS ionospheric correction model

The EGNOS[16] ionospheric model is based on stochastic modelling with a triangular interpolation method. The algorithm combines physical properties of the ionosphere with stochastic features modelled on the basis of available dual frequency GPS observations. Data gathered by two NovAtel Millenium WAAS receivers was used, to

---

[16]Personal communication with my supervisor Dr. Washington Ochieng

assess the model quality as determined by data distributed by the ESTB.

3.4.10.1 Extraction of the ionospheric model from the SBAS message

The ionospheric corrections broadcast from the ESTB are contained in the SBAS message types 18 and 26 [RTCA-DO-299, 1996]. A software module developed in MatLab^{TM} during the research was used to extract and decode the necessary information from the NovAtel logs. Details on the decoding algorithm are given in Appendix A.1). The ionospheric model contains the Grid Ionospheric Vertical Delay (GIVD) for the Ionospheric Grid Points (IGP) with fixed positions as defined in RTCA-DO-299 [1996]. A quality indicator for each Ionospheric Grid Points (IGP) is also given in the form of the Grid Ionospheric Vertical Error (GIVE).

The current broadcast corrections are for the IGP's within the service volume of the ESTB. The density of these grid points decreases in higher latitudes because ionospheric activity decreases towards the poles (cf. Figure 3.13).

The current temporal resolution for the model is 5 minutes[17]. Unfortunately the broadcast GIVE indicators correspond to an applicable range error ($\sigma_{range,99.9\%}$) of 2.4 to 45 metres. This level of uncertainty exceeds the required level for kinematic applications (cf. Chapter 6). Hence the model can be used only to initialise the estimation process as described in Section 5.3. The rather insufficient level of accuracy is explained by the fact that only 8 stations contribute to the generation of the ionospheric model [Suard, 2000].

To derive the vertical delay and the corresponding error estimate for the actual pierce points, a linear interpolation algorithm in conjunction with an appropriate mapping function has been implemented and is described in Section 3.4.6.3.

Figure 3.13 depicts an example of the EGNOS based TEC values converted into vertical delays for the GPS L1 frequency. The conversion between TEC values and the corresponding range delay is realised by application of Equation 3.30. The following

---

[17]ESTB website http://www.esa.int/export/esaEG/estb.html
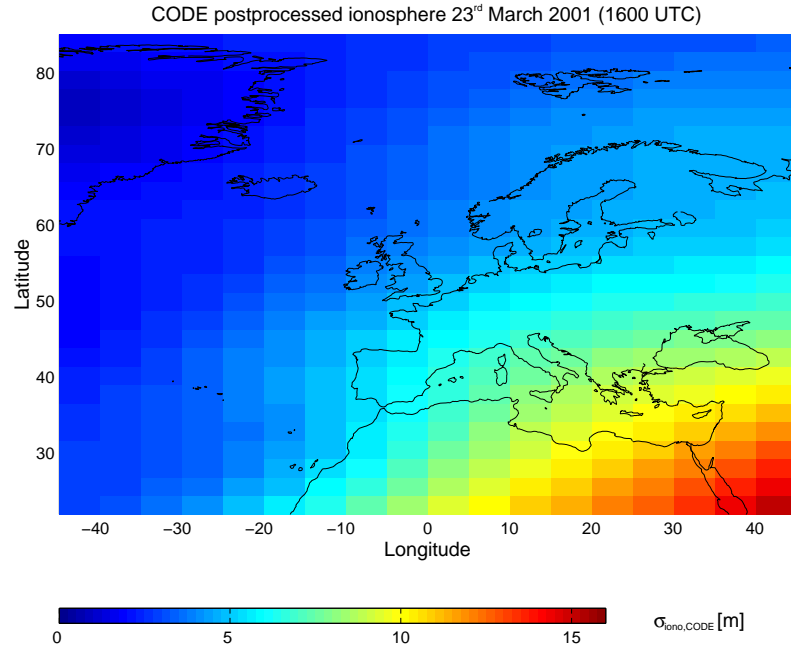
Figure 3.12: CODE post-processed ionosphere for the ECAC coverage volume for the 23rd of March 2001 (1600 UTC)

section compares the range delays applicable for L1 derived from the ionospheric models above.

3.4.11   Comparing the EGNOS and the *Klobuchar* model with the CODE model

The following figures depict ionospheric delays from the CODE model (Figure 3.12), from the EGNOS ESTB model (Figure 3.13) and the corresponding Klobuchar model (Figure 3.14). The values have been calculated for the ECAC coverage area for the 23rd of March 2001 (1600 UTC) based on a 5×1.5^o grid.

To evaluate the differences between the models above the values for the ionospheric delay (L1) have been compared for each grid point within the ESTB service volume. The CODE model has been used as reference. The values range between $-1.22m$ for the Klobuchar model and $-2.62m$ for the EGNOS model. The histograms in Figure 3.15 show the computed differences between the CODE model as reference and the Klobuchar and the EGNOS model.
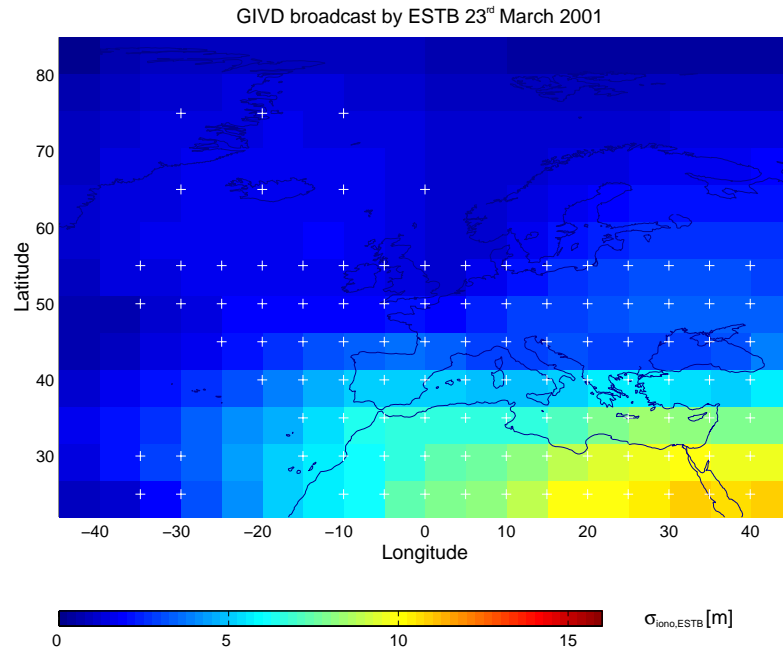
Figure 3.13: ETSB broadcasted ionosphere for the ECAC coverage volume for the 23rd of March 2001 (1600 UTC)
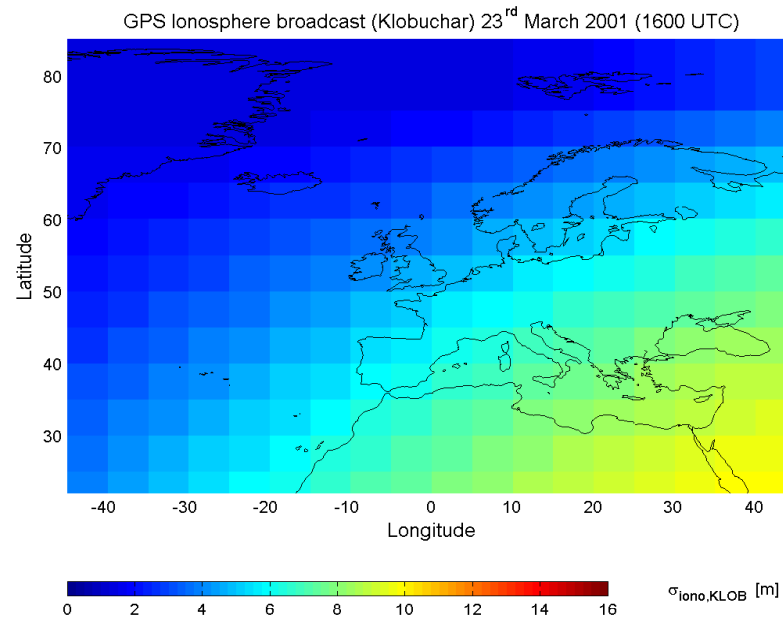
Figure 3.14: Broadcasted ionosphere based on "Klobuchar" coefficients from GPS navigation message computed for the ECAC coverage volume for the 23rd of March 2001 (1600 UTC)

The rather large value for the EGNOS model reflects the large values for the GIVE indicator as described in Section 3.4.10.

Based on this fact it has been decided to use the CODE model as reference and as initial data for the generation of the local ionospheric model to correct the single frequency EGNOS data.
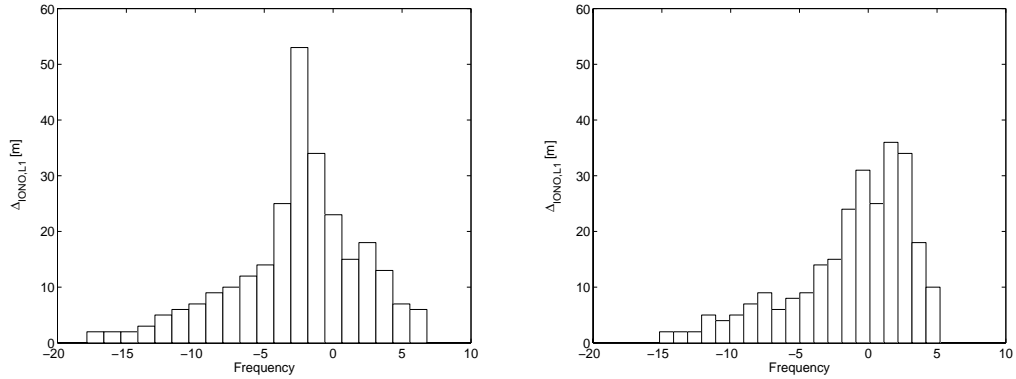
Figure 3.15: Histogram for the computed differences in metres between the CODE based model as the reference, the Klobuchar model (left) and the EGNOS-ESTB model (right)

3.4.12 Baseline length and ionospheric refraction

The differencing concepts (single and double) can be used to reduce greatly the effects of the ionosphere, because of its spatial characteristics (i.e. correlation). This is true in particular for baseline lengths of only a few kilometres (up to 30 kilometre for medium ionospheric activity). But as the baseline length increases the ionosphere decorrelates and might induce a scale bias up to several decimetres. Schaer [1999] gives an empirical formula to calculate the magnitude of the possible scale bias.

$$\delta l_{ion}[ppm] = -0.162 \frac{TEC}{R_{WGS84} \cos(E_{\min})} \tag{3.41}$$

Where
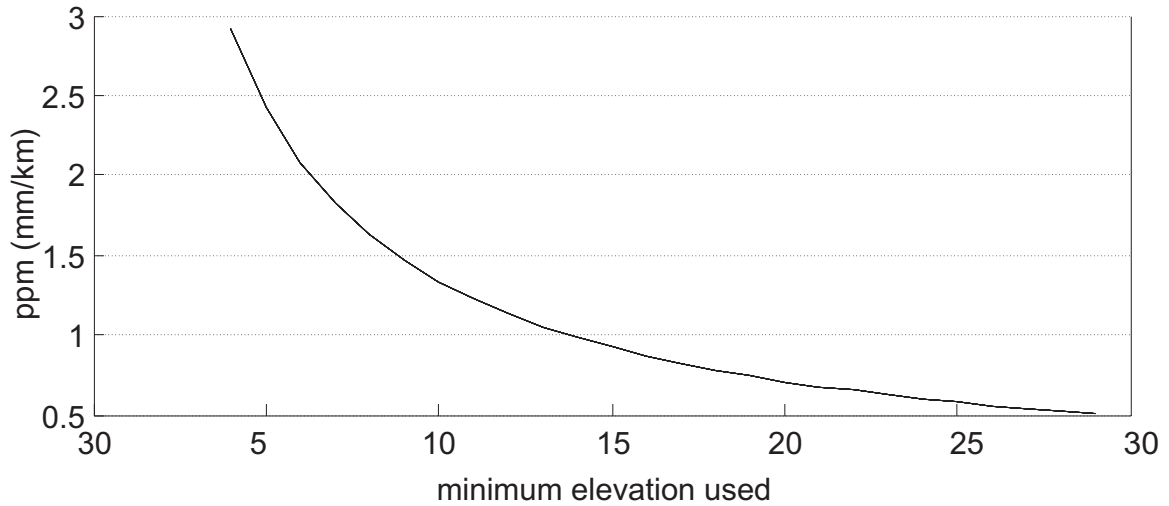
Figure 3.16: Theoretical ionospheric baseline error for single frequency solutions (L1) in ppm (mm/km) induced if the ionosphere is neglected [after Schaer, 1999]

TEC is the average vertical TEC above the baseline

R_{WGS84} is the geocentric receiver radius approx. the Earth radius

$E_{\min}$ minimum elevation angle used in the solution.

The formula has been used to calculate the theoretically induced baseline error based on a moderate TEC level of 10 TECU (in disturbed conditions such as ionospheric storm etc. this value may rise as ten times as high). Figure 3.16 shows the computed values for minimum elevation angles between 5 and 30 degrees. This theoretical consideration has been validated with results from real data in Section 6.3.

3.4.13   Summarising the ionospheric models

The ionospheric models as introduced above cover the Earth's ionosphere to different levels of spatial and temporal resolution. The accuracies of these models varies significantly. The models are available with different time delays. The CODE model is the only one which would be (in terms of accuracy) suitable for real time processing. Unfortunately, the model is only accessible after at least 24 hours data capture and

processing. Nevertheless, the model has been used to great effect in this research both for reference and to derive an ionospheric pseudo observable in the process of ionospheric filtering (cf. Section 5.2.2).

3.5 Tropospheric refraction

3.5.1 General remarks on tropospheric refraction

The troposphere is the lower part of the Earth's atmosphere, which extends from the surface to about 40 Km. It is the gaseous atmosphere where the daily weather takes place. It contains about 80% of the atmospheric mass and nearly all water vapour and clouds.

Charged particles are virtually absent and the uncharged atoms and molecules are well mixed, rendering the troposphere practically a neutral gas. Radio-wave propagation in the troposphere is non-dispersive (for the frequencies in the scope of satellite navigation). Therefore, the signal path delays due to the troposphere cannot be determined by methods relying on observations using different frequencies. The path delay has to be estimated based on the prevailing conditions within the troposphere. The main requirement is to estimate the integral of the refractive index along the tropospheric signal path as accurately as possible. This is illustrated below.

According to Seeber [1993] the tropospheric refractive index η_{tropo} (cf. Equation 3.27) can be approximated by a function of temperature, humidity and pressure.

$$\eta_{tropo} = C_1 \frac{P - e}{T} + C_2 \frac{e}{T} + C_3 \frac{e}{T^2} + ... \tag{3.42}$$

Where

$$
\begin{array}{ll}
P & \text{is the air pressure [mbar]} \\
e & \text{is the partial pressure of the water vapor [mbar]}
\end{array}
$$

$P - e$ is partial pressure of dry gas [mbar]

T is the temperature [K]

C_1, C_2, C_2 are empirically determined constants 77.64 Kmb^{-1},
-12.96 Kmb^{-1} and $3.718 \cdot 10^5$ K^2mb^{-1}

Based on Equation 3.42, the tropospheric refraction can be subdivided into a dry component (η_{dry}) and a wet component (η_{wet}). The dry part, contributing approximately 90%, of the delay can be expressed as:

$$\eta_{dry} = C_1 \frac{P - e}{T} \tag{3.43}$$

The wet part, contributing about 10%, of the delay can be expressed as:

$$\eta_{wet} = C_2 \frac{e}{T} + C_3 \frac{e}{T^2} \tag{3.44}$$

3.5.2   Models to describe the troposphere

The models to describe the troposphere can be classified into three main groups: direct methods, models that rely on surface meteorological measurements and stochastic models.

3.5.2.1   Direct methods

Such models are based on the direct measurement (along the signal path) of the tropospheric refractivity, for example using *Water Vapour Radiometers (WVR)* or *radiosondes*. Hence the tropospheric delay can be evaluated. However the physical size of the equipment and the expense involved makes this approach infeasible for practical field applications. Usually these methods are used for validation and as reference only [cf. Seeber, 1993].

3.5.2.2 Surface meteorological measurement models

Since a direct measurement of the refractivity along the signal path would be way too expensive and in many cases infeasible, *surface meteorological models* approximate the troposphere by describing its behaviour depending on height, temperature and air pressure. Examples of models that fall into this category include, the *"Hopfield"* model [cf. Hopfield, 1969] the *"Saastamoinen"* model [Saastamoinen, 1973] and the *"Black"* model [Black, 1978]. Because it is common practice the Saastamoinen model has been implemented and used in this research. According to Seeber [1993] these models may cover the wet part, depending on the weather conditions, with a standard deviation ranging between 3 to 5 cm.

3.5.2.3 Stochastic models

Furthermore it is possible to determine the tropospheric delay based on its stochastic properties. Two different approaches are described in the literature [cf. Collins and Langley, 1997; Braun et al., 2001]:

- Both entities, the dry and the wet part are treated together, and the combined contribution to the slant range delay is estimated.

- Both entities are treated separately. The dry contribution is described by well-defined deterministic expressions and the wet part, driven by the change in water vapor concentration in the atmosphere, is modelled using probabilistic laws.

Based on such an approach temporal and spatial variations can be described as functions of position and time. A tomographic approach for parametrisation as described in Section 3.4 could be applied as well. All stochastic approaches however, require initial calibration and the outcome is highly dependent on the initial values. Results from WVR's are generally used for the initial calibration. Once calibrated such models are independent from measurements of meteo- sensors

3.6   Multipath

3.6.1   General remarks on multipath

Multipath is among the major error sources in the context of GPS positioning. Multipath signals are described as signals reaching the antenna via multiple paths due to reflections, which distort the C/A-code and P-code modulations and the carrier phase observations [cf. Leick, 1995].

As a function of the geometric configuration in the vicinity of the antenna (cf. Figure 3.17) the reflected signals will be attenuated and phase-shifted. For any number of reflected signals reaching the antenna, the total signal is the result of superposition of the original and the reflected signal [cf. Hoffmann-Wellenhof et al., 1997; Raquet, 1998].

According to the description in Raquet [1998], the theoretical maximum for carrier phase multipath can reach 5cm, but for most practical application the typical values are less than one centimetre. In a similar manner to the carrier phase , in which the maximum multipath is a function of the wavelength, code range multipath is related to the length of the code (chipping rate). This relates to maximal values of code multipath of $\approx$ 3m for the C/A code and of $\approx$ 30cm for the P code.
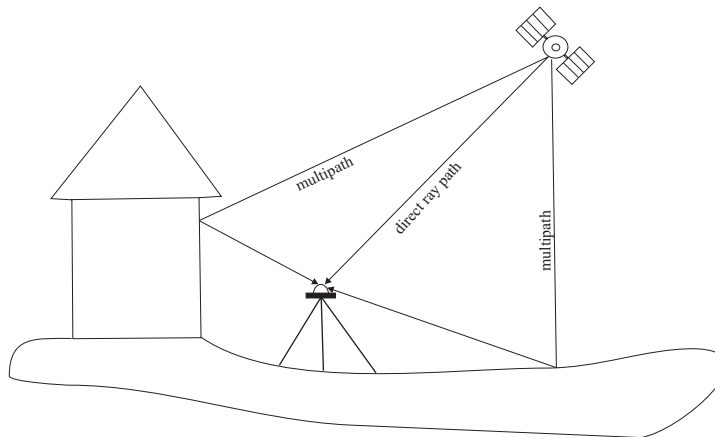
Figure 3.17: Direct and reflected ray path as the result of multipath propagation

A surface in the vicinity of the receiving antenna will cause multipath if the receiver

tracking loops are unable to distinguish between the direct and delayed signals. This occurs for the C/A-code if the difference (between the direct and delayed signals) is less than 1466ns (1.5 chips of the C/A-code) for a standard-width correlator.

The C/A-code tracking loop will reject any reflected signal which is delayed for less than $1466ns$ (which translates into a path-length difference of 440 m for the C/A-code). Any other reflected signal will cause measurement errors due to multipath [cf. Braasch, 1996, p. 559]. The carrier phase multipath is accordingly smaller since the wave length is smaller and the correlators in the tracking loop are narrower.

Multipath mitigation techniques can be categorised into hardware and software techniques.

3.6.2   Hardware techniques

Hardware techniques are either based on specific antennae design (choke-ring, extended-ground-plane) or the use of multi-antenna structures. In both cases the insensitivity to left-hand circularly polarised electro-magnetic signals is the important factor. Other antenna designs implement a gain pattern to allow the attenuation of signals below the specified antenna horizon [cf. Bisnath et al., 1997].

Furthermore, some hardware techniques are based on sophisticated correlator techniques and delay lock loops (eg. *Multipath Estimating Delay Lock Loop, MEDLL*®) to reduce the effect of multipath [cf. Dierendonck et al., 1992; Townsend and Fenton, 1994; Townsend et al., 1995]. The MEDLL® technology is implemented in the NovAtel Millennium WAAS receivers (cf. Section 6.1) used in this research. Narrower correlator spacing is implemented within the digital signal processing (DSP) unit in many receiver. Advanced receivers apply correlator spacing <0.2 chips [cf. Dierendonck et al., 1992].

Hardware based techniques are considered to be the most promising for multipath error mitigation for real-time processing.

3.6.3 Software techniques

These approaches are based on processing strategies applying physical (frequency, geometry) and mathematical (*signal-to-noise* ratio) properties within the processing software. A selection of the most important software based techniques is given below.

3.6.3.1 Techniques based on repeatability of satellite geometry

These approaches are based on long-term single antenna observations and take advantage of the repetitive GPS *"satellite-reflecting surface-antenna"* geometry for static sites to detect and remove the site multipath. Multipath templates are developed from captured data in order to mitigate the effects of multipath at static reference sites [Wanninger and May, 2000].

3.6.3.2 Techniques based on statistical properties

The *signal-to-noise ratio (SNR)* technique is used to model carrier phase multipath for real time applications. [cf. Comp and Axelrad, 1996; Barnes et al., 1998]. The SNR technique utilises the ratio of the amplitude of the recovered carrier signal-to-noise ratio and the known antenna gain pattern. Subsequently a multipath correction profile is derived and used to correct the original carrier-phase. The profile can be generated on a epoch-by-epoch basis. Thus it is not reliant on a relatively stable multipath environment.

3.6.3.3 Techniques based on frequency properties

Three different approaches can be identified here:

- **High pass filtering:** This technique assumes that ionospheric delay has a low frequency component whereas the noise-like multipath has a high frequency component. A high pass filter applied to the code/carrier differenced data can

be used to estimate the error due to noise and multipath.

- **Spectral analysis techniques**[cf. Li et al., 1993] can be used to estimate the multipath and noise in the code/carrier differenced data by evaluating the *Fourier transform* of the data and using *amplitude filtering, autocorrelation* or *decomposition* assuming different frequencies for the error components.

- **Braasch Model**[cf. Braasch, 1996] As described in Equation 3.45 the model assumes that the remaining error after estimating the ionosphere and the ambiguity can be considered as multipath. Therefore, an iterative process can be used to estimate the error due multipath and noise.

3.6.3.4   The hybrid multipath model

For this research a *hybrid* algorithm based on the Braasch model and spectral analysis have been implemented. Thus the residual multipath and noise error have been analysed for low and high frequency components.

The use of high pass filters might omit a low frequency deterministic component of multipath. The advantage of using the Braasch model in conjunction with spectral analysis in a hybrid model is its sensitivity both to short and long term deterministic multipath.

By substituting the ionospheric delay and integer ambiguity determined in an earlier step (either as an outcome from previous observations or an ionospheric estimation; cf. Section 5.2) the residual multipath error is estimated iteratively.

Based on Equation 3.2, the residual error $\delta_{multipath} + \varepsilon_\Phi$ could be evaluated as follows:

$$\delta_{multipath} + \varepsilon_\Phi = \nabla\Delta\rho - \nabla\Delta\Phi + c\left(\frac{\nabla\Delta N}{f}\right) - \nabla\Delta I \qquad (3.45)$$

Subsequently an evaluation of the residuals in the Fourier space is performed to analyse its low and high frequency components. Low frequency components are then taken as the residual long wavelength multipath error (assuming no ionospheric error)
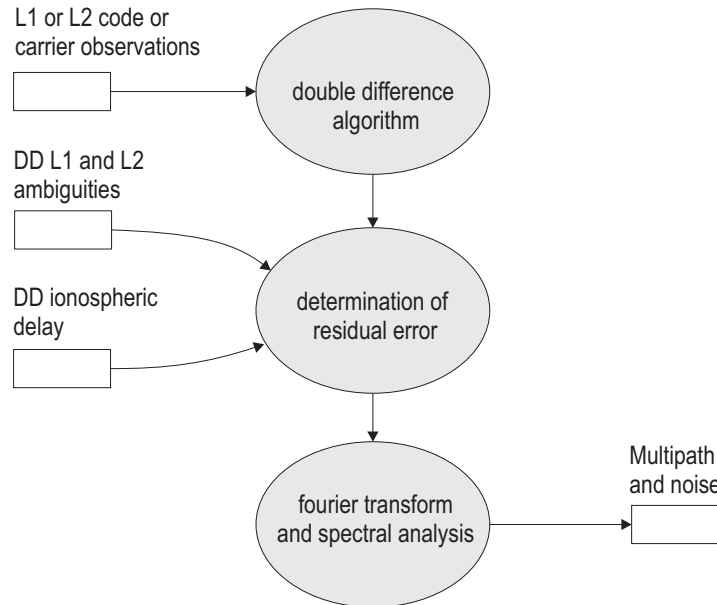
Figure 3.18: High level design of multipath analysis algorithm as implemented for the research

with the rest due to the multipath and noise.

Figure 3.18 shows a high level design of the multipath algorithm. The unknown ionospheric error and ambiguity have been evaluated in the Ionospheric Estimation Module (cf. Section 5.2.5). Subsequently they are substituted to obtain the multipath and the receiver noise. The residual errors are then analysed in the frequency domain. The algorithm has been used for both single and dual frequency data as well as with GEO data.

Finally the estimated multipath is written in a separate file containing multipath estimates for all observation types on a satellite-by-satellite and a epoch-by-epoch basis. The file is used in the final ambiguity determination module as described in Section 6.3.1.

3.7   Cycle slips

Precision kinematic positioning requires the use of the carrier-phase measurements. As described in Section 3.1.2, the carrier-phase measurement is based on the continuous determination of the receiver counter and the fractional part of the phase. Hence, after *"lock-on"*, the satellite signal should be maintained during data acquisition.

However, carrier phase measurements can be defective if the tracking is interrupted due to signal blockage, receiver failure, ionospheric scintillation or excessive multipath, resulting in cycle slips. *"True"* single-epoch ambiguity determination algorithms are immune to cycle slips (cf. Section 3.2.3). Other algorithms determining the ambiguities based on several epochs rely on observations free of cycle slips.

The issue of real-time cycle slip detection is beyond the scope of the research presented here. An assumption has been made that the data used is cycle slip free. This has been ensured by postprocessing data using Leica SkiPro software. However, a brief description of a number of approaches dealing with the detection and correction of cycle slips should be given. Further details can be found in Hoffmann-Wellenhof et al. [1997]; Teunissen and de Jong [1998].

Curve fitting and interpolation: In this approach two curves are fitted to the data one before and one after the slip occurs. Comparing these two curves could then give the value of the cycle slip. Curve fitting can be carried out using regression or least squares models [cf. Mader, 1992]. When a cycle slip is found, faulty data can be corrected by adding the slip to the subsequent measurements.

Prediction using Kalman filtering: In this method the carrier-phase measurement is predicted forward in time and then compared with the actual measurement [cf. Leick, 1995].

Utilisation of instantaneous Doppler frequency: The instantaneous Doppler frequency an be used to detect cycle slips in carrier phase measurements. This

algorithm is based on the fact that doppler measurements are immune to cycle lips.

Linear combination of L1 and L2 observations: The phase measurements on both LI and L2 frequencies can be combined so that the sensitivity of their combinations is exploited to detect the cycle-slips. The common effects cancel each other and assuming no multipath, any discrepancy can give the cycle slip value in the carrier phase measurements.

Triple differencing: Cycle slips can also be detected using the triple difference observable. This method involves differencing across receivers, across satellites and across time. This eliminates the error sources involved in positioning including the satellite and orbit errors and the ambiguity leaving only the cycle-clips.

Chapter 4

Integrated navigation using EGNOS pseudo-range observations

This chapter details the research carried out and the corresponding results of a preliminary analysis to characterise the potential of the combined use of GPS and EGNOS data for basic stand-alone navigation using pseudo-ranges. The assessment has been carried out both in the geometrical and in the positioning domain using simulated and real field environments. The results of this preliminary investigation have provided the motivation for any further research into integrated high precision kinematic positioning with carrier-phase data.

The chapter starts with an assessment based on geometry and User Equivalent Range Error (UERE). This is followed by analysis based on real data including a description of the receiver system used.

The results in the position domain are given and conclusion are made on its benefits.

4.1   Dilution of Precision(DOP) and User Equivalent Range Error(UERE) analysis

Satellite positioning accuracy depends on two main factors, the geometric strength as a result of the constellation used for position determination with respect to an unknown point and the quality of the measurements used.

The geometric strength is measured in terms of a scalar referred to as Dilution of Precision (DOP) and the measurement quality referred to the User Equivalent Range Error (UERE). The UERE represents the combined effect of all navigation system errors as seen by the user. The use of Dilution of Precision (DOP) in conjunction with the UERE provides a very good measure of potential position quality (cf. Figure 4.1). Such an assessment has been carried out in this research during a preliminary investigation into the benefits of the combined use of GPS and EGNOS pseudo-range observation for navigation.

With A representing the design matrix (see also Equation 3.15) the corresponding GDOP value is defined as

$$GDOP = \sqrt{trace(A^T A)^{-1}} \tag{4.1}$$

The associated standard deviation of the user position $\sigma_{Position}$ can be written as the product of the corresponding DOP-value (i.e. GDOP (geometric or 4-D), VDOP (vertical component), HDOP (horizontal 2-D component), PDOP (3-D positioning etc.)) and the standard deviation of the corresponding range measurement σ_{Range}

$$\sigma_{Position} = DOP \cdot \sigma_{Range} \tag{4.2}$$

The determination of the DOP values as given in Equation 4.2 requires the satellite coordinates together with the receiver coordinates to populate the design matrix A. This has been realised for the applicable GPS and EGNOS satellites (with PRN 120 and 122). The positions $(X_{WGS84}, Y_{WGS84}, Z_{WGS84})$ have been computed based on
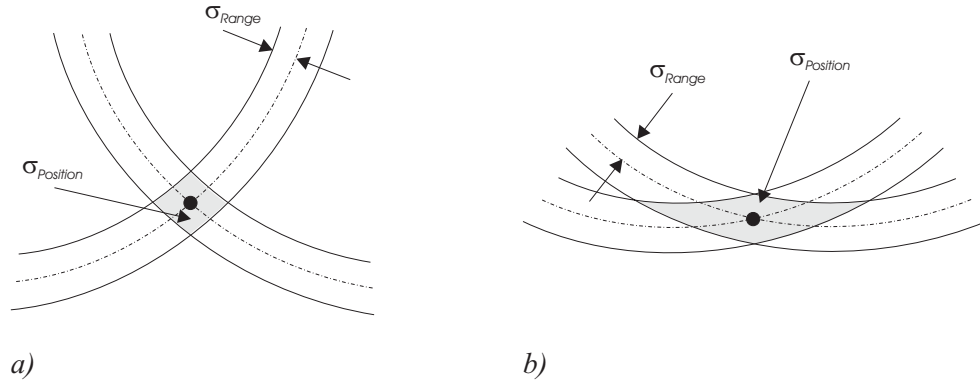
Figure 4.1: Graphical interpretation of position uncertainty $\sigma_{Position}$ and dilution of precision (DOP): a) good DOP; b) poor DOP

almanac data.

Almanac data for all GPS satellites are available in the public domain[1]. They are provided in the commonly used "YUMA" data format containing satellite information and first order orbit parameters as PRN, Health, Eccentricity e, Time of Applicability T_0, Orbital inclination δ_i, Rate of right ascension $\dot{\Omega}$, Square root of semi-major axis $\sqrt{A}$, Right ascension of ascending node Ω_0, Argument of perigee ω, Mean anomaly $\bar{M}_0$, Clock correction a_0, Drift of clock correction a_1 and the corresponding GPS week.

The orbital characteristics of the two geostationary satellites were used to derive GPS equivalent parameters (Table 4.1). They have been inserted in the corresponding GPS almanac file. This was necessary to enable GPS software to cope with EGNOS related data.

In the following two approaches temporal and spatial distributions were used to evaluate the potential impact of using EGNOS satellites (PRN 120 and PRN 122) together with GPS satellites.

---

[1]http://www.navcen.uscg.gov/ftp/GPS/almanacs/yuma/

Table 4.1: Almanac parameters for PRN 120 and 122 as used for the DOP analysis

Satellite PRN	120	122
SV Health	0	0
e	0.00	0.00
T_0 [sec]	319488	319488
δ_i [rad]	0.00	0.00
$\sqrt{A}$	6490.0	6490.0
Ω_0 [rad]	5.5911	0.2705
$\dot{\Omega}$ [rad/sec]	0.00	0.00
$\bar{M}_0$ [rad]	0.00	0.00
a_0 [$sec \times 10^{-8}$]	0.537158	2.019417
a_1 [$sec/sec \times 10^{-12}$]	-1.720216	-4.274599
week	127	127

4.1.1 Temporal distribution

This involved the computation of PDOP values over a 24-hour period (January 29 2002) for the station HUXL (situated on the roof of the TH Huxley School at Imperial College, see also Chapter 6.1). A temporal sample rate of ten minutes and a minimum elevation angle of 5 degree were used. The results can be seen in Figure 4.2.

It is clear that the additional EGNOS satellites enhance the geometrical strength of the GPS satellites for this particular station. This is particular true for those periods with weak GPS coverage and the correspondingly high PDOP values.

4.1.2 Spatial distribution

To derive a spatial distribution, DOP values have been computed on a regular grid (spatial separation 1 deg) of hypothetical user positions located within the $ECAC$ service volume (cf. Section 2.2). The DOP values have been scaled using $UERE$ budget in Table 4.2 according to expression 4.2 to evaluate a theoretical possible positioning accuracy (1σ).

The theoretical positioning accuracy values were computed for one instant in time ("$snapshot$") represented by 2:00:00 (UTC+1 on January 29th 2002. The time was
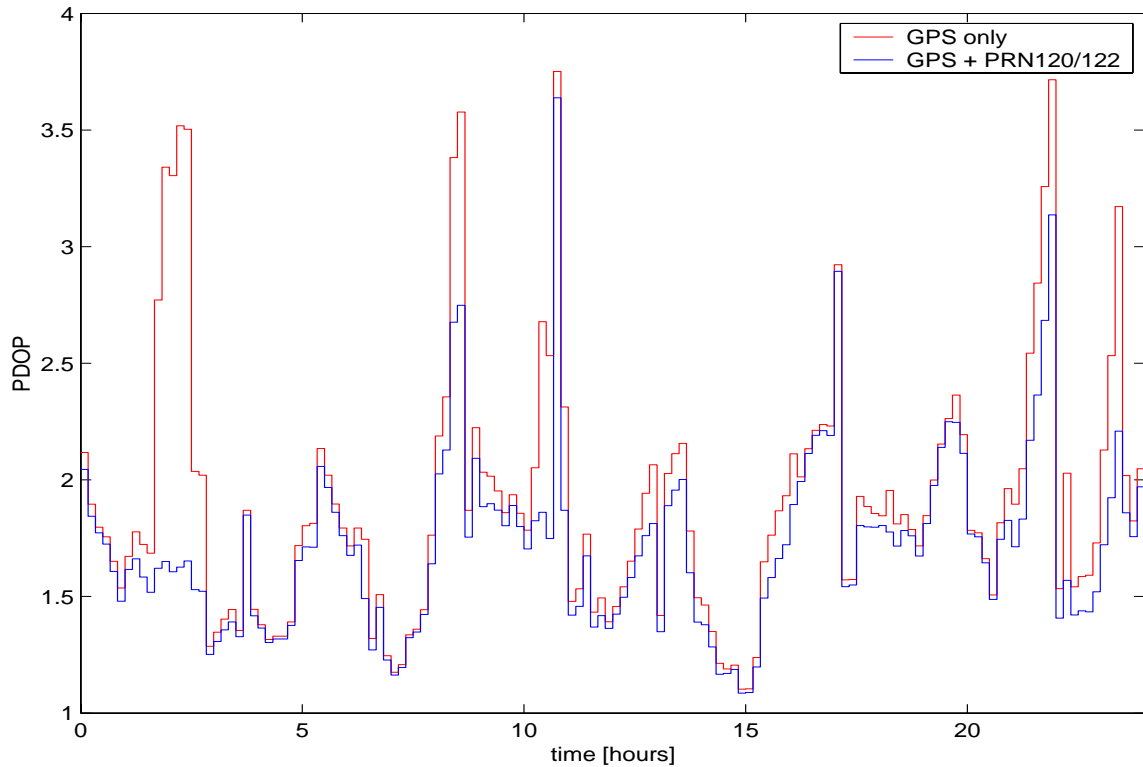
Figure 4.2: Position dilution of precision (PDOP) for the station HUXL computed over one day (January 29 2002) for GPS only(red) and for GPS+PRN120/122

chosen because the geometrical strength based on GPS only was the weakest over the particular day (see Figure 4.2).

Figures 4.3 and 4.4 show the results for GPS only and GPS plus EGNOS for the 3-D component respectively. Figures 4.5 and 4.6 show the same comparison for the 2-D horizontal component and the Figures 4.7 and 4.8 for the height component.

It is clear that the use of additional EGNOS satellites enhances the positioning accuracy of GPS satellites. A further enhancement can be expected with the full EGNOS constellation.

Table 4.3 summarises the results. Values of the theoretical positioning accuracy ($\sigma_{95\%}$) for the best possible site, the average and the worst site have been compared. For all point categories the enhancement can be seen.

Table 4.2: UERE budget for GPS satellites [cf. DoD, 2001b]

Error Source	$\sigma_{PR,GPS}$ [**m, 1** σ]		
NAV message curve fit	0.20		
Orbit	0.57		
Satellite Clock	1.43		
C/A Code Phase Bias	0.27		
Receiver Noise	0.80		
Tropospheric Error	0.25		
Ionospheric Error[a]	1.3(best site)	7(average)	14.4(worst site)
Ionospheric Error[b]	0.01	0.5	1.4
Total UERE budget (Single Freq.)	2.2	7.3	14.6
Total UERE budget (Dual Freq.)	1.7	1.9	2.3

[a]Either single frequency receiver (standard correction algorithm) or Block IIR satellites
[b]L1/L2 dual frequency receiver and Block IIF satellites

Table 4.3: Theoretical positioning accuracy for the best, the average and the worst location

		best site		average site		worst site
	GPS	GPS+2GEO	GPS	GPS+2GEO	GPS	GPS+2GEO
$\sigma_{3d,95\%}$ [m]	12.2	11.4	16.5	15.3	30.8	30.8
$\sigma_{hz,95\%}$ [m]	5.3	5.2	7.9	7	16.1	14.7
$\sigma_{vert,95\%}$ [m]	9.4	8.9	12.7	12	28.7	26.7
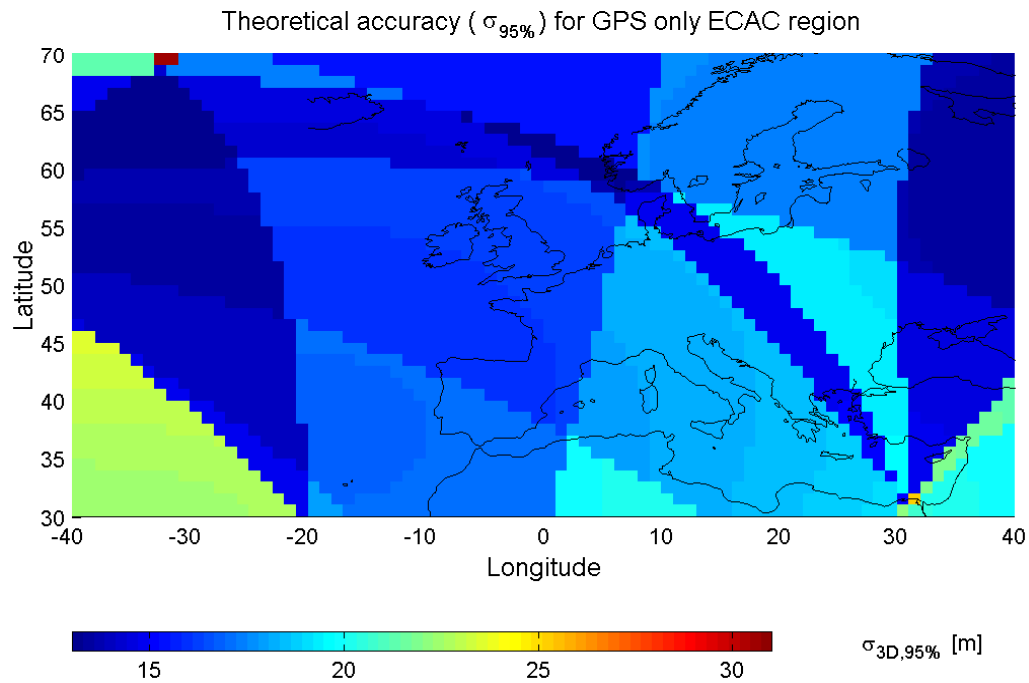
Figure 4.3: Theoretical accuracy $\sigma_{3-D,95\%}$ for ECAC service area for GPS only
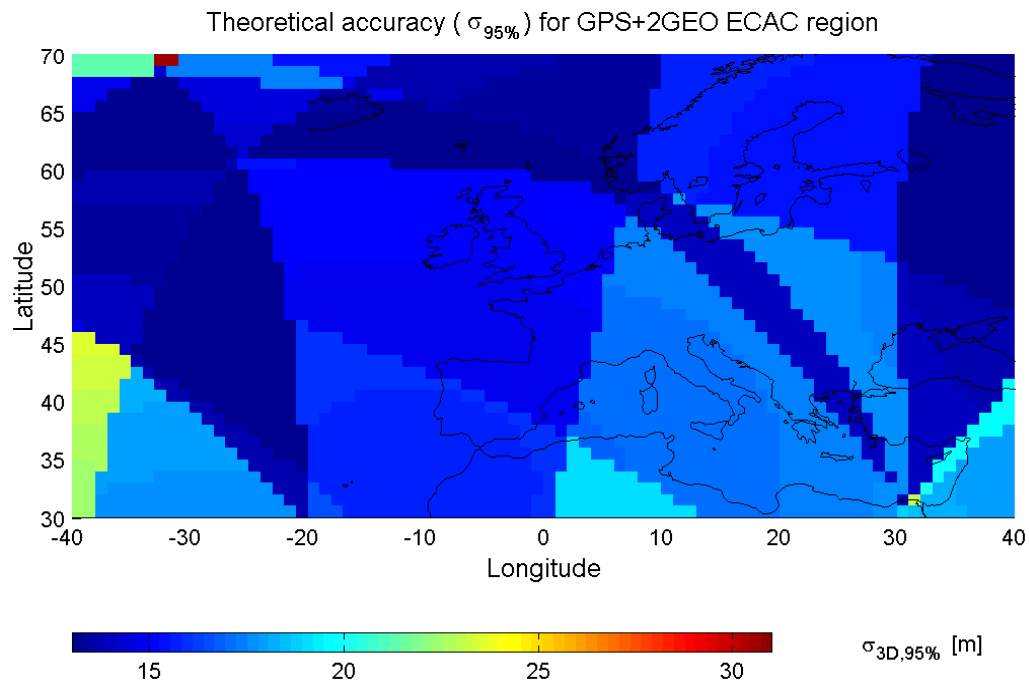
Figure 4.4: Theoretical accuracy $\sigma_{3-D,95\%}$ for ECAC service area for GPS+EGNOS (AOR-E and IOR)
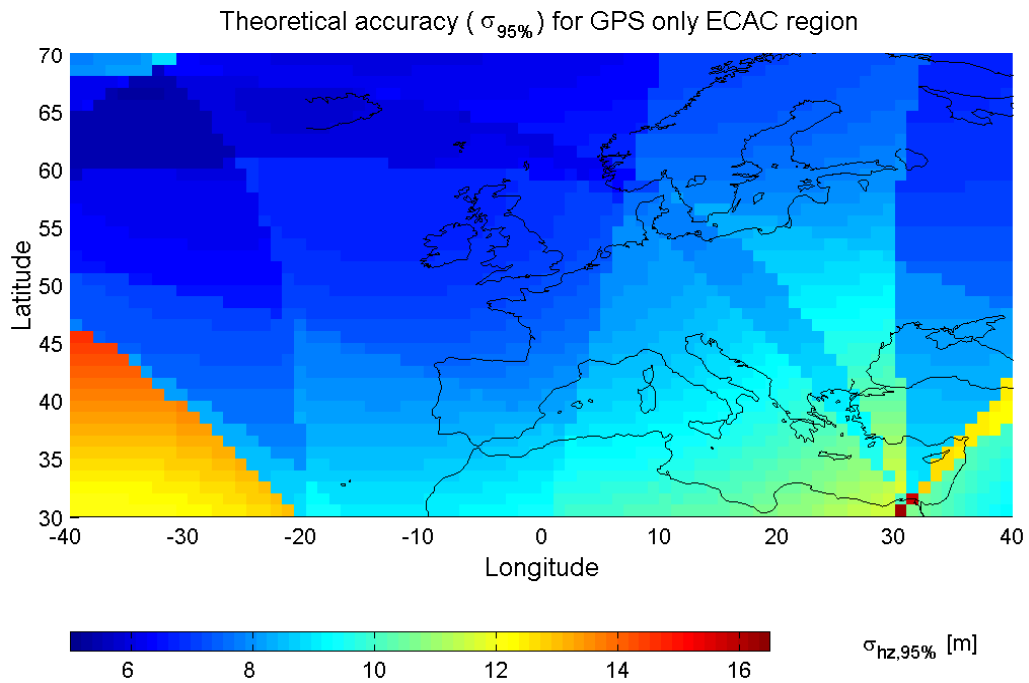
Figure 4.5: Theoretical accuracy $\sigma_{hz,95\%}$ for ECAC service area for GPS only
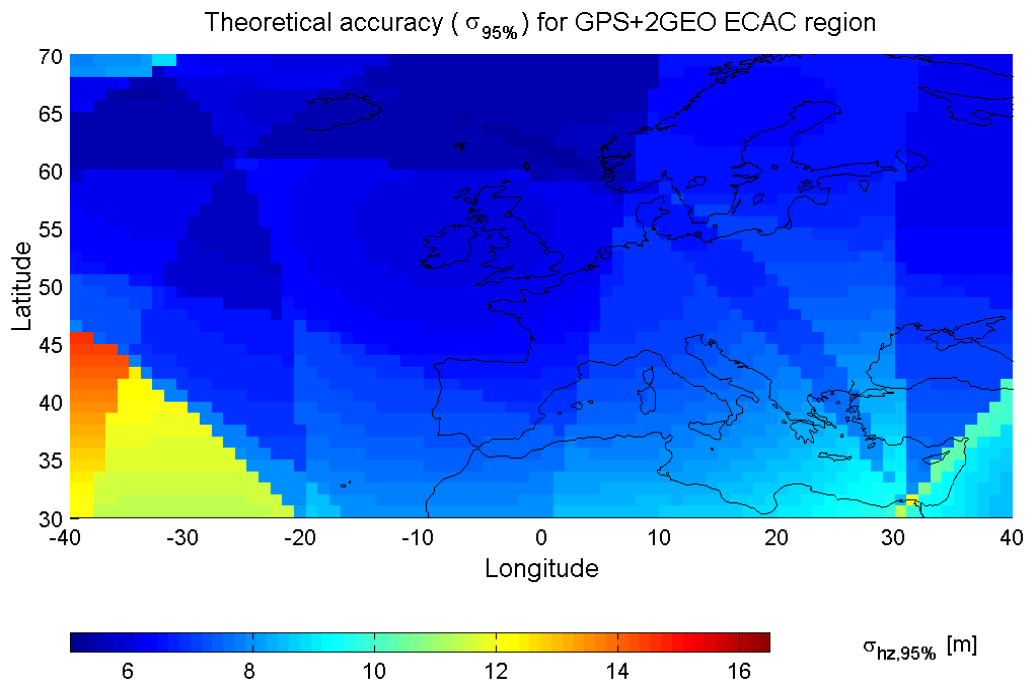
Figure 4.6: Theoretical accuracy $\sigma_{hz,95\%}$ for ECAC service area for GPS+EGNOS (AOR-E and IOR)
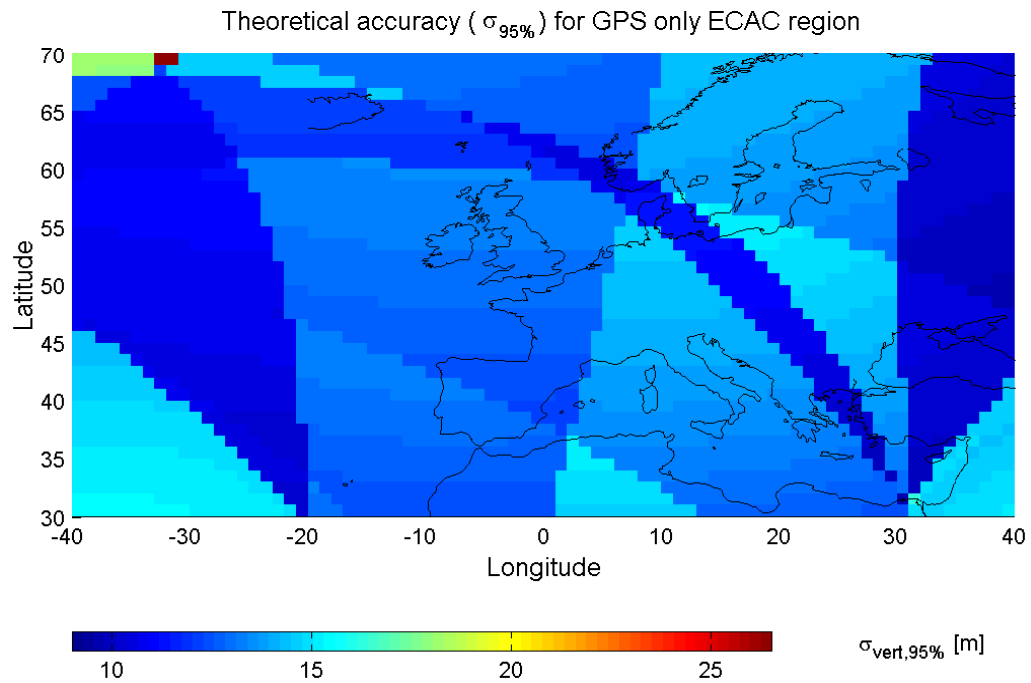
Figure 4.7: Theoretical accuracy $\sigma_{vert,95\%}$ for ECAC service area for GPS only
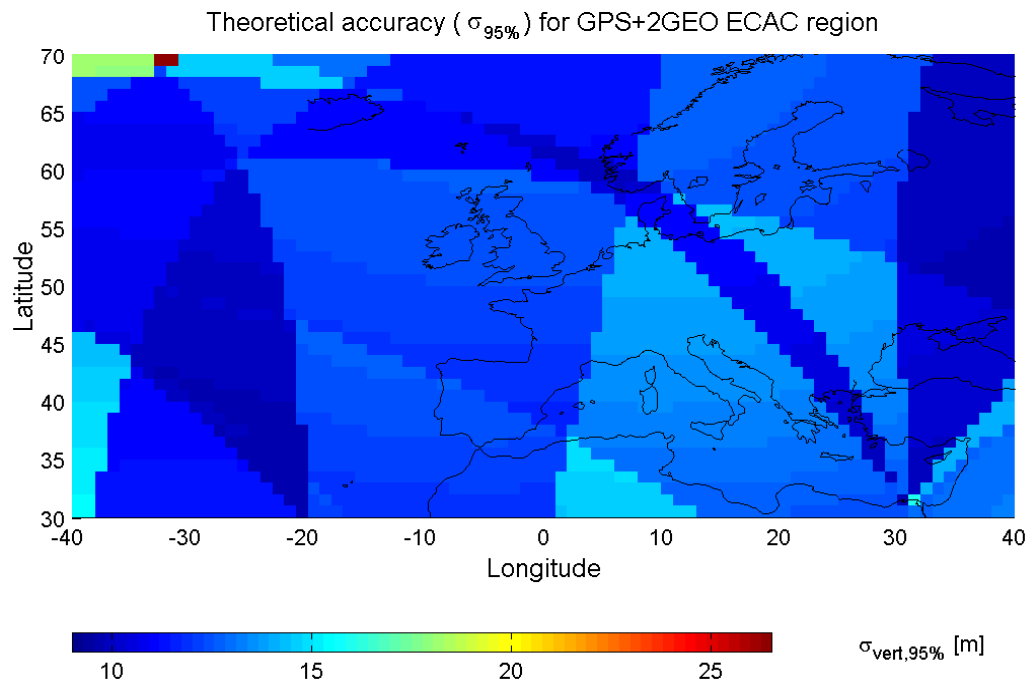
Figure 4.8: Theoretical accuracy $\sigma_{vert,95\%}$ for ECAC service area for GPS+EGNOS (AOR-E and IOR)

106

4.2 Integrated Navigation

4.2.1 The NovAtel Millennium® WAAS receiver system

Two NovAtel Millennium ® WAAS receivers were chosen for the experimental part of the navigation performance assessment. NovAtel has developed several models of SBAS-capable hardware and software solutions. These receiver systems can output the SBAS data in log format (FRMA/B, WALA/B etc. cf. Section 4.2.2), and can incorporate these corrections to generate differential-quality position solutions.

The current capability of the receivers used here include simultaneous receiving of signals from 12 GPS receivers (10 Hz position and raw data output rate) or 10 GPS and 1 SBAS L1 channel (2 Hz output). Standard SBAS data messages were analysed based on RTCA standard DO-229 (Change 1) *Minimum Operational Performance Standards for GPS/WAAS airborne equipment (WAAS-MOPS)* [cf. RTCA-DO-299, 1996].

The relevant receiver performance parameters measured by mean range measurement standard deviation and the corresponding *signal-to-noise ratio* (C/N_0; cf. Section 3.6) have been quantified in Table 4.4 [NovAtel Inc., 1997]. Whereas the C/N_0 values specify the required ratio between the received signal and the general measurement noise given in decibel(dB). These values have been used for a-priori observation weighting.

Table 4.4: Receiver performance parameters for range measurements for NovAtel GPScard(WAAS)

Frequency	Carrier-phase σ_{code}[m]	Pseudo-range $\sigma_{carrier}$[m]
L1	0.003 with $C/N_0 > 42.0dB$	0.1 with $C/N_0 > 42.0dB$
L2	0.005 with $C/N_0 > 36.0dB$	0.4 with $C/N_0 > 36.0dB$

4.2.2 Data extraction and decryption

The format of the data-logs is described in detail in NovAtel Inc. [1998]. The data log types relevant to the research are summarised below. A detailed description can be found in Appendix A.1:

Framed Raw Navigation Data ($FRMA/B): This message contains the raw framed navigation data (i.e. SBAS data). An individual message is issued for each PRN tracked. The message is updated with each acquired new frame.

Channel Range Measurements ($RGEA/B/D): This message contains the channel range measurements for currently tracked satellites. Additional information on receiver tracking status is given also.

Raw GPS Ephemeris ($REPA): This log contains the raw binary information for the GPS navigation message subframes one, two and three for the corresponding satellite [DoD, 2001b].

The data has been recorded as hexadecimal representation of the original binary data stream (i.e. a hexadecimal symbol represents a four bit sequence; F→1111). This is necessary to keep the size of the data logs on a minimum. A software module was developed to decode the data logs. Its details are given in Appendix A.1.

The software selects and decodes the necessary SBAS message typ 9 from the $FRMA/B data log. This contains the time tagged GEO satellite coordinates in form of actual positions (X, Y, Z), velocities $(\dot{X}, \dot{Y}, \dot{Z})$, accelerations $(\ddot{X}, \ddot{Y}, \ddot{Z})$ and clock parameters as offset, aging and drift (a_0, a_1, a_2). The algorithms corresponding to GPS and EGNOS orbital information have been discussed in Section 3.3.5.

4.2.3 Integrated observation data format

The code and carrier phase measurements have been recorded as $RGEA logs. The structure allows a straightforward conversion into the commonly used Receiver Independent EXchange (RINEX) format. To accommodate the three digit PRN numbers

ranging from 120 to 138 for GEO satellites, RINEX version 2.10 [cf. Gurtner, 2000] has been implemented and adapted slightly (cf. Appendix B).

4.2.4 Weighting scheme of pseudo-range observations

The standard least square estimator used for the navigation solution applies a specific scheme to assign a specific a-priori weight to each GPS and GEO pseudo-range observation, used. The a-priori variance-covariance matrix Q_{xx} has been populated as follows.

$$Q_{xx} = \begin{bmatrix} \frac{1}{\sigma_{PR,1}^2} & & & & \\ 0 & \frac{1}{\sigma_{PR,2}^2} & 0 & \cdots & 0 \\ 0 & 0 & \frac{1}{\sigma_{PR,3}^2} & \cdots & 0 \\ \vdots & \vdots & \vdots & \ddots & \vdots \\ 0 & 0 & 0 & \cdots & \frac{1}{\sigma_{PR,i}^2} \end{bmatrix} \qquad i = Number\ of\ satellites \qquad (4.3)$$

Where $\sigma_{PR,i}$ denotes the standard deviation of the corresponding pseudo-range. It has been computed as sum of the squares of all given navigation error components. The single components are given in Table 4.2 for GPS satellites and in Table 4.5 for the GEO satellites respectively. The multipath, the ionospheric and the tropospheric components are scaled according to the elevation angle of the satellite .

Table 4.5: UERE budged for GEO satellites

Error Source	$\sigma_{PR,GEO}$ [m, 1 σ]		
GEO Satellite Clock and Orbit	1.00		
C/A Code Phase Bias	0.27		
Receiver Noise	0.80		
Tropospheric Error	0.25		
Ionospheric Error	1.3(best site)	7(average)	14.4(worst site)
Total UERE budget (Single Freq.)	1.8	7.1	14.4

Geodetic
calculations

Standard ionospheric
correction

Standard tropospheric
correction

L1 Pseudo-
ranges

Forming
observation
equations

Evaluate ionospheric
and tropospheric
corrections

Integrated
orbit file

Forming normal
equations

LSQ -solver

Computation
of positions
and residuals
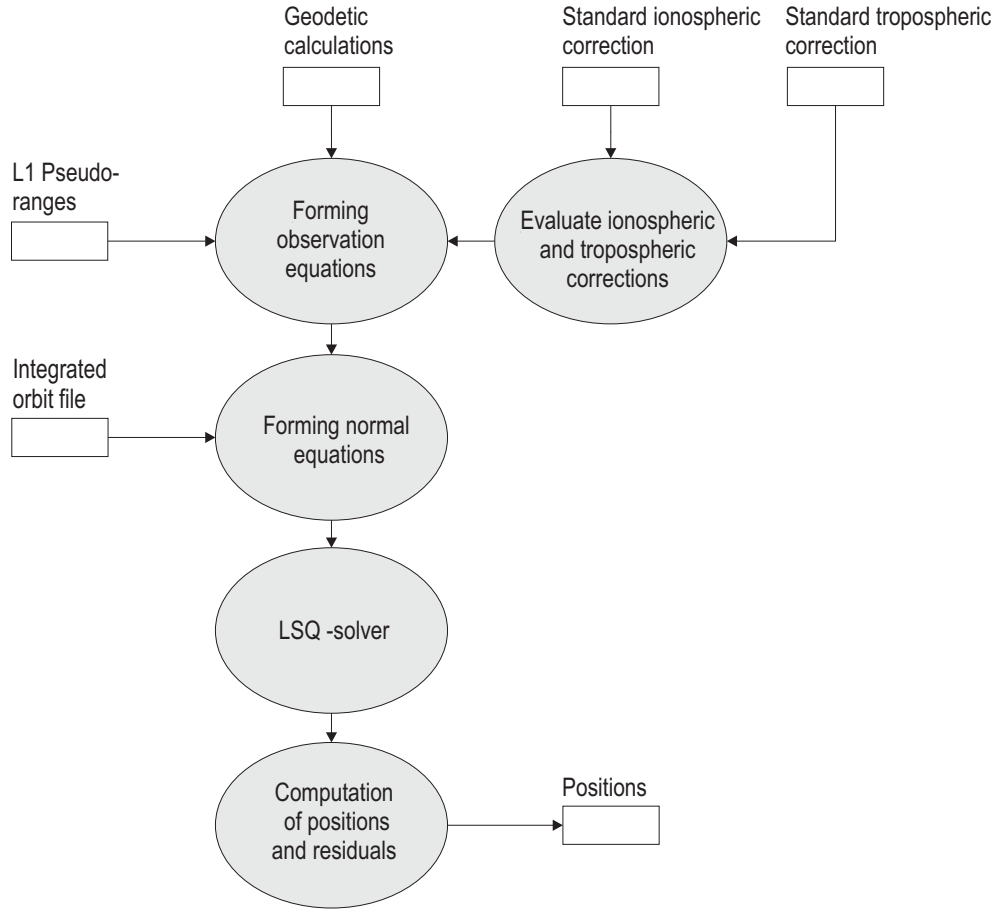
Positions

Figure 4.9: High level design of navigation and single point positioning module
implemented for the research

4.2.5   Numerical results

With an integrated orbit and observation file format determined as described above
it was possible to process both GEO and GPS data to determine single point position
solutions. 15 hours of data were processed in a epoch-by-epoch mode to simulate a
moving receiver.

Figure 4.9 shows the high level design of the navigation and single point positioning
module developed and tested.

The standard single frequency ionospheric model (cf. Section 3.4.6.4) has been
used. For the troposphere several correction models have been implemented (cf.

Section 3.5). The shown results are based on the *"Saastamoinen-model"*.

Three scenarios where set up to evaluate the potential impact of the use of additional EGNOS data. These scenarios should reflect the differences in the user environment as possible in the open space and under harsh engineering conditions where several satellites are blocked due to surrounding obstacles.

- **Scenario I** Utilisation of all available satellites including PRN 120 above the minimum elevation of 5 degree. Figure 4.10 gives the results showing that, with 10-11 satellites simultaneously tracked, the differences between the fixed point and the computed positions are gaussian distributed and only seldom excess ±10 metres.

- **Scenario II** Approximately 50% of the GPS satellites have been blocked. The results are visualised in Figure 4.11.

- **Scenario III** Approximately 50% of the GPS satellites have been blocked. Additionally PRN 120 has been used. The results are visualised in Figure 4.12.

Using all satellites in view did not show a significant impact on the navigation solution. But blocking 50% of all GPS satellites has proven the benefit of using additional GEO ranges. The results have been summarised in Table 4.6 and in Figure 4.10-4.12. The standard deviations ($\sigma_{95\%}$) in Table 4.6 show the significant gain from including PRN 120 (AOR-E) in the navigation solution.

Table 4.6: Comparison ($\sigma_{95\%}$) of different observation scenarios using GPS and EGNOS epoch-by-epoch pseudo-ranging

	all available SV	GPS(only, 50% blockage)	GPS(50% blockage) + PRN 120
$\sigma_{north,95\%}[\mathrm{m}]$	2.15	3.75	3.74
$\sigma_{east,95\%}[\mathrm{m}]$	2.10	4.20	3.74
$\sigma_{height,95\%}[\mathrm{m}]$	5.40	8.75	6.00
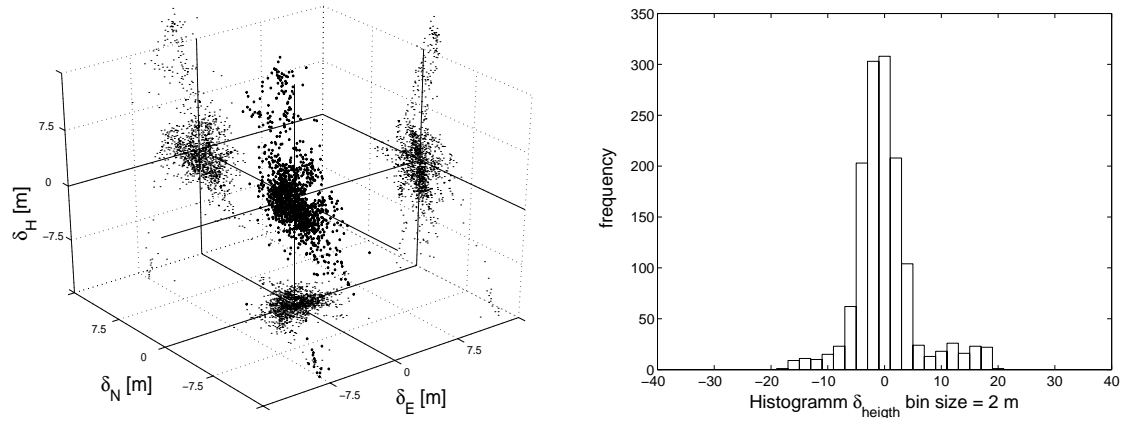
Figure 4.10: 3-D scatter plot(left) and frequency in δ_{height} (right) of deviation [m] from fixed position Scenario I
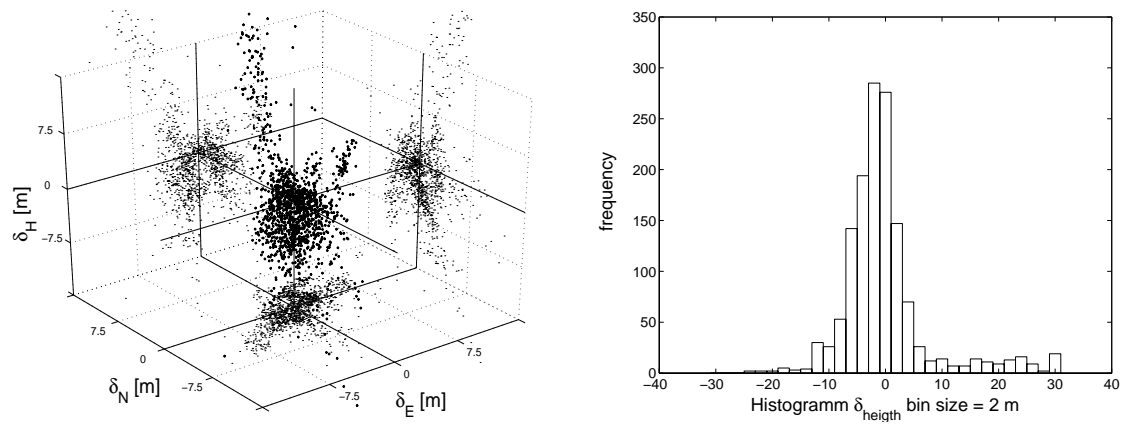
Figure 4.11: 3-D scatter plot(left) and frequency in δ_{height} (right) of deviation [m] from fixed position Scenario II
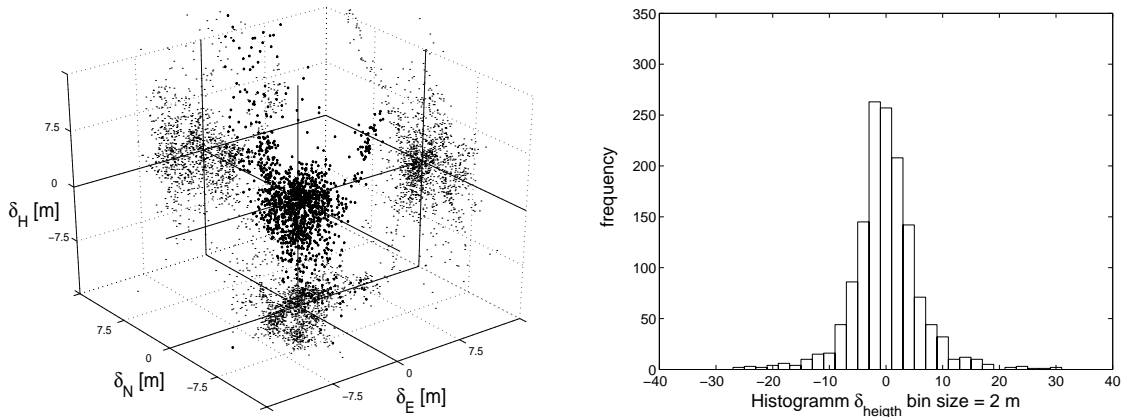
Figure 4.12: 3-D scatter plot(left) and frequency in δ_{height} (right) of deviation [m] from fixed position Scenario III

4.3   Integrated navigation - conclusion

This chapter has shown that based on a theoretical analysis a considerable enhancement can be expected if EGNOS satellites are included in the navigation solution. This finding has been proved with the processing of real data as captured by a NovAtel Millennium WAAS receiver on a qualitative level. The reasons for significant quantitative differences between both results can be seen in the conservative assumptions about standard navigation system errors as specified in DoD [2001b].

The promising findings in this chapter were the justification to continue with the research into the application of carrier-phase measurements for high precision kinematic processing as described in the chapters to follow.

Chapter 5

Integrated near real-time ionospheric prediction

Chapter 3 Section 3.4 presented a detailed discussion of the physical and mathematical properties of the Earth's ionosphere. This chapter documents the research effort to determine ionospheric slant delays applicable to the single-frequency EGNOS carrier-phase observations at a sufficient level of accuracy. It introduces a new approach for near real-time ionospheric prediction and parametrisation. This includes preliminary evaluations of various methods to parameterise 2-D models based on sparsely distributed data sets. A particular focus is set on the optimal use of all available ionospheric information, including a detailed assessment of the performance and the relevance of each existing externally derived ionospheric model.

5.1   The new approach for real-time ionospheric prediction

A key requirement for the combined use of GPS and EGNOS data is the capability to account for the error introduced by the effects of the ionosphere. In order to carry out kinematic positioning, a model that can be used reliably and accurately is required.

The model proposed is based on a sparse GPS dual frequency data set as it would be encountered in a localised single baseline kinematic positioning augmented with

data from existing ionospheric models. The approach implemented and evaluated is based on the following main steps.

- **Preprocessing:** This includes data extraction and decoding (cf. Section 4.2.2), outlier and cycle-slip detection (cf. Section 3.7), orbit computation and integration (cf. Section 3.3.4.2). These tasks are not discussed further as they are common practice in GPS processing. Details can be found in various textbooks such as Hoffmann-Wellenhof et al. [1997], [Leick, 1995] and Rothacher and Mevart [1996].

- **Derivation of the ionospheric pseudo- observable:** This involves spatial and temporal interpolation to include an externally derived ionospheric model to augment the sparse GPS data.

- **Ionospheric filtering:** This involves the application of a weighted Kalman filter approach to determine ionospheric slant delays for all suitable GPS satellites based on dual frequency code and carrier-phase observations. This is realised at various levels of observation *"differencing"*. Furthermore, a *signal-to-noise* ratio analysis of the data used is carried out to evaluate a suitable *"state transition matrix"* for different application scenarios.

- **Ionospheric prediction:** This involves the application of a suitable prediction algorithm to determine the ionospheric delay in cases of satellite blockage and extended cycle slip occurrence. A 3rd-order polynomial regression algorithm has been implemented and evaluated.

- **Ionospheric mapping:** This involves the application of a suitable mapping function to transform slant delays to vertical delays and vice versa.

- **Ionospheric parametrisation and interpolation:** This step determines the slant ionospheric delays for the single frequency satellites (i.e. GEO's) using a 2-D bi-harmonic spline model.

The functional architecture of the software implemented is illustrated in Figure 5.1 [cf. Sauer and Ochieng, 2002a]. The flow-chart is in accordance with the steps as described above. Furthermore the following section presents the details of the algorithms, their evaluation, implementation and validation. The steps in the dotted box (Figure 5.1) are treated in detail in this chapter.
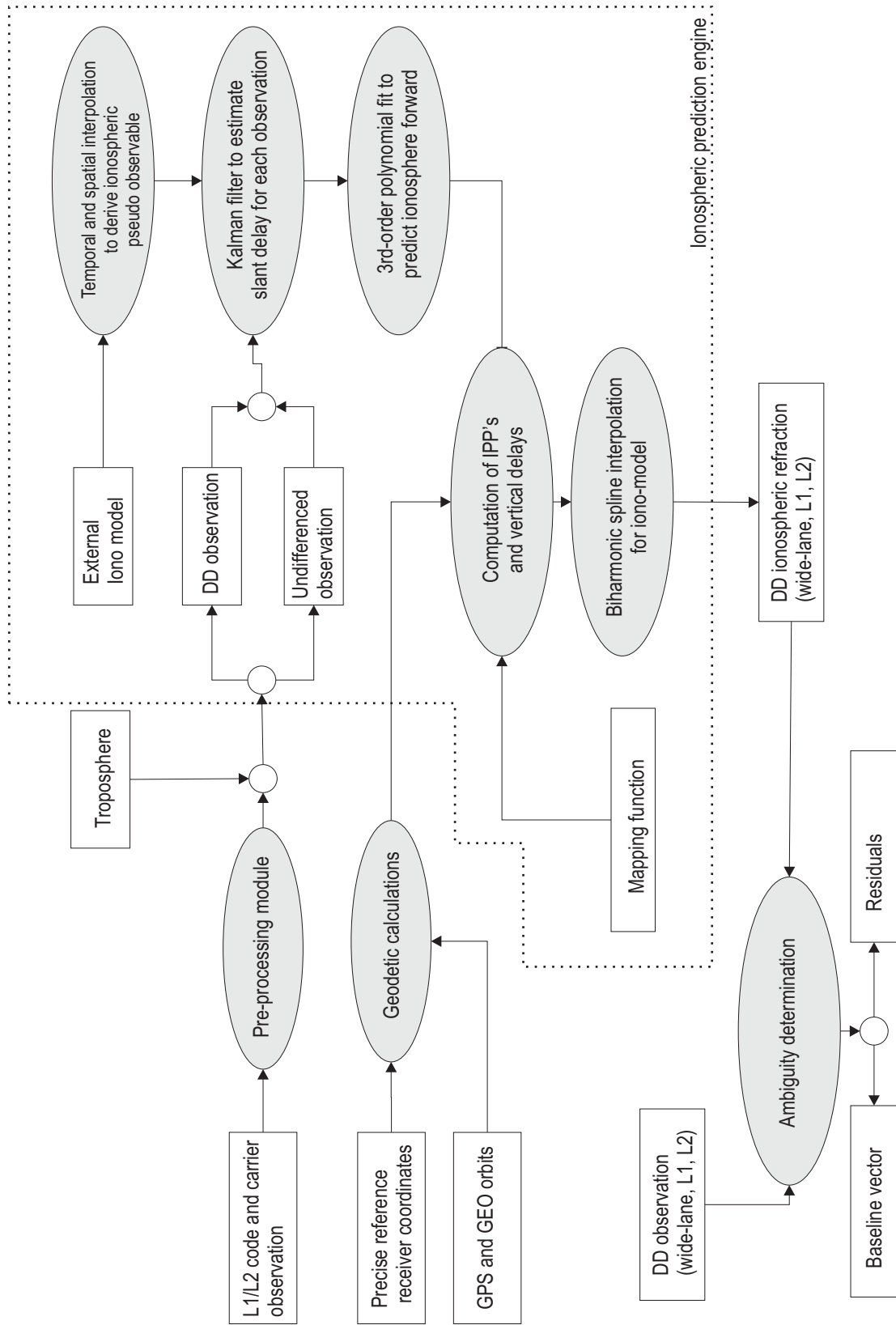
Figure 5.1: A high level design of the ionospheric parameterisation algorithm [cf. Sauer and Ochieng, 2002a]

5.2   Ionospheric estimation using LSQ filters

5.2.1   Random processes and Least-squares filter theory

The idea of using different sequential least squares (LSQ) filtering techniques such as *Kalman* and *Bayesian* filters for processing GPS observations was first proposed by Brown and Hwang [1983]. Other authors [eg. Goad, 1990; Euler and Goad, 1991; Goad, 1992; Gross et al., 1998; Mohamed and Schwarz, 1999] subsequently refined the idea and discussed various aspects of LSQ filtering within the context of GPS positioning based on carrier-phase observations.

A general introduction to Kalman filters is given by Welch and Bishop [2002]. More extensive discussions about the theory of filtering in optimal estimation can be found in Gelb [1974]; Brown and Hwang [1997]; Strang and Borre [1998]. LSQ filtering is based on a sequential adjustment utilising statistical properties of a previous estimation step. The statical properties of the current epoch are governed by the statistical properties of the preceding one. The basic concept of LSQ filtering is depicted in Figure 5.2. Note that the terminology in Figure 5.2 is based on a variety of literature about LSQ filtering and differs slightly from the "normal" least-squares terminology (cf. Section 3.2.3).

As shown in Figure 5.2, the Kalman filter estimates a process by using a form of feedback control, where the filter estimates the "*process state*" at some time $(k-1)$ and then obtains a feedback in the form of (noisy) measurements. Hence, the equations for the Kalman filter fall into two groups: *time update equations* and *measurement update equations*. The time update equations are responsible for projecting forward (in time) the current state and error covariance estimates to obtain the *a-priori* estimates for the next time step. The measurement update equations are responsible for the feedback (i.e. incorporating a new measurement into the *a-priori* estimate to obtain an improved *a-posteriori* estimate (k). The level of influence between prediction and update is controlled by the Kalman gain matrix.

Using the annotation as given below, the following linearised system of observation
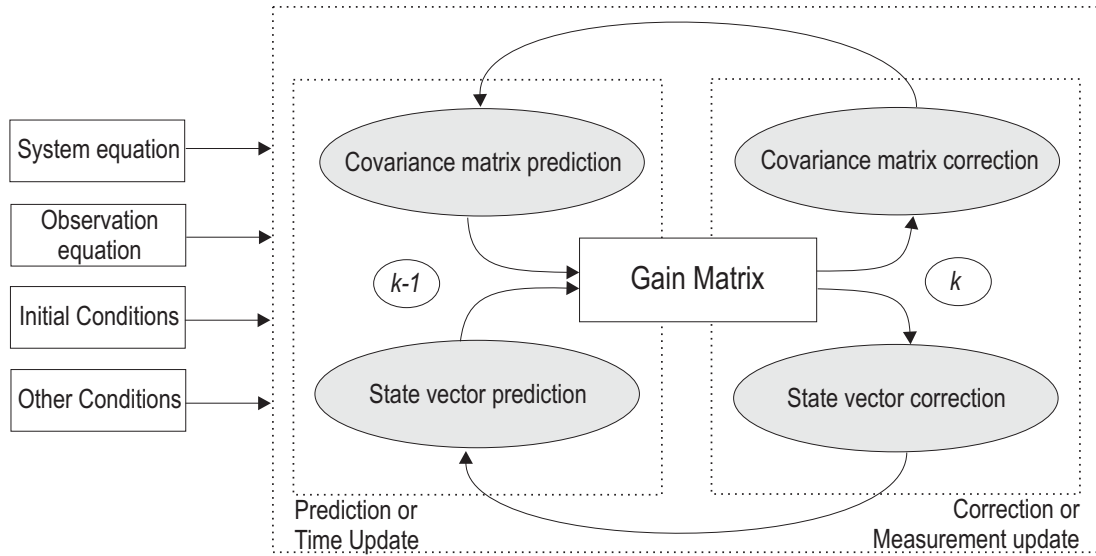
Figure 5.2: Basic principle for recursive LSQ filters

equation give the start to a complete picture on the actual filter. These equations are discussed again within the scope of filtering for the ionospheric slant delay and the wide lane ambiguities in Section 5.2.2.

System equation:

$$x_k = F_{k-1}x_{k-1} + \epsilon_k \qquad \epsilon_k \sim N(0, Q_{\epsilon,k}) \tag{5.1}$$

Observation equation:

$$b_k = A_k x_k + e_k \qquad e_k \sim N(0, Q_{e,k}) \tag{5.2}$$

The following sequence of filter equations reflects the algorithm flow as implemented in code.

State Vector Prediction:

$$\hat{x}_{k|k-1} = F_{k-1}\hat{x}_{k-1|k-1} \tag{5.3}$$

Variance-covariance matrix prediction:

$$P_{k|k-1} = F_{k-1}P_{k-1|k-1}F_{k-1}^T + Q_{\epsilon,k} \tag{5.4}$$

Kalman gain matrix computation:

$$K_k = P_{k|k-1}A_k^T(A_kP_{k|k-1} - A_k^T + Q_{e,k})^{-1} \tag{5.5}$$

State vector update/correction:

$$\hat{x}_{k|k} = \hat{x}_{k|k-1}K_k(b - A_k\hat{x}_{k|k-1}) \tag{5.6}$$

Variance-covariance matrix update/correction:

$$P_{k|k} = (I - K_kA_k)P_{k|k-1} \tag{5.7}$$

The annotation used is based on Strang and Borre [1998].

Where

k	epoch or time index
A_k	is the design matrix describing functional relationships
F_k	State transition matrix describes the relationship between two consecutive states
b_k	Vector of observations
x_k	State vector (unknown) to be estimated
ϵ_k	System or process noise
e_k	Observation noise
K_k	Gain matrix
$Q_{\epsilon,k}$	System or process variance-covariance matrix
$Q_{e,k}$	Measurement variance-covariance matrix
$P_{k|k-1}$	a-priori variance-covariance for the estimate $\hat{x}_{k|k-1}$

$P_{k|k}$ a-posteriori variance-covariance for the estimate $\hat{x}_k$

$\hat{x}_{k|k-1}$ a-priori state updates as overall solution in the least-quare estimation

$\hat{x}_{k|k}$ a-posteriori state updates as overall solution in the least-quare estimation

5.2.2 Geometry free observation model and filter design

An important contribution of this research is the utilisation of LSQ filters to determine the ionospheric delays based on GPS dual-frequency code and carrier observation in conjunction with an externally derived ionospheric *"pseudo observable"*. The idea of deriving ionospheric information and preliminary ambiguities originated in the approach as published by Euler and Goad [1991] relies on the availability of high quality dual frequency P-code (not ordinarily accessible for civil use, see Table 2.2) and carrier-phase observations.

The approach by Euler and Goad [1991] has been extended in this research by the application of a numerically more efficient Kalman filter. Furthermore an enhanced filter initialisation process using available external ionospheric models as described in Section 3.4.8 has been developed.

The data used in the research presented is based on dual-frequency L1 C/A, L2 P code and L1/L2 carrier-phase observations. Since the paper by Euler and Goad [1991] was published, the quality of pseudo-range measurements has improved significantly. Section 5.2.3 includes a statistical quality assessment of the data sets, used, and justifies the role of pseudo-range observations in estimating ionospheric slant delays.

At this point it is important to recall the relevant observation equations based on a geometry free observation model [Teunissen, 1997]. These have been discussed at a general level in Sections 3.1.1 and 3.1.2. The approach taken to model the effect of the ionosphere divides it into two parts, a deterministic part $I_{i,0}$ and a stochastic

part $I_{i,\xi}$ [cf. Sauer and Ochieng, 2002a,b].

Deterministic or trend components: The deterministic part, denoted by $I_{i,0}$ represents the part of the ionospheric delay following a relatively simple model. It can be interpreted as long-term ionospheric behaviour.

Stochastic or signal components: The stochastic part, denoted by $I_{i,\xi}$ represents the part of the ionosphere with short-term behaviour. This can be interpreted as a stochastic or signal component.

The corresponding observation equations can be written in the following manner (for the annotation of commonly used terms see Equation 3.1.2).

$$\Phi_{i,1}^k(t) = \rho_i^k - (I_{i,0}^k + I_{i,\xi}^k) + \lambda_1 N_{i,1}^k + \varepsilon_{i,\varphi,1}^k \tag{5.8}$$

$$\Phi_{i,2}^k(t) = \rho_i^k - \xi(I_{i,0}^k + I_{i,\xi}^k) + \lambda_2 N_{i,2}^k + \varepsilon_{i,\varphi,2}^k \tag{5.9}$$

$$PR_{i,1}^k(t) = \rho_i^k + (I_{i,0}^k + I_{i,\xi}^k) + \varepsilon_{i,PR,1}^k \tag{5.10}$$

$$PR_{i,2}^k(t) = \rho_i^k + \xi(I_{i,0}^k + I_{i,\xi}^k) + \varepsilon_{i,PR,2}^k \tag{5.11}$$

Where

$$\xi \qquad = \left(\frac{f_1}{f_2}\right)^2$$

The division into deterministic and stochastic part enables the derivation of an ionospheric trend which can be used to predict the ionospheric delay. A further observable referred to as the ionospheric *"pseudo-observable"*, $I_{external}$, has been introduced based on an externally derived model (cf. Section 3.4.9). The corresponding observation equation for this observable can be written as.

$$I_{k,external} = (I_{i,0}^k + I_{i,\xi}^k) + \varepsilon_{i,iono}^k \tag{5.12}$$

Where

$$\varepsilon_{i,iono}^{k} \qquad \text{is the ionospheric uncertainty introduced by the external model}$$

As well as the *a-priori* uncertainty for the code- and carrier-phase observations an *a-priori* uncertainty is assigned to the ionospheric observable. This is realised using an appropriate variance-covariance matrix. The strategy for populating the corresponding variance-covariance matrices is described in Section 5.2.4.

In order to account for the temporal correlation between the observations at the epochs t and $t+1$ the Kalman gain matrix is modelled accordingly. The approach used for this is given in Section 5.2.5.

As already stated, combining code and carrier-phase measurements for modelling ionospheric delays as proposed requires good quality pseudo-range observations on both frequencies. The following section gives a detailed analysis of the code and carrier-phase observations used. The quality of the externally derived ionospheric observable is described in Section 3.4.9.

5.2.3   Code and carrier noise analysis

Good quality code measurements on both frequencies are required to model the effect of the ionosphere as proposed. Although the quality of carrier-phase measurements is vital too, the focus at this point is on the code measurements since their noise level is usually one order of magnitude larger. Three different criteria have been used to evaluate the quality of code- and carrier-phase measurements.

- The evaluation of satellite specific Differential Code Bias (DCB) values as published within the scientific community. In the literature DCB is also referred to as hardware or inter channel bias.

- The computation and evaluation of code- and carrier-phase residuals based on postprocessing of stations with long observation times ($> 15h$).

- Extraction and evaluation of receiver generated *signal-to-noise ratio (snr)* levels and observation type specific values for measurement standard deviations.

5.2.3.1 Differential Code Biases (DCB)

The Differential Code Bias (DCB)es are particularly important for *"one-way"* linear combinations between L1 and L2 code measurements. Usually they have to be treated as unknowns in the system of equations. In the case of short term application for ionospheric mapping (observation time spans of $\approx 1h$), it is sufficient to consider them as white gaussian noise and to *"lump"* the DCB with the system noise as estimated in the Kalman filter state (cf. Section 5.2.5). Calibrated high performance scientific or military receivers are capable of measuring the receiver DCB directly.

In case of long term ionospheric mapping and prediction as published for example by Komjathy [1997] and Schaer [1999], satellite and receiver DCB are also of importance since they give valuable information about the long-term stability of the receiver and satellite time standards. Daily DCB values are published together with the TEC values in IONEX files by CODE.

Although the use of satellite DCB published by several international agencies such as CODE or JPL could be valuable for this research a simpler approach based on a weighting mechanism (cf. Section 5.2.4) was considered to be sufficient to account for the corresponding level of uncertainty.

Figure 5.3 shows the level of the mean DCB and the corresponding *RMS* values as published by *CODE* for the period of the measurement campaign between March 21 - March 30 2001 (cf. Section 6.1). It can be seen that the values range between -3 and 4 nanoseconds. One reason for the different values is the fact that different generations of space craft carrying time standards with different levels of performance.

Values for the receiver DCB can be determined as well. But this requires extensive
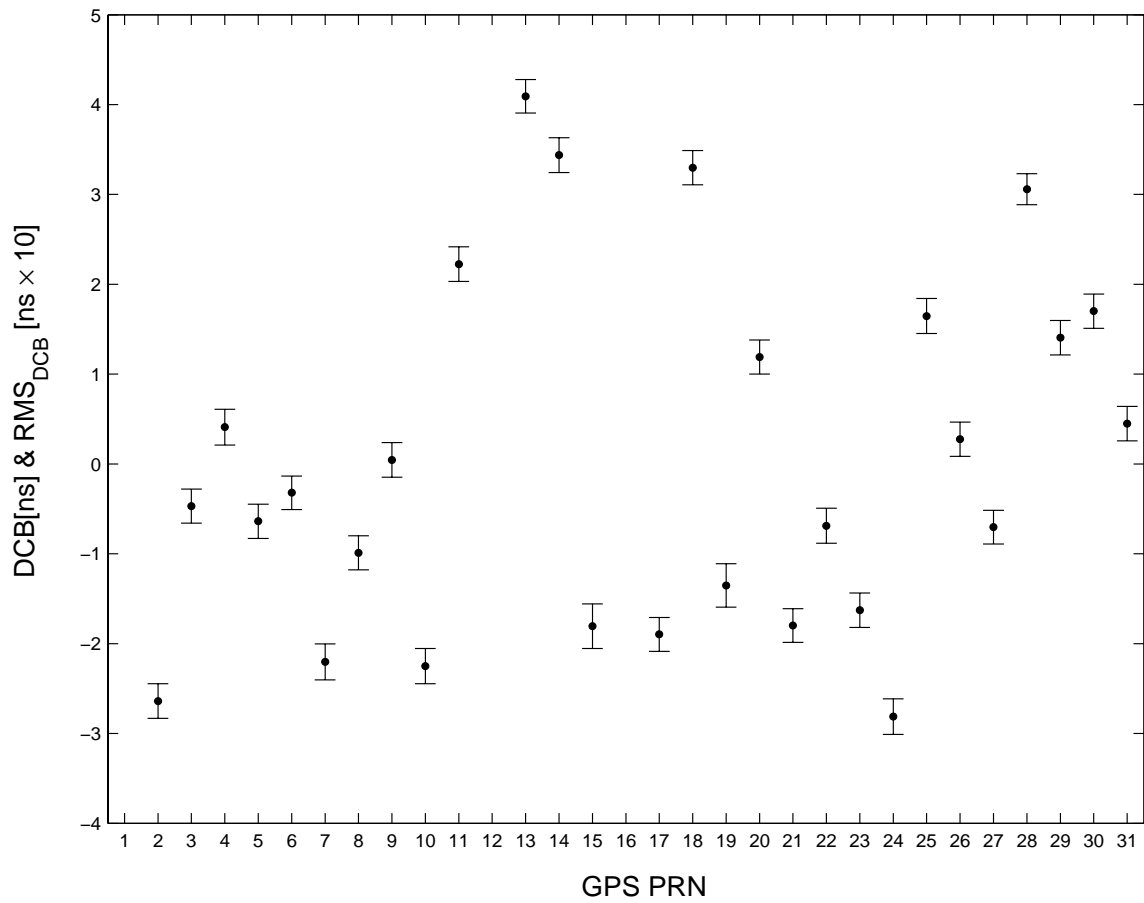
Figure 5.3: Mean DCB[ns] and the corresponding RMS $[ns \times 10]$ values for GPS spacecrafts for March 21 - March 30 2001
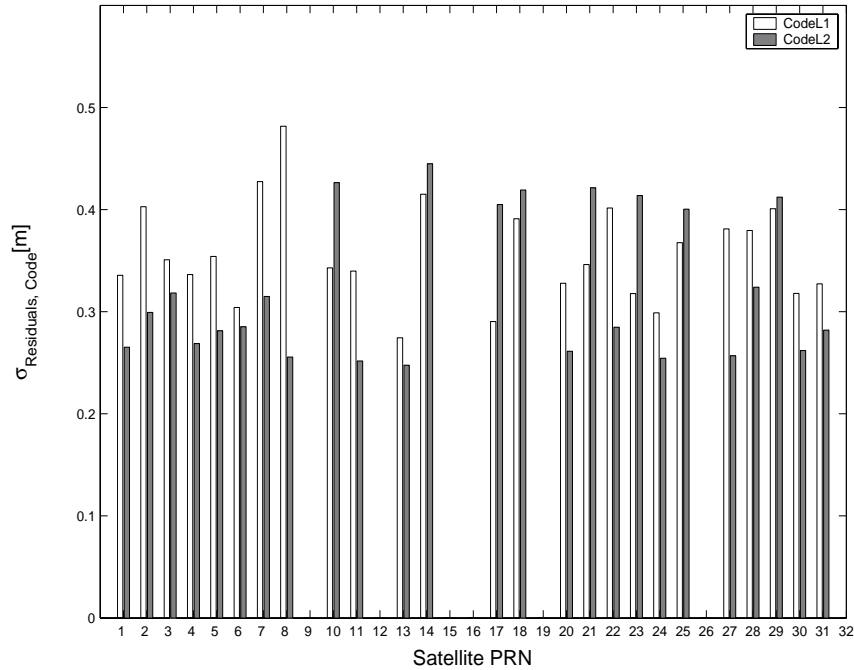
Figure 5.4: Standard deviation for pseudo-range residuals (white bars for L1, grey bars for L2) $\sigma_{Residuals,Code}[\text{m}]$ for station HUXL March 22 10.00-22.00 UTC

observation time spans in a fixed network. Values for receiver DCB range between 2 and 20 nanoseconds [cf. Schaer, 1999].

5.2.3.2 Analysis of computed measurement residuals

Measurement residuals have been analysed for both single point positioning and baseline post-processing. This analysis produces a measure of uncertainty specific to a particular setting, station, environment and temporal period. The computed residuals contain all remaining un-modelled error components (i.e. multipath, ionospheric delay etc.). Figures 5.4 and 5.5 show the post processed residuals for the code and carrier-phase measurements for the station Huxley (HUXL) situated an the roof of Imperial College. The values justify the use of pseudo-range measurements.
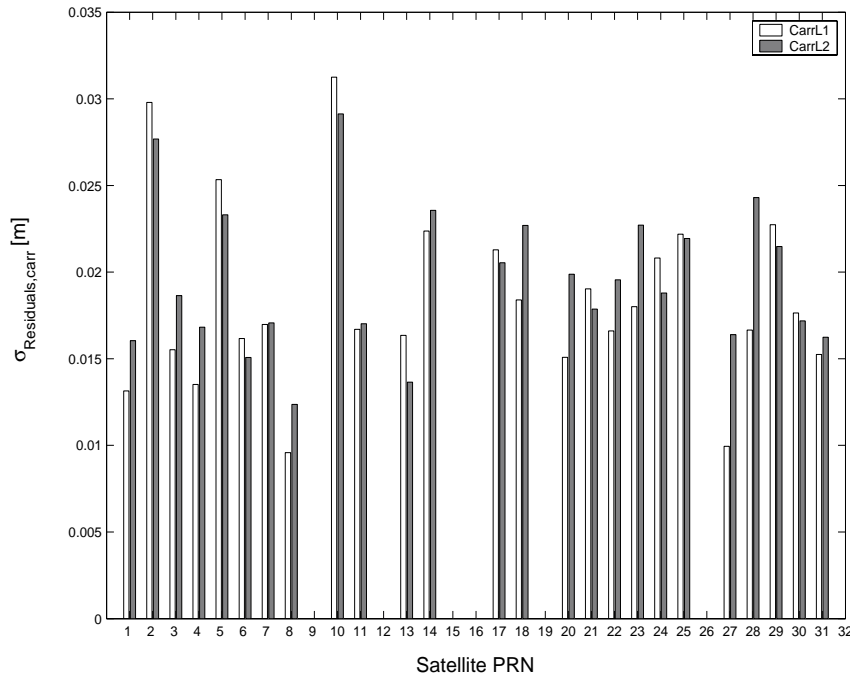
Figure 5.5: Standard deviation for carrier-phase residuals (white bars for L1, grey bars for L2) $\sigma_{Residuals,Carr}$[m] for station HUXL March 22 10.00-22.00 UTC

5.2.4 Derivation of the weighting function

Based on the assumption of a stationary and exponentially correlated process for the standard deviations of each *satellite-receiver* combination [cf. Goad and Yang, 1994], an attempt has been made to derive an exponential weighting function for each type of receiver used in this research.

To support the proposed elevation dependent weighting strategy, standard deviations, estimated by the receiver firmware, of code- and carrier-phase measurements have been logged as supported by the NovAtel $RGEA-log (cf. Appendix A.1). These values reflect the correlation between elevation, *snr* and the corresponding measurement standard deviation. The standard deviation in this case is the result of elevation dependent (i.e. general level of multipath which effects the snr) and elevation independent components (i.e. receiver thermal noise). The time series for each receiver satellite combination results in a receiver specific weighting function as derived in this

section.

The difference compared to the approach described by Euler and Goad [1991] can be seen in the second-order exponential function and the determination of the corresponding polynomial coefficients. Furthermore the coefficients have been derived according to each different observation type.

The general form of the second order exponential expression to describe the *a-priori* standard deviation as a function of elevation has been assumed as follows.

$$\sigma_{Obs,a-priori}(elev) = \exp(p_1 elev^2 + p_2 elev + p_3) \tag{5.13}$$

The coefficients (p_1, p_2, p_3) have been derived using a least-square estimator, minimising the variance between the predicted function and the measured time series.

The results of the regression analysis are based on 15 hours of data captured at the station HUXL (cf. Section 6.1). The coefficients were predicted using all measurement noise values for the corresponding measurement type (code and carrier). Table 5.1 contains the estimated coefficients p_1, p_2, p_3 in Equation 5.13.

Table 5.1: Estimated coefficients for exponential weighting function corresponding to NovAtel Millennium WAAS

	p_1	p_2	p_3
L_1	0.0003	-0.045	-3.930
L_2	0.0003	-0.050	-3.520
P_1	0.0003	-0.050	-1.170
P_2	0.0006	-0.090	-1.025

Figures 5.6 to 5.9 show the time series scatter plots (for a period of 2 hours with a 2 minute interval) of the standard deviation of measurement, versus the satellite elevation, and the corresponding predicted noise using the coefficients in Table 5.1. The standard deviations have been logged for code- and carrier-phase observations for the GPS satellites PRN2, PRN3 and PRN14. The correlation between measurement noise and elevation can be seen clearly. Low satellite elevations are the reason for the wider spread in standard deviation in Figures 5.8 and 5.9. The weighting strat-
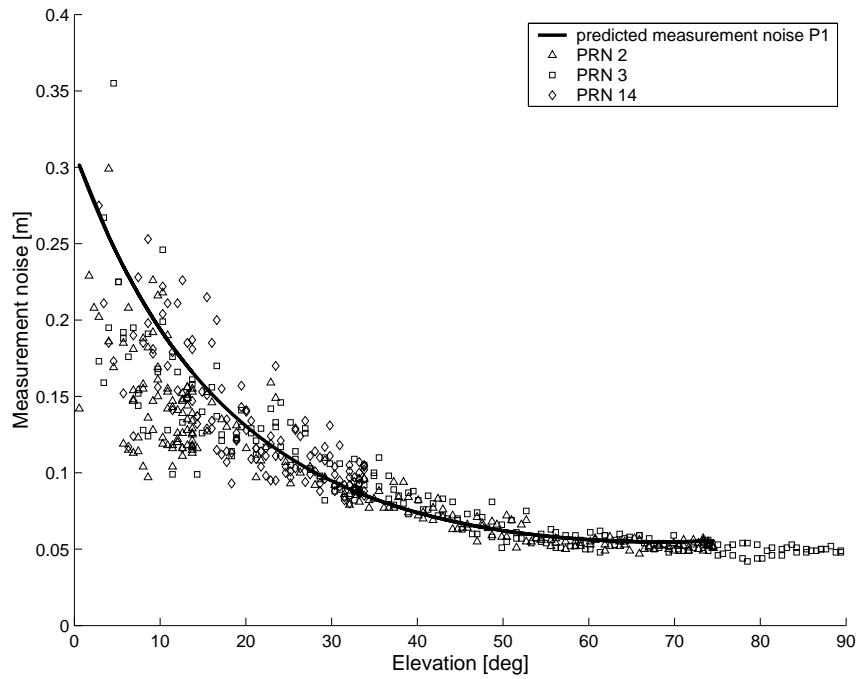
Figure 5.6: Predicted versus measured measurement noise for NovAtel Millennium WAAS on L1 pseudo-range measurements (over 2 hours in 2 minute increments)

egy minimises the effect of elevation depended error components, namely multipath, receiver noise and the DCB.

The measurement standard deviations for the Geostationary Earth Orbiting (GEO) satellites have not been analysed since the data have not been used in the ionospheric estimation. In any case since GEO satellite elevations do not, in general, change over time no elevation dependency of noise values should be observed.
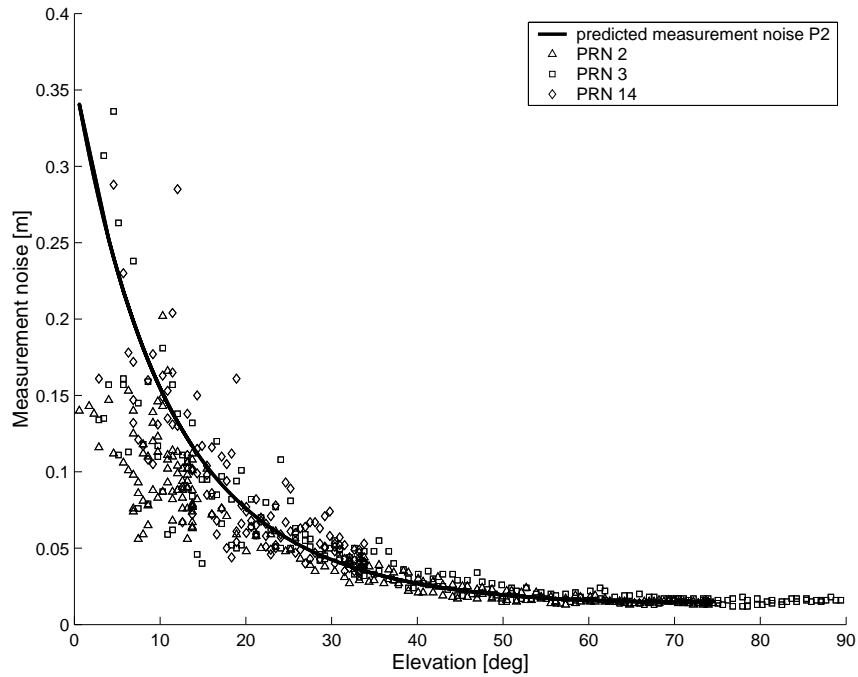
Figure 5.7: Predicted versus measured measurement noise for NovAtel Millennium SBAS on L2 pseudo-range measurements (over 2 hours in 2 minute increments)
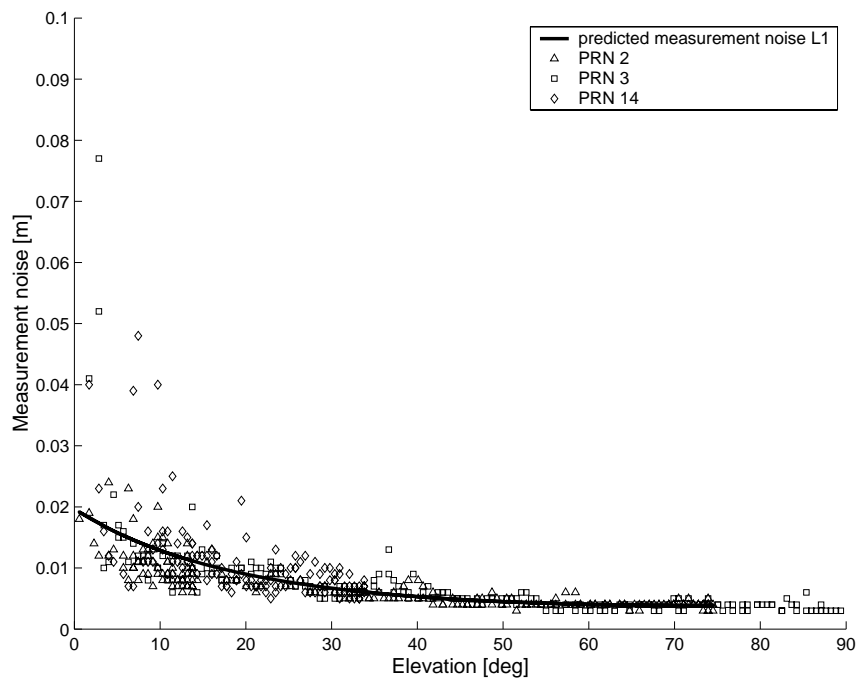
Figure 5.8: Predicted versus measured measurement noise for NovAtel Millennium WAAS on L1 carrier-phase measurements (over 2 hours in 2 minute increments)
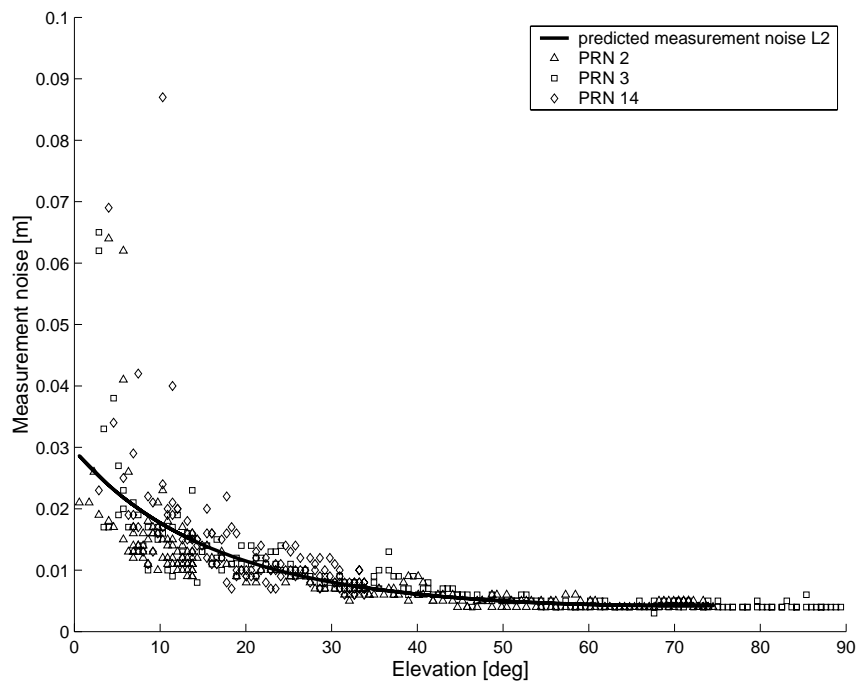
Figure 5.9: Predicted versus measured measurement noise for NovAtel Millennium SBAS on L2 carrier-phase measurements (over 2 hours in 2 minute increments)

5.2.5 Kalman filter formulation to estimate the ionospheric delays

The data analysis for the code and the carrier observations in the previous section shows sufficiently good quality for both types of measurement. This justifies the use of the dual-frequency GPS observations to estimate local (station specific) ionospheric delays and the initial values for the L_1 (N_{L1}) and *wide-lane* (N_{WL}) ambiguities.

The Kalman filter formulation used including the system design matrix, the state vector, the state transition matrix and the corresponding variance-covariance matrices (cf. Equations 5.1 and 5.3) has been defined as follows based on the observation equations as given in 5.8 to 5.12.

System design matrix:

$$A_k = \begin{bmatrix} 1 & 1 & 1 & 0 & 0 \\ 1 & -1 & -1 & \lambda_{L1} & 0 \\ 1 & \xi_{L1,L2} & \xi_{L1,L2} & 0 & 0 \\ 1 & -\xi_{L1,L2} & -\xi_{L1,L2} & 0 & \lambda_{L2} \\ 0 & 1 & 1 & 0 & 0 \end{bmatrix} \tag{5.14}$$

State vector:

$$x_k = \begin{bmatrix} \rho(t) & \frac{I_0(t)}{f_1^2} & \frac{I_\xi(t)}{f_1^2} & N_{L1} & N_{WL} \end{bmatrix} \tag{5.15}$$

State transition matrix:

$$F_k = \begin{bmatrix} 1 & 0 & 0 & 0 & 0 \\ 0 & p_{ion,0} & 0 & 0 & 0 \\ 0 & 0 & p_{ion,\xi} & 0 & 0 \\ 0 & 0 & 0 & 1 & 0 \\ 0 & 0 & 0 & 0 & 1 \end{bmatrix} \tag{5.16}$$

The values $p_{ion,0}$ and $p_{ion,\xi}$ represent the prediction operator for the trend and the signal component of the ionospheric delay respectively. According to Goad and Yang

[1994] their values can be given by as follows.

$$p_{ion,0} = \exp(-\left|\Delta t\right|/\tau_0) \qquad p_{ion,\xi} = \exp(-\left|\Delta t\right|/\tau_\xi) \tag{5.17}$$

Whereas τ denotes the corresponding correlation time and Δt the time between two adjacent measurement epochs.

The remaining diagonal elements of the state transition matrix are set to one, which indicates, that these values do not change for filtered ranges and ambiguities. This is obviously not true. Hence numbers $\to \infty$ are assigned to the corresponding entities in the system variance-covariance matrix. The entities in the system variance-covariance matrix corresponding to the ambiguity terms are usually set to zero, since the ambiguity should remain unchanged (provided no occurrence of cycle-slips, cf. Section 3.7).

System variance-covariance matrix:

$$Q_{\epsilon,k} = \begin{bmatrix} \infty & 0 & 0 & 0 & 0 \\ 0 & \sigma_{ion,0}^2 & 0 & 0 & 0 \\ 0 & 0 & \sigma_{ion,\xi}^2 & 0 & 0 \\ 0 & 0 & 0 & 0 & 0 \\ 0 & 0 & 0 & 0 & 0 \end{bmatrix} \tag{5.18}$$

A-priori observation variance-covariance matrix:

$$Q_{e,k} = \begin{bmatrix} \sigma_{PR(L1)}^2 & 0 & 0 & 0 & 0 \\ 0 & \sigma_{\Phi(L1)}^2 & 0 & 0 & 0 \\ 0 & 0 & \sigma_{PR(L2)}^2 & 0 & 0 \\ 0 & 0 & 0 & \sigma_{\Phi(L2)}^2 & 0 \\ 0 & 0 & 0 & 0 & \sigma_{I(external)}^2 \end{bmatrix} \tag{5.19}$$

The measurement errors are assumed to be uncorrelated. Therefore off-diagonal entries are set to zero. The actual values for the diagonal-elements of the a-priori

variance covariance matrix $Q_{e,k}$ are computed according to Equation 5.13 and the corresponding coefficients in Table 5.1.

Figure 5.10 concludes the main processing steps to derive the ionospheric delay specific to each satellite-receiver combination. The preprocessing step involves the detection and correction of cycles slips and outliers (cf. Section 3.7).
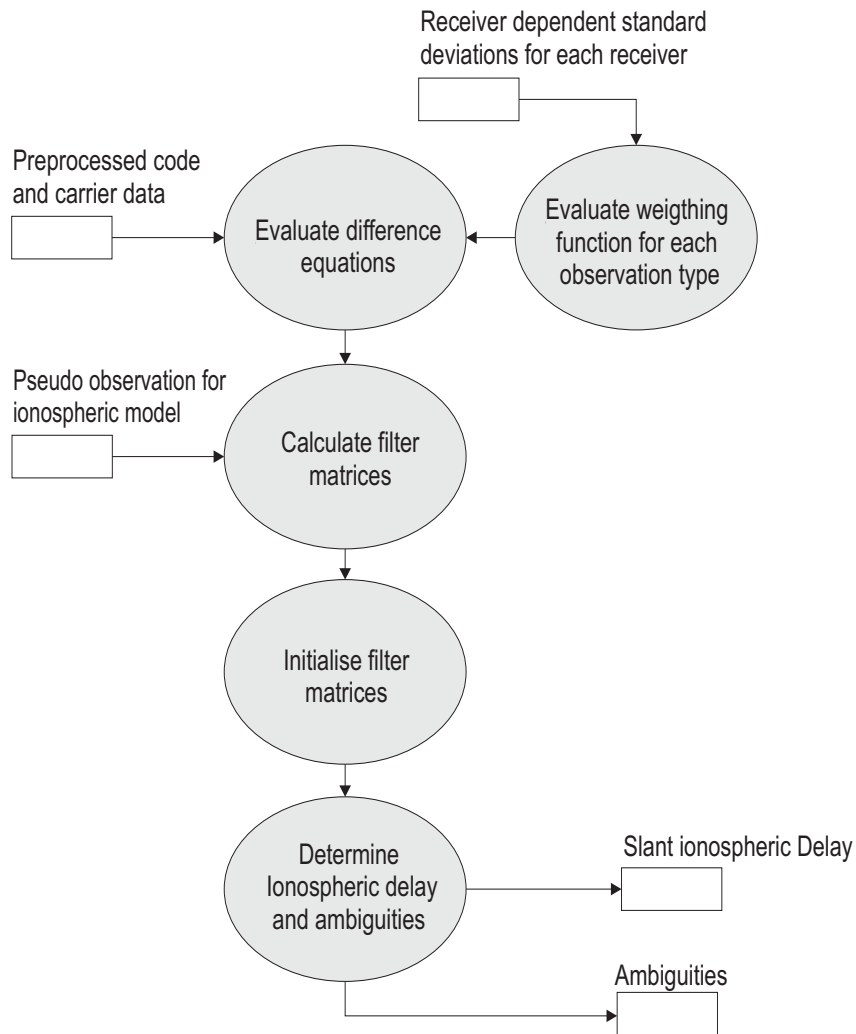
Figure 5.10: High level design of ionosphere analysis module as implemented in this research

5.3   Integrating ionospheric pseudo-observations in the estimation process

The idea of utilising externally derived ionospheric delay information is based on the fact that the available data (assuming the use of only two receivers) is sparsely distributed. This either leads to numerical instabilities in the process of ionospheric delay estimation using Kalman filters or to subsequently wrongly determined station specific ionospheric delay models causing unreliable ambiguity determination and baseline computation.

To aid the ionospheric estimation process, ionospheric delay *pseudo-observations* and the corresponding standard deviations have been introduced to the system of linear equations described in Section 5.2.2.

Originally two sources of externally derived ionospheric models were considered; the model based on CODE (cf. Section 3.4.9) and the EGNOS based model (cf. Section 3.4.10). The EGNOS model is designed to be accessible in near real-time, the CODE model is available with a 24 hour delay after the data is captured. Based on this the EGNOS model would be more suitable for kinematic positioning. However, since its current quality as indicated by the GIVE (cf. Section 3.4.10) is not sufficient the model has not been used here . It is assumed that as soon as EGNOS achieves FOC the quality parameters of the ionospheric models will be suitable to aid the ionospheric delay estimation for high accuracy kinematic positioning.

Instead the more precise CODE model has been used here. This should provide important information and experience on the use of externally derived ionospheric models in the process of determining higher accuracy local ionospheric models for use with EGNOS single frequency data.

A software module has been developed to extract and interpolate slant ionospheric delays from the CODE TEC maps and the corresponding $\sigma_{iono,95\%}$ (converted from $\sigma_{TEC,95\%}$). The actual values and their standard deviations are included in the *Kalman* filter equations (5.14 to 5.19).

The following three steps were implemented to derive the ionospheric pseudo-

observable and its corresponding standard deviation.

5.3.1 Temporal interpolation

The model for a local or a global ionosphere as processed by CODE is represented by a set of TEC-maps in the so called IONEX data format [cf. Schaer et al., 1998]. The temporal sampling rate is 2 hours. Hence twelve TEC-maps have been used to describe the daily ionospheric model. The interpolation at epoch, t, between two consecutive TEC-maps ($TEC_i \leq t < TEC_{i+1}$) at the time T_i and T_{i+1} for a vertex of longitude, λ, and latitude, ϕ, is realised with the following formula as given by Schaer et al. [1998].

$$TEC_{vert}(\phi, \lambda, t) = \frac{T_{i+1} - t}{T_{i+1} - T_i} TEC_i(\phi, \lambda'_i) + \frac{t - T_i}{T -_i T_{i+1}} TEC_i(\phi, \lambda'_{i+1}) \qquad (5.20)$$

In order to compensate for the correlation between the position of the Sun and the ionospheric activity, two consecutive maps TEC_i and TEC_{i+1} have been rotated according to $\lambda'_i = \lambda - T_i$. This can be interpreted as the equivalent to Earth's rotation for the time span between the TEC time stamp and the actual receiver time to be evaluated. The same algorithm is applied for the corresponding values for the a-priori standard deviation, $\sigma_{iono,95\%}$, of the ionospheric delay model.

5.3.2 Spatial interpolation

In order to interpolate between the four surrounding vertices of the ionospheric TEC map the following algorithm based on RTCA-DO-299 [1996] has been adapted and implemented. A weighting function is implemented to account for the distance between the data points and the points to be evaluated. The mathematical formulation for the spatial interpolation of the vertical TEC values, as function of the corresponding ionospheric pierce point (IPP) is below.

$$TEC_{IPP}(\phi_{IPP}, \lambda_{IPP}, t) = \sum_{i=1}^{4} W_i(x_{PP}, y_{pp}) TEC(\phi_i, \lambda_i, \mathrm{t}) \qquad (5.21)$$

Where,

TEC_{IPP} is the TEC value for the pierce point to be evaluated

W is the inverse distance weighting function

TEC is the TEC value at the corresponding grid node

λ, ϕ, t are the geographic longitude, latitude and the time of the corresponding vertex in the TEC map.

The weight function is determined as [RTCA-DO-299, 1996],

$$W(x_{PP}, y_{PP}) = x_{PP}^2 y_{PP}^2 (9 - 6x_{PP} + 6y_{PP} + 4x_{PP}y_{PP}) \qquad (5.22)$$

The orthogonal coordinate differences $\Delta\lambda_{PP}$ and $\Delta\phi_{PP}$ between the geographical pierce point coordinates λ_{PP}, ϕ_{PP} and the lower left grid node (λ_1, ϕ_1) are determined by,

$$\Delta\lambda_{PP} = \lambda_{PP} - \lambda_1 \qquad \Delta\phi_{PP} = \phi_{PP} - \phi_1 \qquad (5.23)$$

The values for x_{PP} and y_{PP} are determined using the spatial resolution of the model in both dimensions (ξ_λ, ξ_ϕ), where:

$$x_{PP} = \frac{\Delta\lambda_{PP}}{\xi_\lambda} \qquad y_{PP} = \frac{\Delta\phi_{PP}}{\xi_\phi} \qquad (5.24)$$

The expressions above describe a continuous surface for all points defined within the corresponding part of the surface. Figure 5.11 depicts the parameters described in Equations 5.21 to 5.24.
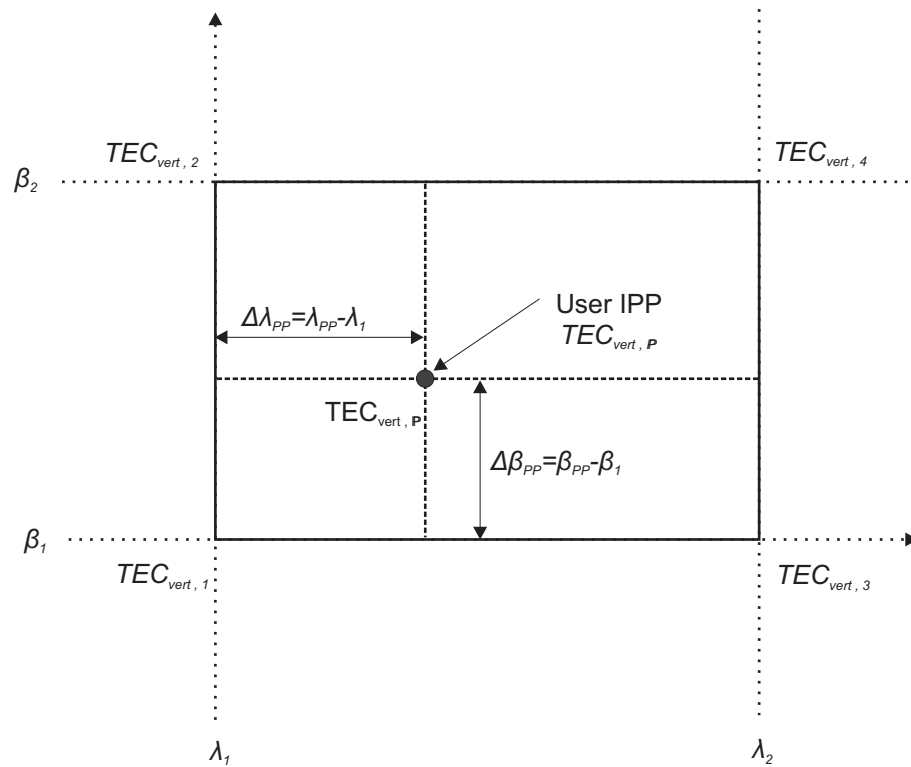
Figure 5.11: Interpolation of user pierce point using the four surrounding grid node values [cf. RTCA-DO-299, 1996]

The location of the pierce points is determined by the application of Equations 5.25 to 5.27. E and A denote the elevation and the azimuth for the direct *line-of-sight* between satellite and receiver respectively. Figure 5.12 illustrates the determination of the ionospheric pierce point based on the applicable parameters. The geographic latitude, ϕ_{PP}, is computed as follows.

$$\phi_{PP} = \sin^{-1}\left(\sin\phi_U \cos\Psi_{PP} + \cos\phi_U \sin\Psi_{PP}\cos A\right) \qquad [rad] \qquad (5.25)$$

According to Figure 5.12 the earth central angle is derived as follow.

$$\Psi_{PP} = \frac{\pi}{2} - E - \sin^{-1}\left(\frac{R_{Earth}}{R_{Earth} - h_{Shell}}\cos E\right) \qquad [rad] \qquad (5.26)$$

Finally, the geographic longitude of the pierce point (λ_{PP}) is given by.

$$\lambda_{PP} = \lambda_U + \sin^{-1}\left(\frac{\sin\Psi_{PP}\sin A}{\cos\phi_{PP}}\right) \qquad [rad] \qquad (5.27)$$
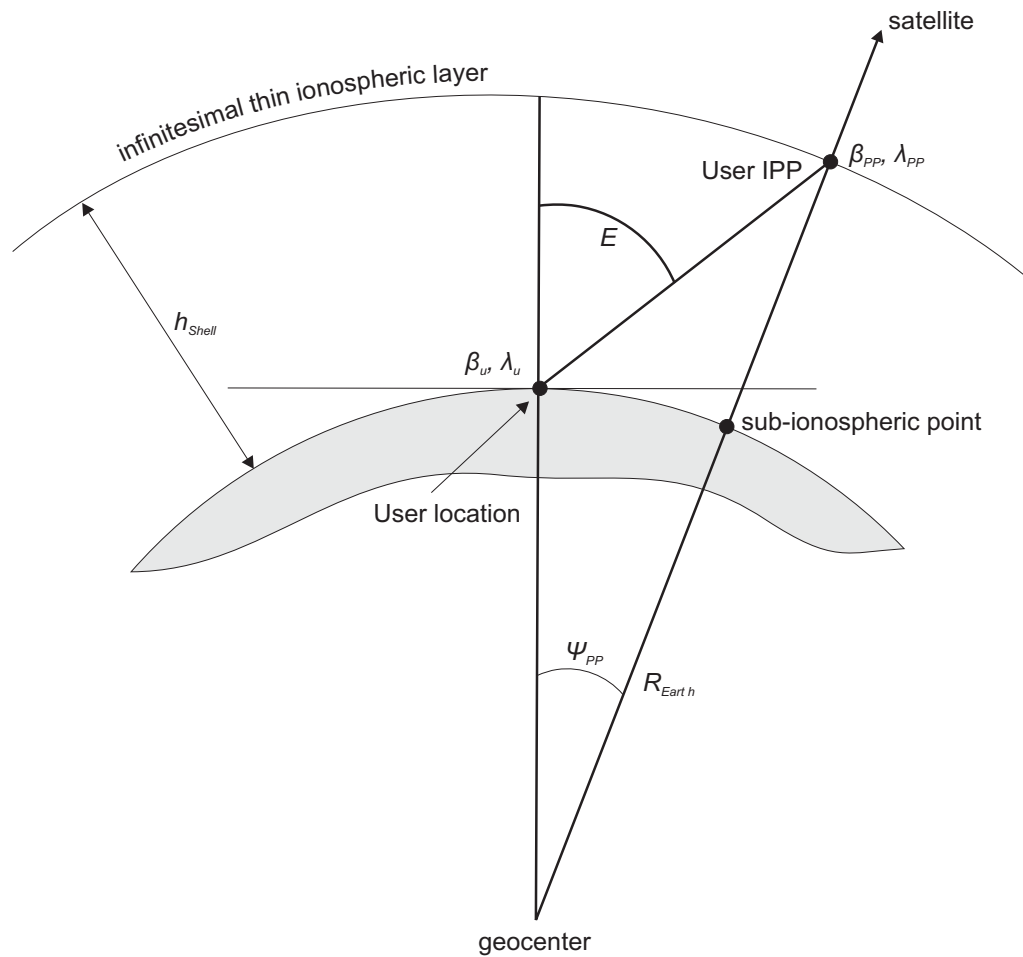
Figure 5.12: Determination of ionospheric pierce point location $(\phi_{PP}, \lambda_{PP})$ based on user location (ϕ_U, λ_U), shell height (h_{Shell}) and elevation (E) [cf. RTCA-DO-299, 1996]

5.4   Parameterising the ionosphere

5.4.1   General remarks on *2-D* parameterisation

Several different algorithms to parameterise a local or global ionospheric activity have been described in Sections 3.4.6.4 to 3.4.6.7. The approaches rely exclusively on either large sets of direct ionospheric observations or dual-frequency GPS observations from networks operating several continuously running stations. Furthermore they cover the whole globe or large regions requiring more sophisticated functions such as Taylor series expansion or spherical harmonics to describe spherically curved surfaces.

In the studied case of kinematic processing based on only two receivers, ionospheric observations are sparsely distributed in the spatial domain (i.e 10-12 observations per station). This puts a constraint on the capability to cover all spatially changing features of a local ionosphere. This is true in particular in times of hight solar activity and ionospheric storms (cf. Section 3.4.2).

In order to make optimal use of all available ionospheric information a two-dimensional (planar) approximation has been adapted for this research. This is justified by the following example of comparing the geometrical dimensions on a sphere versus a planar surface.

The maximum diameter of the area probed by one receiver with a minimum elevation angle (E_{min}) of 15° on a truncated sphere is $\approx 1170 km$. The corresponding diameter in a 2-D system is $\approx 1167 km$. This converts to a maximum distortion in distance by a factor of 1.00566 which is considered negligible with respect to potential impact of local ionospheric activity.

The following sections investigate two different approaches which vary in complexity and ability to fit sparsely distributed data sets.

5.4.2 Examples of 2-D parameterisation methods

5.4.2.1 Linear interpolation

The easiest and computationally most economical method is based on a weighted linear interpolation between the three vertices of the surrounding triangle. The triangles are usually generated by *"Delaunay"* triangulation which involves finding the optimal constellation for triangles connecting the data points. The computational details are given in Watson [1992] and Aurenhammer [1991].

Because the method evaluates a linear function for each triangle separately, it does not describe a continuous surface, i.e. the first and the second derivative of the surface show discontinuities. Hence the method is not a "true" parameterisation of the data set over the whole data space. A general mathematical formulation adopted for determining TEC values using weighted linear interpolation is given below.

$$TEC(\lambda, \phi) = \sum_{i=1}^{3} w_i TEC(\lambda_{PP,i}, \phi_{PP,i}) \tag{5.28}$$

Where w_i denotes the normalised inverse distance between the triangle vertices and the point to be evaluated. It is computed as follows.

$$w_i = \frac{d_i}{\sum_{i=1}^{3} d_i^{-1}} \tag{5.29}$$

.

5.4.2.2 Cubic spline interpolation

Cubic splines are commonly used for the interpolation/parametrisation of sparsely distributed data sets. A 2-dimensional interpolation technique for a sparsely distributed ionospheric data set based on cubic splines has been developed for this research building on the idea by Sandwell [1987].

For the 2-dimensional case, the following spline function returns the interpolated TEC_{node} value using N data-points.

$$TEC_{node} = \sum_{j=1}^{N} TEC_{PP,j} \cdot w_m \left(x_{node} - x_j \right) \tag{5.30}$$

w_m denotes the two-dimensional "*Green's force function*" used to evaluate the specific weight of each data-point and $x_{node} - x_j$ the vector between the data-point and the evaluated node-point and $TEC_{PP,j}$ the corresponding TEC value at the ionospheric pierce point.

$$w_m = \left| (x_{node} - x_j) \right| 2 \left(\ln \left| (x_{node} - x_j) \right| - 1 \right) \tag{5.31}$$

Although rather sparsely placed data points (10 for a region of $12^o \times 20^o$) have been used, the strategy ensures a continuous surface without discontinuities in the first and second derivative. Therefore, the computed model represents a continuous (smooth) parametric model and does not capture abrupt changes in the ionosphere.

Both approaches (Section 5.4.2.1 and 5.4.2.2) were implemented in code and the corresponding results were compared using simulated data. This includes the computation of a local ionospheric model comparing the injected and the recovered TEC values for the corresponding grid nodes.

The histograms in Figure 5.13 illustrate the frequency of computed differences for ≈ 40000 grid nodes between the models based on linear interpolation and nonlinear cubic interpolation. Both models are derived from synthetic data sets allowing the comparison with the true injected value for the ionospheric delay. The models have been scaled to represent the vertical ionospheric delay on L1. The histogram corresponding to the cubic spline algorithm (compared to the linear interpolation algorithm) shows slightly lower differences to the injected original model. Hence, the cubic spline interpolation algorithm has been chosen for the further parametrisation of the local ionospheric model.
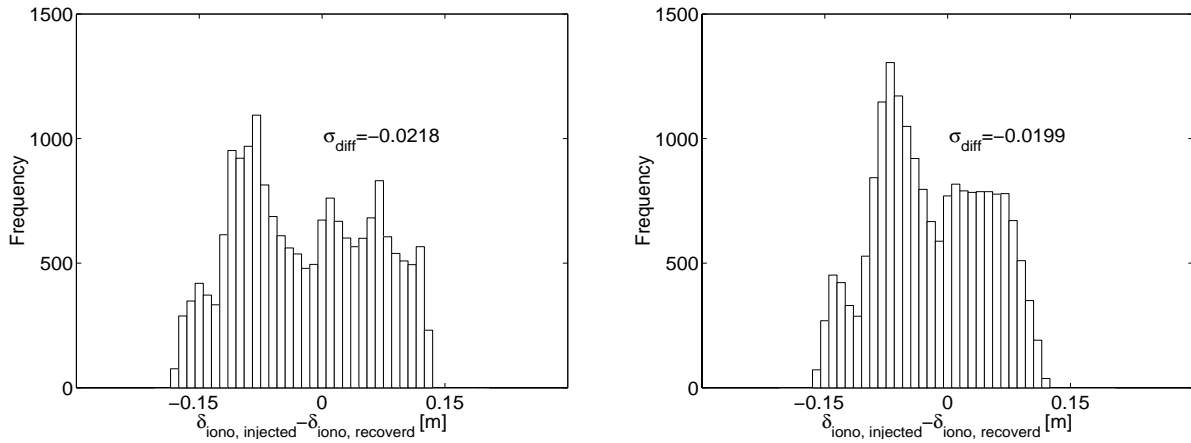
Figure 5.13: Histograms of relative frequency of differences [m] between the injected and the recovered ionospheric model based on linear interpolation (left) and on cubic spline interpolation (right)

5.5 Computation of station specific ionospheric models: Implementation

A software module was developed and implemented based on the 2-D cubic spline function using the dual frequency GPS derived ionospheric delays. Such a model is used either to generate slant delays as applicable for the GEO IPP's or to create a grid based *Station Specific Local Ionospheric Model (SSLIM)*.

Figure 5.14 illustrates the high level design of the parameterisation module as implemented in code. The important input parameters are the satellite and receiver positions as well as the estimated slant ionospheric delays. Furthermore, the parameters for the ionospheric model (shell height) and the spatial resolution are specified. The output includes the slant range corrections applicable to the single frequency observations or the grid based SSLIM. Numerical results and their validation based on other available ionospheric models are discussed in Section 5.6.
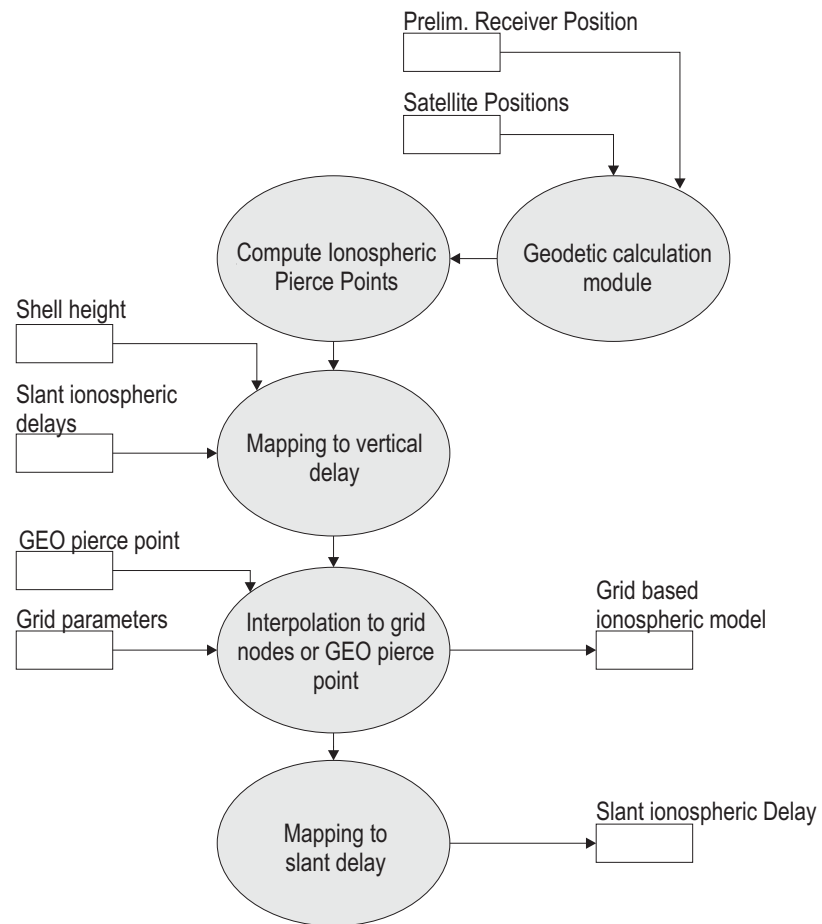
Figure 5.14: High level design of the ionospheric parameterisation module

5.6   Computation and validation of station specific ionospheric models

The following section discusses the validation of the computed ionospheric models based on numerical results. These are computed for all applicable stations based on data captured on 25 March 2002. The data has been derived based on the observation campaign as described in Section 6.1. The models are compared with the corresponding CODE (cf. Section 3.4.9) and *Klobuchar* model (cf. Section 3.4.6.4). The comparison with the CODE model as originally used for computation provides the validation for the model implementation and is a measure of the coverage of local ionospheric features. The *Klobuchar* model is used only for reference since it is the standard correction model for single frequency observations for single point positioning.

Different station specific ionospheric models using the following processing parameters have been computed.

- **Parameter set I:** Computation based only on dual frequency GPS code- and carrier phase observations. No external model has been used. The weighting function proposed in Equation 5.13 has been used to minimise the effect of elevation dependent error components.

- **Parameter set II:** Computation based on dual frequency observations and an externally derived model (i.e. CODE), with no weighting function applied.

- **Parameter set III:** Computation based on dual frequency observations and the externally derived model (i.e. CODE) with the weighting function applied (Equation 5.13).

The validation itself is based on three different levels of data analysis.

- **Validation based on synthetic data:** Providing the validation of model consistency, correct algorithmic and implementation.

146

- **Validation based on real data:** Providing a test of applicability of computed ionospheric delay models based on real data.

- **Analysis of computed baseline components:** This methodology is given in Section 6.3 which involves application of the computed range corrections and the corresponding qualities for the computation of the corresponding baseline components.

The numerical values for the station specific models for all relevant stations has been to compute the differences between each model (with a particular parameter setting) and the CODE model. The CODE model has been used to validate the results because its accuracy is given as approx. 0.1 *TECU*, corresponding to a total vertical range error of 0.016m over all data points [cf. Schaer, 1999].

The TEC values have been computed for all grid nodes within the area defined by the maximum and minimum pierce point coordinates. The particular grid node locations are defined by the grid locations as given in the IONEX file corresponding to the CODE model. The ionospheric models have been computed based on both synthetic and real data. Subsequently the TEC values were converted into the applicable vertical range corrections using the following approximation of Equation 3.30.

$$\delta_{range,iono} \approx \pm \frac{40.3}{f^2} \cdot TEC_{vert} \tag{5.32}$$

Where,

$\delta_{range,iono}$ is the vertical ionospheric range correction

f is the corresponding carrier frequency.

Opposite signs are applied for the correction of code and carrier-phase observations (cf. Section 3.4.4). Based on Equation 5.32, 1 $TECU$ (10^{16} electrons/m^2) corresponds to $\approx 16cm$ on L1 and to $\approx 26cm$ on L2.

5.6.1 Numerical results using synthetic data

The internal consistency and the correct formulation of the ionospheric delay model were tested with simulated (synthetic) data before applying real data (cf. Section 5.6.2). The external robustness depends on how realistic the data simulation is. The details of the algorithms and the implementation in code used to generate synthetic data can be found in Section 6.2

Table 5.2 summarises the results of the model computation using the given parameter sets I-III.

Table 5.2: Summary of statistics comparing results of different parameter sets to compute station specific ionospheric models based on synthetically derived observations. Shown are the mean differences ($\bar{\delta}_{TEC}$) and the standard deviations (σ_{TEC})

Station	Parameter Set I		Parameter Set II		Parameter Set III	
	$\bar{\delta}_{TEC}$ [TECU]	σ_{TEC} [TECU]	$\bar{\delta}_{TEC}$ [TECU]	σ_{TEC} [TECU]	$\bar{\delta}_{TEC}$ [TECU]	σ_{TEC} [TECU]
HERS	0.1	0.1	0.1	0.1	0.1	0.1
LOND	0.2	0.1	0.15	0.1	0.05	0.1
HUXL	-0.2	0.1	-0.5	0.2	-0.1	0.2
DEVI	0.1	0.2	0.25	0.1	0.1	0.1
SILW	-0.3	0.1	-0.25	0.1	-0.05	0.1
HYDE	0.1	0.2	0.1	0.1	0.1	0.1
WATE	-0.2	0.1	0.1	0.1	0.1	0.1
Mean δ	0.0		0.0		0.0	

An interesting feature of the results in Table 5.2 is that the values tend to deviate in the same direction for each point. It can be seen that although the mean value δ over all stations is zero, the majority of single mean values $\bar{\delta}_{TEC}$ are positive. The differences can range between -0.3 TECU to $+0.25$ TECU corresponding to applicable vertical range errors of $-0.05m$ and $+0.04m$ respectively scaled for the L1 frequency. This trend indicates, the error introduced by the computation of a parametric surface (cf. Section 5.4) which tries to fit all available points [cf. Sauer and Ochieng, 2002b]. This is in accordance to the fact that in the case of baselines

shorter than approx. 30 kilometre the ionospheric delay is still correlated and should be removed by the application of double differences. Details hereof can be found in Chapter 6.

5.6.2 Numerical results using real data

Similar to the validation strategy in the previous section three local ionospheric delay models corresponding the parameter sets I, II and III have been computed using real GPS dual frequency data.

The mean of the differences ($\bar{\delta}_{TEC}$) between the computed models and the CODE model, and the corresponding standard deviations (σ_{TEC}) for the seven stations in the network are summarised in Table 5.3. It can be seen that the model determined without CODE data has the highest differences and bias values compared to the CODE model. As expected, the models incorporating the externally derived iono- spheric information (i.e. from the CODE model) show lower levels of the differences and the standard deviations.

The effect of the proposed weighting function to limit the influence of the elevation dependent error components, can be seen clearly in the lowest values for the mean differences and the standard deviations for parameter set III. The corresponding mean differences range between 0.2 TECU and 0.8 TECU. This converts to 0.003 m to 0.13 m difference in the total range delay. The impact of this level of uncertainty on the final ambiguity determination and baseline computation is discussed in the following Section 5.7.

The mean differences and the corresponding standard deviations are significantly higher compared to the values based on synthetically derived data (cf. Section 5.6.1). This can be explained by the stochastic characteristics of the bias and error compo- nents, injected in the data simulation. In such cases the filters, assuming a correct implementation, as described in Section 5.2.5 should be able to recover the injected (included) ionospheric model accurately.

The computed differences reflect the model uncertainty as well as local ionospheric features which are not covered by the CODE model. These distinct local features can be seen in the differences in Figures 5.15, 5.16 and 5.17, as explained below.

Table 5.3: Summary of statistics comparing results of different parameter sets to compute station specific ionospheric models. Shown are the mean difference($\bar{\delta}_{TEC}$) and the standard deviation (σ_{TEC})

Station	Parameter Set I		Parameter Set II		Parameter Set III	
	$\bar{\delta}_{TEC}$ [TECU]	σ_{TEC} [TECU]	$\bar{\delta}_{TEC}$ [TECU]	σ_{TEC} [TECU]	$\bar{\delta}_{TEC}$ [TECU]	σ_{TEC} [TECU]
HERS	0.9	2.8	0.3	1.4	0.2	0.8
LOND	1.2	3.1	0.5	2.9	0.3	1.6
HUXL	-2.3	3.5	0.4	2.0	0.6	0.8
DEVI	0.9	2.7	-0.9	2.4	0.4	0.7
SILW	-10.2	4.9	-0.5	2.1	0.3	1.2
HYDE	6.4	25.3	5.1	3.4	0.8	2.4
WATE	4.3	8.5	0.7	2.9	0.5	0.9
Mean δ	0.2		0.8		0.4	

Figure 5.15 illustrates the final computed station specific ionospheric model as a temporal snapshot for the station HUXL for 25 March 2000 at 07:40:00 [UTC]. For comparison purpose the extracted CODE model and the Klobuchar model for the same spatial bounds and the same time have been plotted in Figures 5.16 and 5.17 respectively. It can be seen that the model derived using parameter set III covers significantly more local ionospheric features (shown by faster varying values in the TEC distribution) compared to the *"plain"* CODE model. The model based on Klobuchar parameters differs significantly from both other models. This phenomenon proves the fact that the Klobuchar model may cover only 50% of the ionospheric delay [cf. Leick, 1995; Seeber, 1993].

The TEC values in Figures 5.15 to 5.17 have been scaled to the vertical ionospheric delay in metres as applicable on L1.
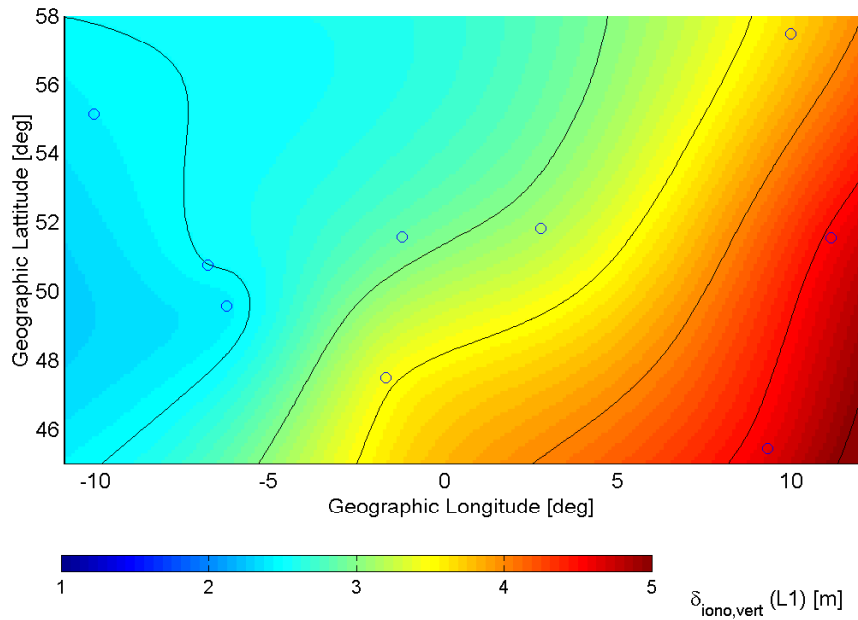
Figure 5.15: Vertical ionospheric delay [m]/final combined SSLIM for station the HUXL 25 March (snapshot at 07:40:00 UTC) scaled for L1
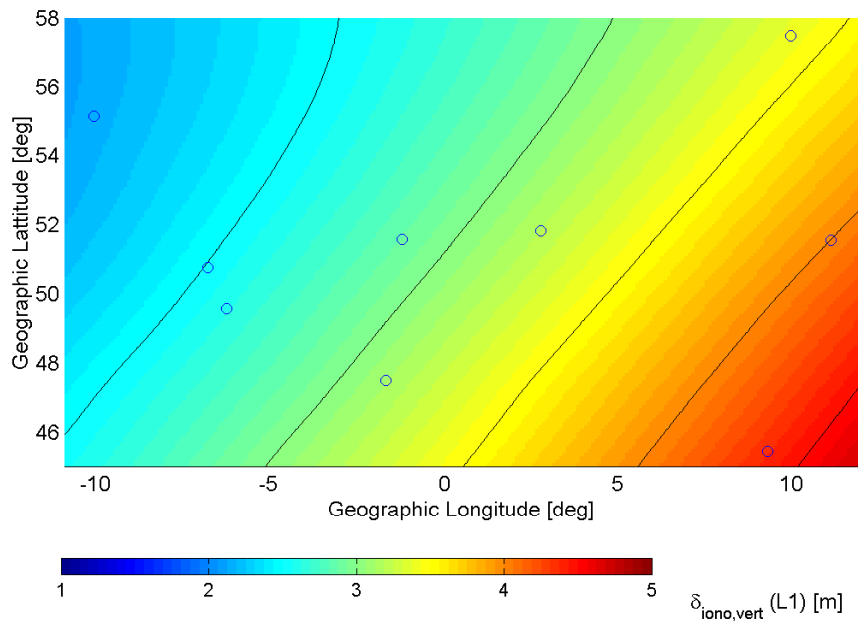
Figure 5.16: Vertical ionospheric delay [m]/derived from the CODE IONEX data for station HYDE 25 March 2000 (snapshot at 07:40:00 UTC) scaled for L1
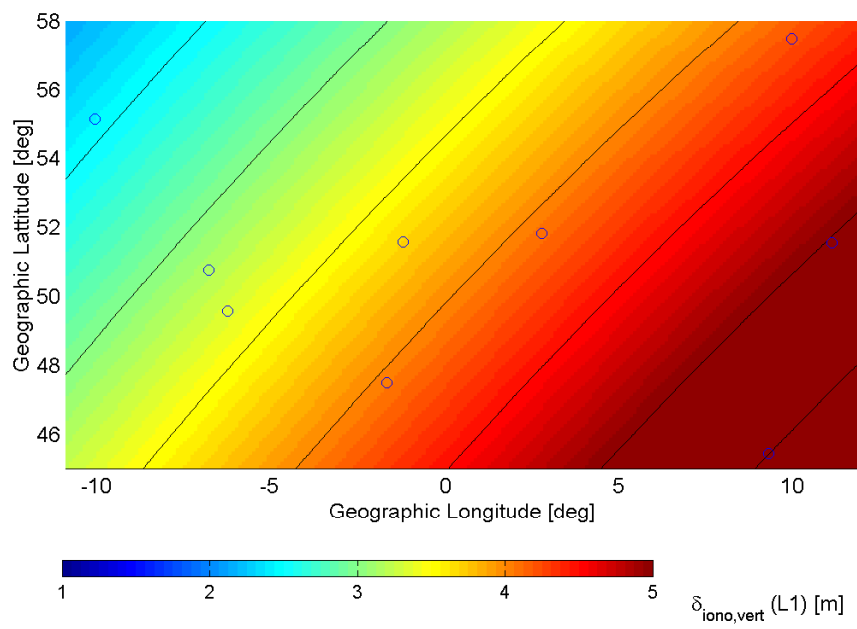
Figure 5.17: Vertical ionospheric delay [m]/derived from the GPS navigation message Klobuchar parameters for the station HYDE 25 March 2000 (snapshot at 07:40:00 UTC) scaled for L1

5.7 The quality of the final ionospheric model and its implications on ambiguity determination

Following the extensive discussion in Section 3.2.3 and 6.1 the following paragraph links the quality of the determined ionospheric slant delay to carrier phase processing and the corresponding ambiguity determination. To resolve the ambiguity term in Equation 3.6 reliably, using a search algorithm, it is necessary to compute the unmodelled error budget with a certain level of accuracy. Hernández-Pajares et al. [2000] specifies half the wavelength ($\lambda/2$) with an uncertainty of no more than $\lambda/4$. The effects of the troposphere and multipath have been discussed in Section 3.5 and 3.6.

In the context of ionospheric refraction, which is frequency dependent, the choice of the linear combination with the corresponding combined wavelength λ is important. This is true in particular because the sensitivity to unmodelled ionospheric errors varies for different linear combinations.

Based on the values given in Table 5.3 and the fact that linear combinations resulting in longer wavelength are less sensitive to uncertainties in the ionospheric modelling, it has been decided to solve for the wide-lane ambiguities (L_5) (Equation 3.12) first before solving for the L1 ambiguities.

The maximum value for the difference between the CODE model and the SSLIM is given with 0.8 TECU equivalent to approximately 0.7 cycles for the L1 and 0.3 cycles for the L_5 frequencies. Upon this fact in the final determination of integer ambiguities and baseline components the SSLIM has been applied for L_5 linear combination. The final impact on ambiguity and baseline computation is discussed in the following Chapter 6.

Chapter 6

Integrated carrierphase processing: Data processing, analysis and validation of results

The first part of this chapter discusses the strategy formulated and executed to capture real data to validate the proposed models.

This is followed by a description of the validation strategy and the mathematical models that have been implemented in code to generated synthetic code and carrier-phase observations, for GPS and EGNOS satellites.

The chapter concludes with the numerical results based on applying the proposed strategy for integrated GPS-EGNOS carrierphase processing. This includes a detailed discussion of the success rates for ambiguity determination and the resulting baseline residuals.

6.1   Test campaign Spring 2001

A data measurement campaign was conducted between 19 March and 25 March 2001 to validate the proposed processing strategy. Two NovAtel Millennium WAAS receivers were used to collect data in the greater London area and Southern England for varying baseline lengths (Table 6.1). The geographical locations and the spatial relationships between the stations are shown in Figure 6.1. The map in the background has been taken from McNally [1997].
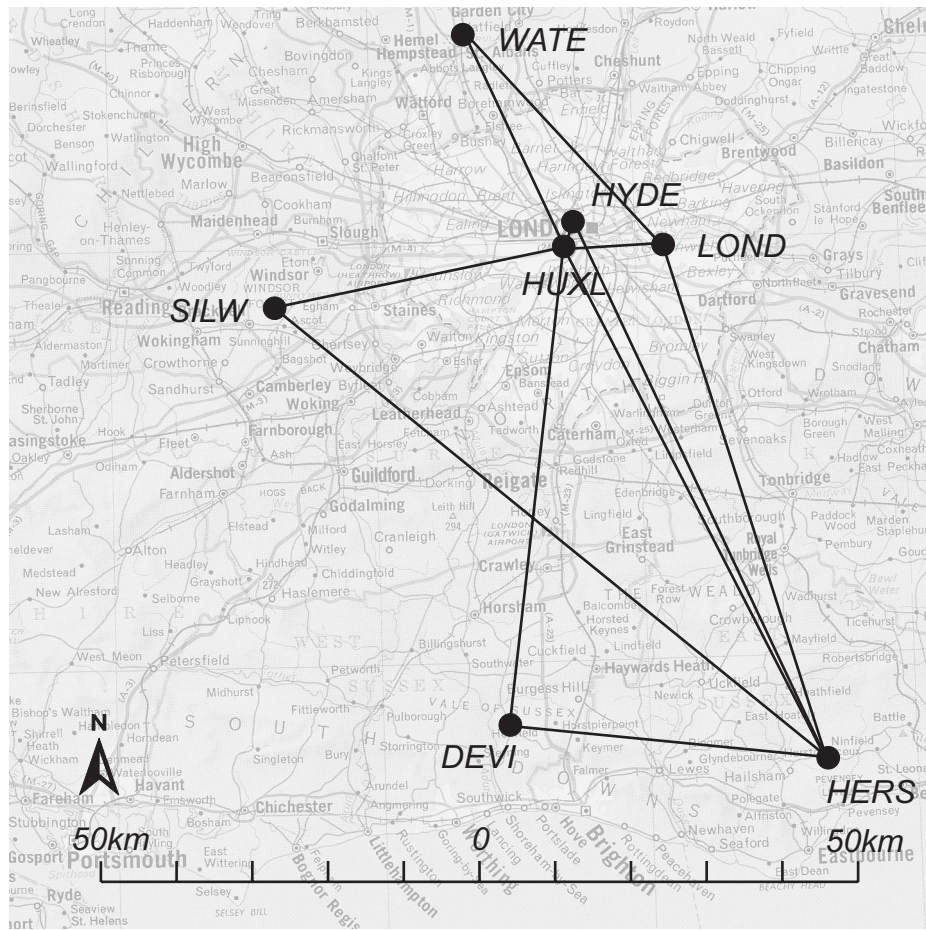
Figure 6.1: Measurement campaign and test network (station ID's and baselines)

Table 6.1: Baselines used for algorithm testing (Locations and station ID's)

Sation ID	Location	Sation ID	Location	Baseline Length [m]
HERS	Herstmonceux	DEVI	Devils Dyke	36660.7111
HERS	Herstmonceux	HUXL	Huxley School	78923.8738
HERS	Herstmonceux	LOND	Greenwich	76203.3141
HERS	Herstmonceux	SILW	Silwood Park	91218.2300
HERS	Herstmonceux	HYDE	Hyde Park	79767.8433
LOND	Greenwich	HUXL	Huxley School	4009.0208
LOND	Greenwich	WATE	Water End	27566.4573
HUXL	Huxley School	DEVI	Devils Dyke	70750.9527
HUXL	Huxley School	HYDE	Hyde Park	1150.7419
HUXL	Huxley School	SILW	Silwood Park	34071.7918
HUXL	Huxley School	WATE	Water End	25643.4879

The stations in Table 6.1 belong to the following regional, national and international GPS networks:

- **Imperial College Network (ICN):** The stations HUXL, HYDE and SILW are permanently marked stations. They have been established for the purpose of this campaign but are envisaged to be used for the Imperial College surveying course in the future.

- **Ordnance Survey (OS) active stations:** These stations are continuously occupied and operated stations within the *UK National GPS Network*. The raw data is available in the public domain in RINEX[cf. Gurtner, 2000] format[1]. The applicable station for the campaign is LOND. It operates an ASHTECH UZ-12 receiver.

- **Ordnance Survey (OS) passive stations:** These are permanently marked stations but unlike the active stations are not operated continuously. They were occupied during the measurement campaign and the data used to ensure the repeatability of the experiments. The stations used were DEVI and WATE.

---

[1]http://www.gps.gov.uk

- **International GPS Service (IGS):** These stations are maintained in the framework of IGS for various high precision GPS applications. The station HERS has been used in the campaign. It operates an ASHTECH Z-XII3 receiver, with data available in the RINEX format in the public domain[2].

6.1.1 Determination of "true" station coordinates and baseline vectors

All available data sets (the stations were occupied for one hour or longer) have been processed in a static post-processing mode using the Leica SkiPro package. The satellite positions have been computed using precise ephemerides. The static processing mode ensured that integer ambiguities could be resolved for all baselines, having detected and resolved all cycle slips. The cycle slip free data was subsequently used for ionospheric modelling and carrier-phase processing (Section 6.3).

Once all baselines (some observed more than once) had been processed using the SkiPro package, a weighted constrained network adjustment was carried out. The OS and IGS stations LOND and HERS were *"fixed"* but allowed a degree of freedom by assigning them weights according to their corresponding standard deviations. The *"fixing"* of the two stations is possible because the OS and the IGS coordinates are determined to a high level of accuracy and precision.

This strategy for network adjustment is justified by the following two assumptions.

- **Repeatability:** Assuming that one of the most important applications of the proposed strategy and algorithms is deformation monitoring of civil engineering structures, the results of each of the stations within the measurement campaign should be repeatable. This is ensured by integrating the network into a spatially large reference frame.

- **Station coordinate and observation quality:** It is assumed that the station coordinates as used in the IGS framework and the OS network are determined

---

[2]http://igs.ifag.de

to a very high level of quality. The receiver and antenna technologies used for these stations reflect the *state-of-the-art* in GPS technology ensuring low levels of measurement noise. Furthermore, the station location is chosen to ensure full view of the sky and low multipath levels.

The derived station coordinates and corresponding baseline vectors formed the reference baseline for the validation of the proposed processing strategy, the resulting position and baseline computations.

6.2   Mathematical models for realistic data simulation

Validation using simulated data was considered vital in testing the implementation, sensitivity and internal consistency of the proposed algorithms. A simulation software package was developed to generate realistic code and carrier observations for a combined GPS-EGNOS constellation. The navigation system errors were generated using realistic error models as described below.

- **Satellite clock error:**   The satellite clock error was generated by interpolating the clock parameters as contained in the corresponding ephemeris file. Furthermore white Gaussian noise (cf. Equation 6.2) was added to simulate stochastic behaviour (the interpolated values have been used as the *seed*, μ).

- **Receiver clock error:** The receiver clock error δt_{rec} is generated using the following quadratic expression:

$$\delta t_{rec} = a_1 + a_2 \delta t + a_3 \delta t^2 \tag{6.1}$$

Whereas the coefficients a_1, a_1 and a_3 are generated randomly using the seed values $a_1 = 10^{-5}[s]$, $a_2 = 10^{-10}[1/s]$ and $a_3 = 10^{-18}[1/s^2]$. This approach ensures that the receiver clock errors range between $\pm 10^{-6}s$ [cf. Strang and Borre, 1998].

- **Measurement noise:** The measurement noise was generated using the elevation dependent model suggested in Section 5.2.4. In addition a noise component was added according to Equation 6.2.

- **Ionospheric refraction:** The ionospheric refraction was generated using a purely deterministic approach (i.e. there is no noise component as described in 5.2.2). TEC values from the corresponding IONEX file were extracted, interpolated and scaled using the mapping function (cf. Equation 3.35) and carrier frequency (cf. Section 3.4.9).

- **Tropospheric refraction:** The tropospheric refraction was computed using the *Saastamoinen* model described in Section 3.5 and using standard atmospheric parameters. Furthermore, a tropospheric scaling is introduced to that simulated and corrected (as in the later processing) are not equal.

- **Multipath:** The multipath error was computed using a *"simple"* elevation dependent model according to Hoffmann-Wellenhof et al. [1997]. A stochastic component was added using white gaussian noise (Equation 6.2).

The following expression has been used throughout the data simulation to compute white Gaussian noise.

$$\varepsilon(x) = \frac{1}{\sigma\sqrt{2\pi}} e^{-\frac{(x-\mu)^2}{2\sigma^2}} \tag{6.2}$$

Where

x	is the randomly generated abscissa with a *"seed"* μ (i.e. the geometrical derived value) and a standard deviation σ (i.e. specified as parameter)
ε	is the noise value to be computed

The satellite orbital (positional) data is generated using the combined orbit files described in Section 3.3.6. Smooth orbit parameters can be used to generate the data as described in Section 4.1, making it possible to generate data for any satellite constellation. Furthermore, observations based on three different carrier frequencies can be simulated to generate GPS III or Galileo observations. The software has multi-station data generation capability and can operate both in static and kinematic modes. A detailed record of all the simulation settings and the error components applied are kept in separate files for subsequent analysis. The derived measurements are stored in the RINEX 2.10 format.

A high level design of the software module is given in Figure 6.2.
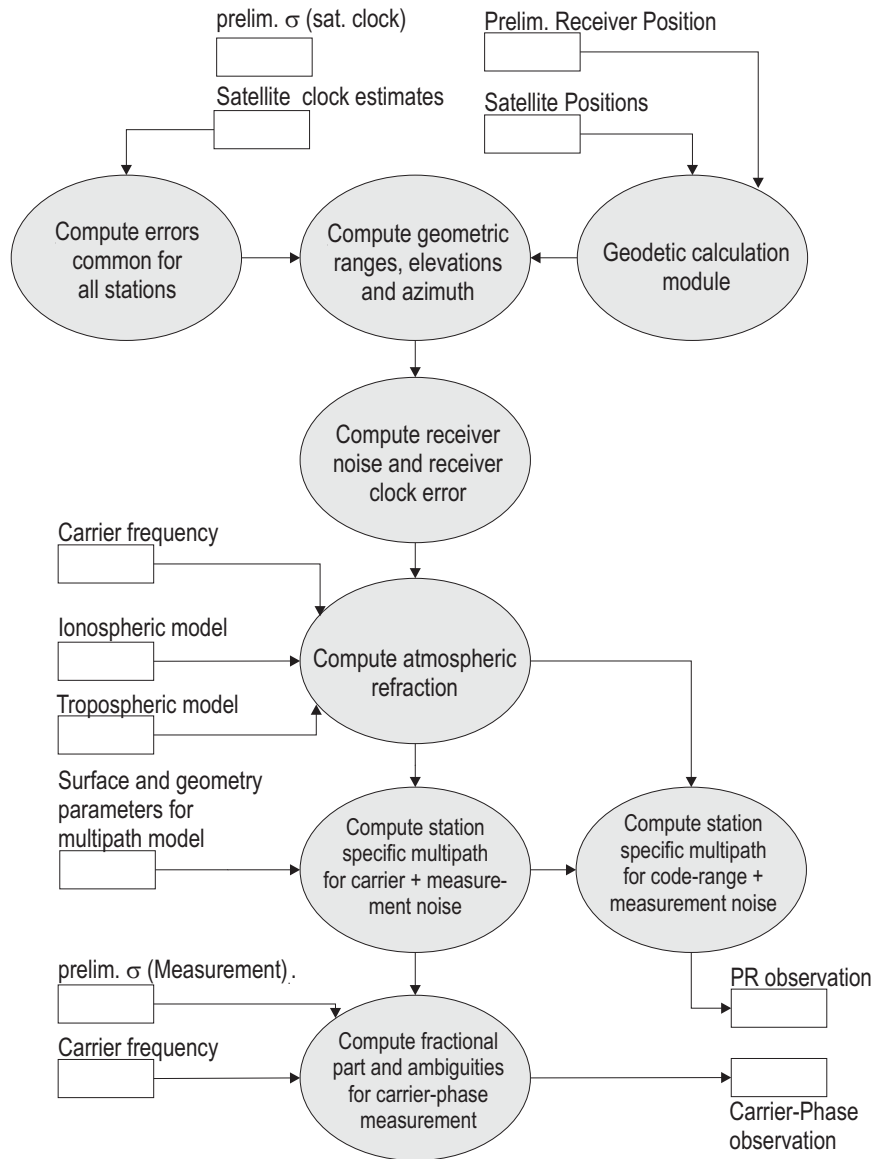
Figure 6.2: High level design of the data simulation software module

6.3 Integrated carrier phase processing

6.3.1 Strategy for stepwise ambiguity determination

A stepwise approach was chosen to solve for the final double-differenced carrier phase ambiguities. This involves firstly solving for the wide-lane ambiguities followed by the L1 ambiguities. In both cases the proposed local ionospheric model (SSLIM) could be used to reduce the influence of the decorrelated ionosphere depending on the length of the baseline .

The flowchart in Figure 6.3 illustrates the approach implemented. The input data comprises the raw observations, the multipath estimates (cf. Section 3.6) and the slant ionospheric delays scaled for the L1 frequency.
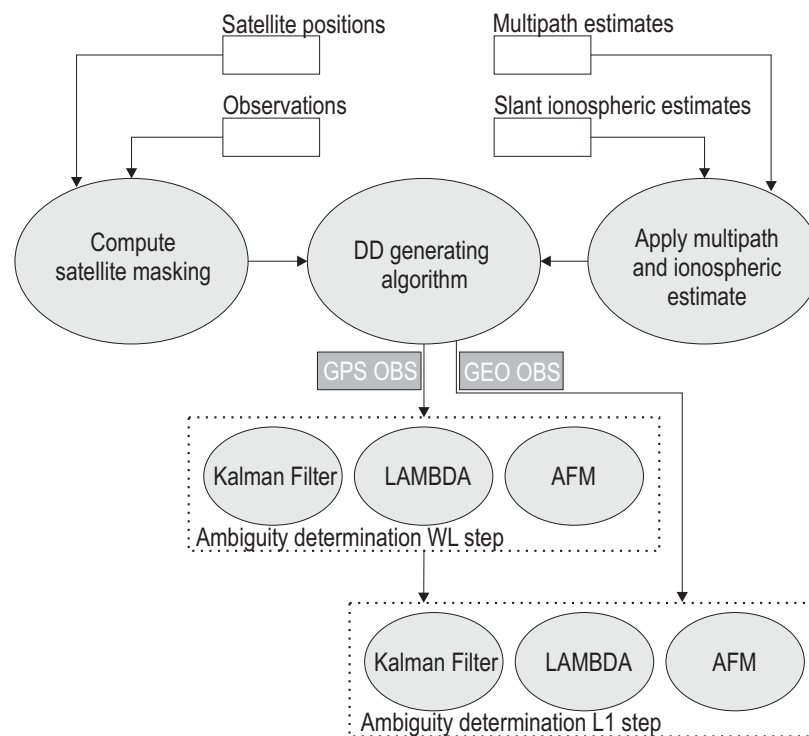
Figure 6.3: High level design of the module for ambiguity determination with optional core algorithm for ambiguity determination

6.3.2 Validation strategy

Various scenarios were formulated to validate and test the algorithms developed. The scenarios were based on different ionospheric options and approaches for ambiguity determination (cf. Section 3.2.3). The focus was on analysing the ability to recover the GEO L1 ambiguities and the impact of the additional observations from the GEO satellites.

Two sources of data have been used, the observations taken from the local network described in Section 6.1 and the raw data simulated as described in Section 6.2. Both data sources (simulated and real) have been used in the computation process to recover carrier-phase ambiguities and finally the baseline vectors.

6.3.2.1 Validation measures

Three measures were used to evaluate the quality of the ambiguity determination and the baseline computation. These values were computed based on the *"truth"* as described in Section 6.1.

- **Fractional part of computed float ambiguity:** The correct integer ambiguity has been computed in the postprocessing step using the Leica SKI-Pro software, the comparison with computed float ambiguity using the new algorithm can be used to measure how close the actual algorithm recovers the original integer ambiguity value. This measure is used in particular for algorithms determining the float ambiguities and subsequently rounding or bootstrapping to the nearest integer value.

- **Success rate of ambiguity determination:** For float ambiguities the value (success rate) is computed by comparing the number of all ambiguities to be determined and the number of ambiguities determined within the range of ± 0.4 fractional parts of the original or true ambiguity. For fixed ambiguities the calculation is given by the ratio between correctly and falsely determined integer

values.

- **Residuals to** *"true"* **baseline vector:** This involves the computation of vector residuals between the computed baseline components and the *"true"* baseline components as determined in a static mode using Leica SKI-Pro. This measure has been used for the final validation in Section 6.4.

6.3.2.2 Validation scenarios

The following scenarios (I-IV) have been set up to validate the proposed processing approach [Sauer and Ochieng, 2002a].

- **Scenario I:** Determination of ambiguities and baseline components involving all Satellites in view (elevation cut-off 15°), without the application of an ionospheric delay model.

- **Scenario II:** Artificial masking is introduced for satellites towards the North West between 10 and 120 degrees, thereby blocking almost 50% of GPS satellites in view as it would be expected in urban and difficult engineering environments.

- **Scenario III:** Extension of Scenario II including one additional GEO satellite. No ionospheric model is applied.

- **Scenario IV:** Extension of Scenario II including one additional GEO satellite, with ionospheric model applied to the GEO satellite data.

- **Scenario V:** Extension of II including one additional GEO satellite, with the ionospheric model applied to all remaining satellites. This is to evaluate the benefit of the computed ionospheric model in case of longer baseline lengths assuming that the ionospheric delay is de-correlated leading to an increased ionospheric residual.

The following Sections 6.3.3 to 6.3.5 document the results computed for the different scenarios and employing the different approaches for ambiguity determination. The

baseline vectors have been computed on an *epoch-by-epoch* basis for all scenarios emulating a kinematic environment. The detailed results presented are for the stations occupied by the NovAtel WAAS receivers simultaneously. Two baselines are considered, the shortest (HUXL $\Rightarrow$ HYDE) with a vector length of about one kilometre, and the longest (HUXL $\Rightarrow$ DEVI) about 70 kilometres long. The results as based for the other baselines are summarised in Section 6.4.

6.3.3   Kalman filtering

The Kalman filter approach was used to determine the float ambiguities and the vector components. Figures 6.4 to 6.6 show the results for the ambiguity determination for the baseline HUXL $\Rightarrow$ HYDE, in form of differences in cycles between the original/correct ambiguity set and the computed ambiguity set. This effectively represents the differences in fractional parts of the real valued ambiguities. Since baseline vector components are directly estimated in the filter state, the geometry, i.e the number and distribution of satellite observations, plays a significant role in determining the final ambiguities and their quality. The implementation allows the wide-lane ambiguities to be calculated in the first instance followed by the L1 ambiguities, using precisely determined double-differenced ionospheric delays.

The best results, i.e. smallest difference in the fractional parts and the highest success rates as expected are achieved with Scenario I, as it reflects the strongest geometrical constellation. The impact of the GEO satellite used is less significant. In some cases the additional GEO satellite impacts negatively on the results. The main reason here is that the improvement in geometry is outweighed by the additional elevation dependent errors introduced by the relatively low elevation of the GEO satellites ($16/22^o$). In the two cases where all satellites and GPS satellites only are used, the success rate for correct ambiguity determination is 100%.

In the scenarios where almost 50% of the GPS satellites are blocked, the geometrical factor plays an important role. In these cases the GEO satellite appears to enhance the quality of the solution .

The impact of the application of the computed ionospheric delay model on the baseline HUXL $\Rightarrow$ HYDE (length $\approx$ 1 kilometre) is, as expected, relatively small. This is true in particular because the ionospheric activity at the rover and reference stations are highly correlated. The level of the DD-ionospheric delays has a magnitude of less than one cm with a noise like characteristic.

Figure 6.4: Baseline HUXL$\Rightarrow$HYDE, Normalised frequency versus fractional part of estimated final L1 ambiguities according to Scenario I(left) and II(right) based on the Kalman filter estimation

Figure 6.5: Baseline HUXL$\Rightarrow$HYDE, Normalised frequency versus fractional part of estimated final L1 ambiguities according to Scenario III(left) and IV(right) based on the Kalman filter estimation

Figures 6.7 to 6.8 show the results for the baseline HUXL $\Rightarrow$ DEVI, the longest baseline occupied by NovAtel WAAS receivers. It can be seen that the error components show lower levels of correlation compared to the shorter baseline. The quality of the baseline computation has dropped significantly.

Figure 6.6: Baseline HUXL⇒HYDE, Normalised frequency versus fractional part of estimated final L1 ambiguities according to Scenario V based on the Kalman filter estimation (left) and success rates [%](right)

Again the geometry of the constellation has the strongest influence on the baseline quality. The impact of the additional observations from the GEO satellite can be seen clearly (cf. Figure 6.8a).

Since the ionospheric component decorrelates significantly at a baseline length of about 70 kilometres, the impact of a correctly determined ionospheric model is now seen to be significant. Figure 6.8(right) and Figure 6.9(left) show the difference between the results based on computation with and without the SSIM. The final success rates for the five scenarios are summarised in Figure 6.9(right). None achieves a 100% success rate. The application of the SSLIM results in a 5% increase in the success rates for the ambiguity dtermination.

6.3.4   Ambiguity Function Method (AFM)

The second method implemented for final baseline/ambiguity determination is based on the Ambiguity Function Method (AFM) described briefly in Section 3.2.3. The implementation allows the determination of baseline components based on a search in the position space using various types of linear combinations of observations on L1 and L2.

This enables a stepwise solution for wide-lane ambiguities in the first instance
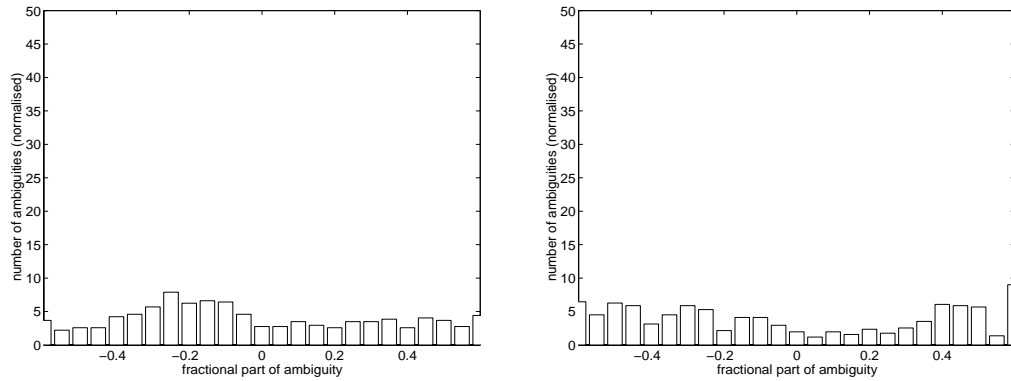
Figure 6.7: Baseline HUXL⇒DEVI, Normalised frequency versus fractional part of estimated final L1 ambiguities according to Scenario I(left) and II(right) based on the Kalman filter estimation
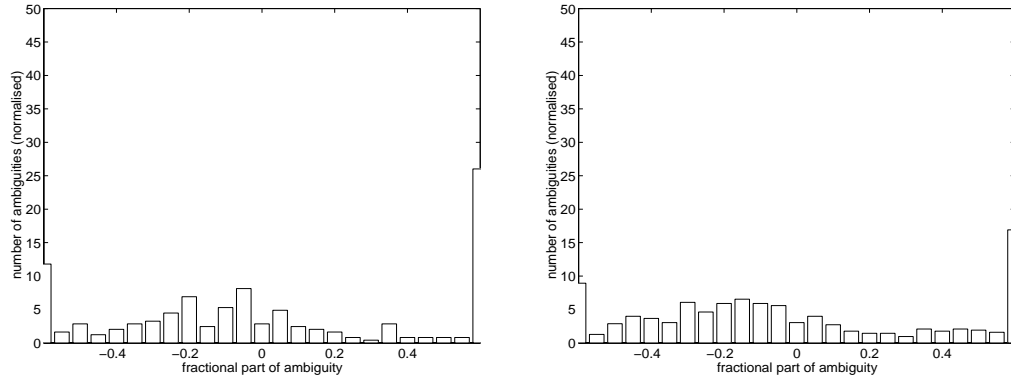
Figure 6.8: Baseline HUXL⇒DEVI, Normalised frequency versus fractional part of estimated final L1 ambiguities according to Scenario III(left) and IV(right) based on the Kalman filter estimation

followed by a subsequent determination of the less noisy L1 ambiguities.

The results based on this method show a slight improvement over those determined by Kalman filtering. A significant influence of the quality of preliminary vector components can be seen. This is logical because the search in the position domain is realised in a defined rather than in an infinite space. The implementation enables the utilisation of preliminary determined baseline components as either results of the previous method (cf. Section 6.3.3) or the utilisation of pseudo-ranges and a least-squares estimator.

The method computes the AFM value using all available satellite observations for
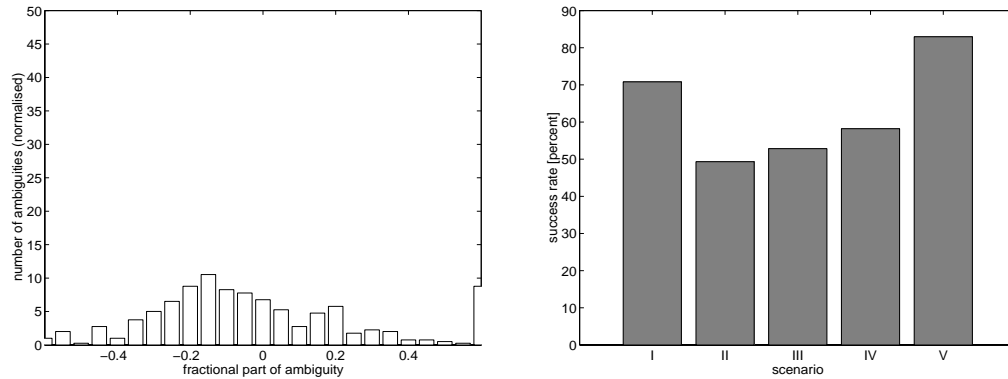
Figure 6.9: Baseline HUXL⇒DEVI, Normalised frequency versus fractional part of estimated final L1 ambiguities according to Scenario V based on Kalman filter estimation (left) and success rates [%] (right)

each test position in the search space. Subsequently for the two test positions with the highest AFM value (regarded as the "*physically*" most likely ones), an F-test is carried out on the computed residuals and the "*statistically*" most likely position is selected.

Inevitably a wrongly determined preliminary rover position would lead to wrong final baseline components and ambiguities. This is true because running the search with a wrongly determined search space would lead to a local maximum of the ambiguity function rather than a global maximum.

Ambiguities and baseline components are determined on an epoch-by-epoch basis. Statistical properties from the previous solution influence the new solution only in form of the position of the initial search space. This makes the AFM the only "*true*" single-epoch method. Furthermore, the method is completely resistant to cycle slips. However, discarding statistical properties imposes disadvantages related to error components with temporal stochastic behaviour.

Similar to the fractional parts as illustrated in Figures 6.4 to Figure 6.9 in Section 6.3.3 the same measures have been calculated for each scenario.

In Figures 6.10 to 6.12 it can be seen that the general level of quality in baseline and ambiguity determination has improved compared to results based on Kalman filtering.
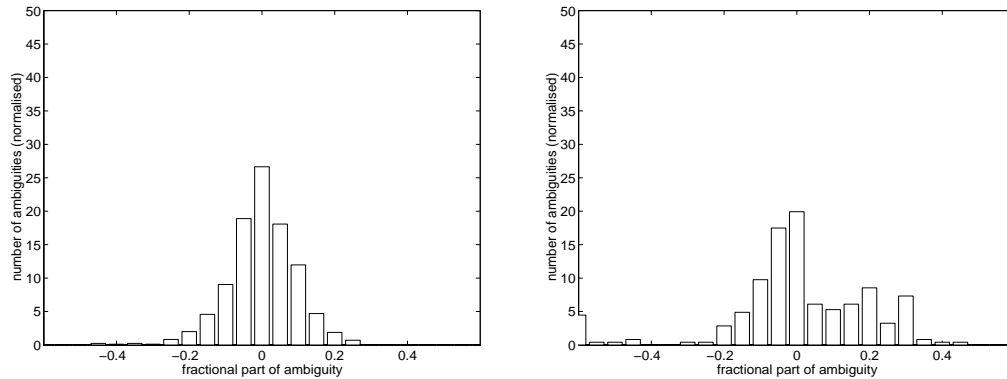
Figure 6.10: Baseline HUXL⇒HYDE, Normalised frequency versus fractional part of the estimated final L1 ambiguities according to Scenario I(left) and II(right) based on the AFM
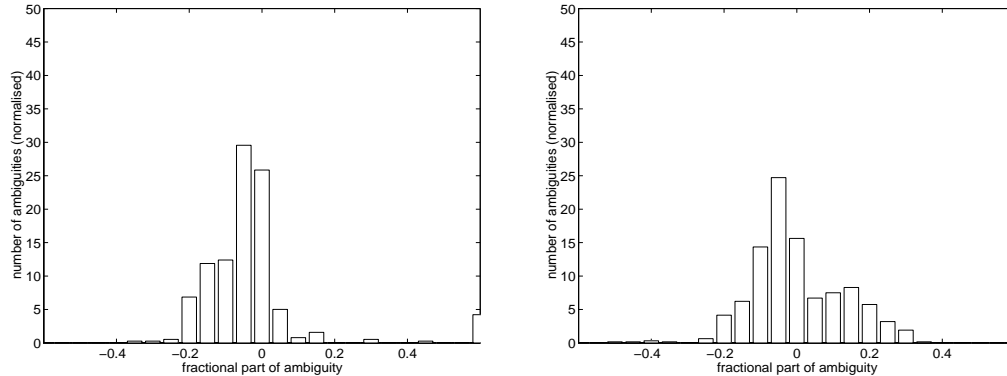
Figure 6.11: Baseline HUXL⇒HYDE, Normalised frequency versus fractional part of the estimated final L1 ambiguities according to Scenario III(left) and IV(right) based on the AFM

A reason for this is the fact that the initial position of the search space position has been determined using the results of the previous section as recommended by Corbett and Cross [1995].

Since the search is carried out in the position domain, the geometry of the constellation has a considerable impact on the success rate of ambiguity determination. Using this method the impact of the additional GEO observation is considerable. The difference can be seen comparing Figure 6.10(right) and Figure 6.11(left), as well as by examination of the success rates for ambiguity determination in Figure 6.12(right).

As with the Kalman filtering, the results for the short baseline HUXL ⇒ HYDE,
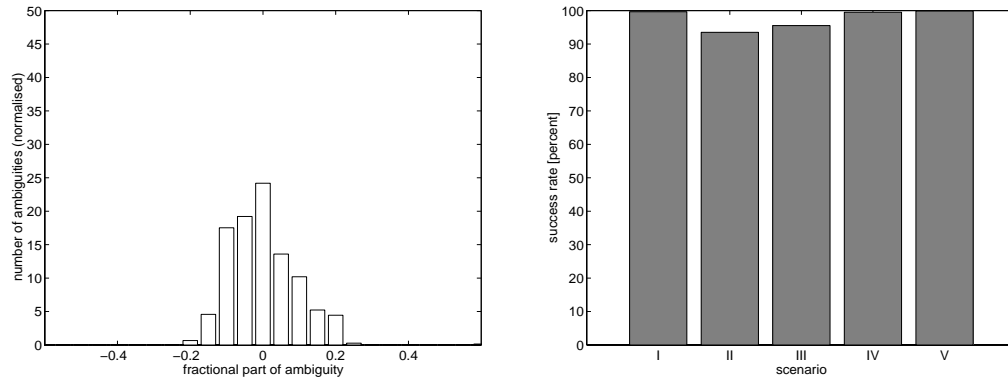
Figure 6.12: Baseline HUXL⇒HYDE, Normalised frequency versus fractional part of the estimated final L1 ambiguities according to Scenario V based on the AFM (left) and success rates [%] (right)

show only a slight improvement as result of the application of the SSLIM. The results for the longest baseline, shows a significant positive impact of the SSLIM. Therefore, the computed ionospheric model is more useful as the ionosphere decorrelates with increasing baseline length.

Furthermore comparing the results based on the AFM with the results based on the Kalman filter implementation for the longest baseline reveals that the search algorithm (based on AFM) is superior in terms of the remaining fractional parts and success rate.
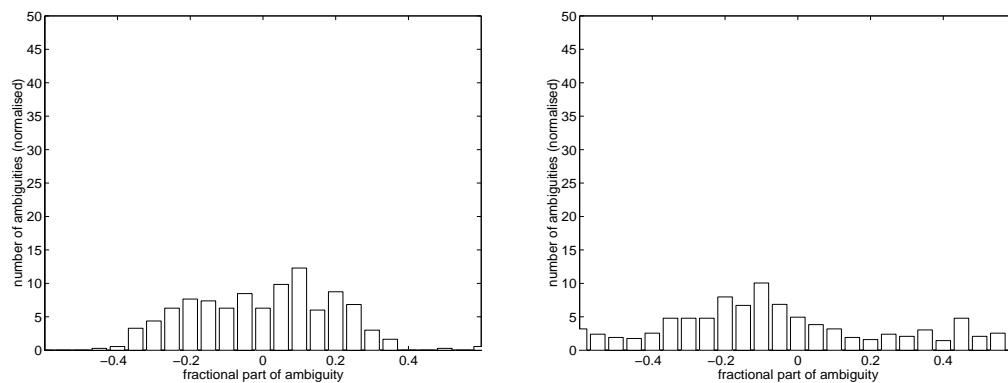
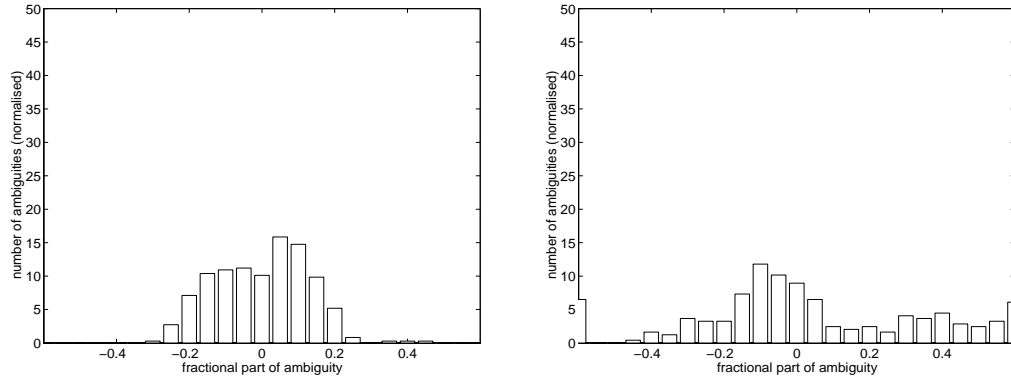**Figure 6.13:** Baseline HUXL⇒DEVI, Normalised frequency versus fractional part of estimated final L1 ambiguities according to Scenario I(left) and II(right) based on AFM
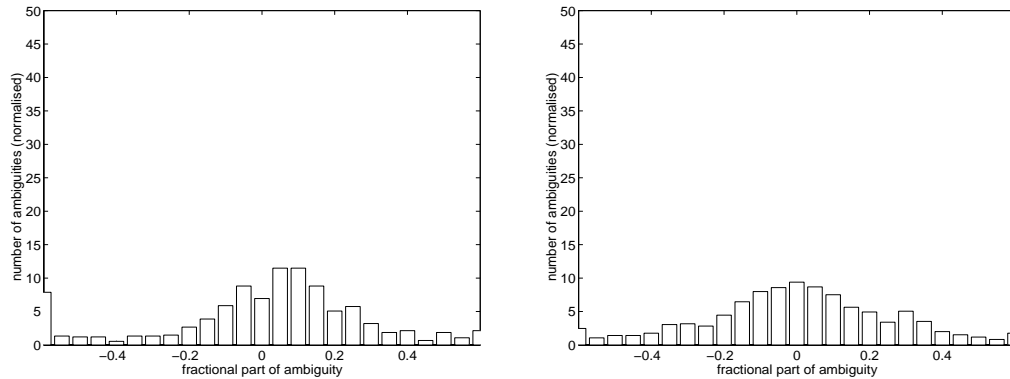
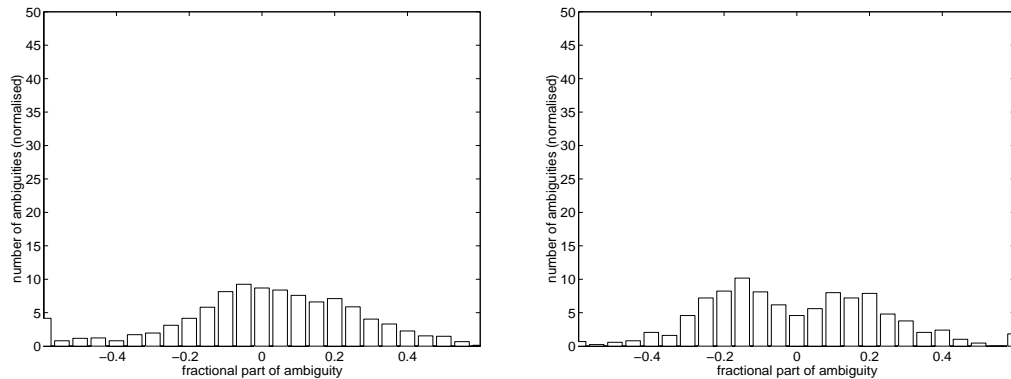**Figure 6.14:** Baseline HUXL⇒DEVI, Normalised frequency versus fractional part of estimated final L1 ambiguities according to Scenario III(left) and IV(right) based on AFM
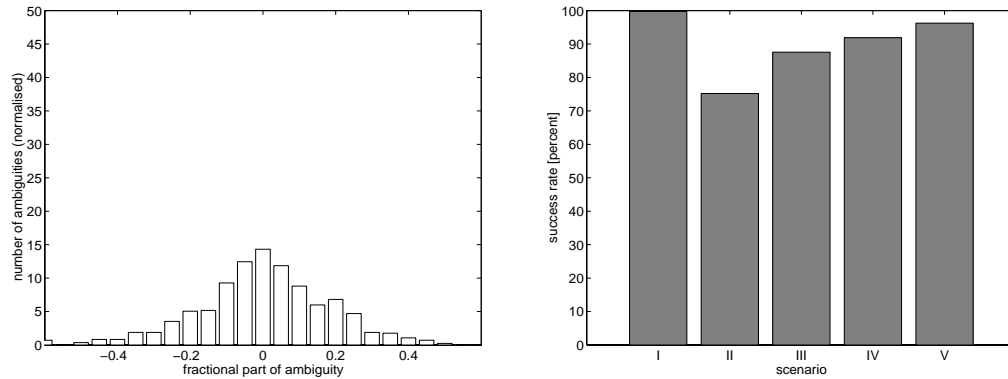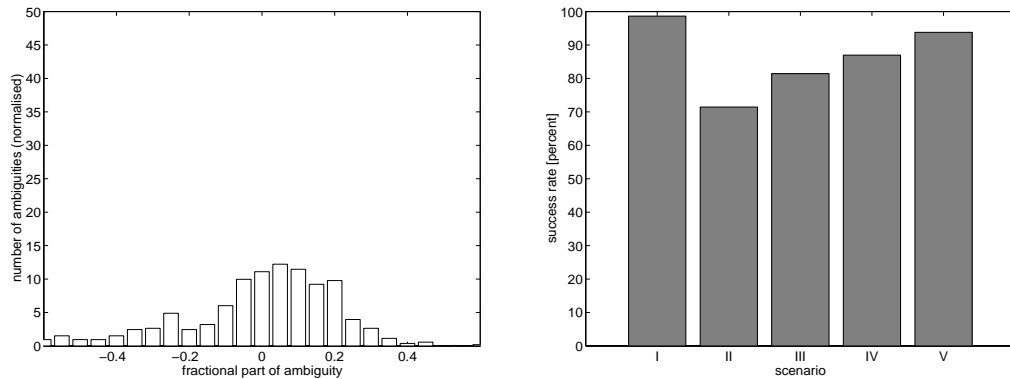

Figure 6.15: Baseline HUXL⇒DEVI, Normalised frequency versus fractional part of estimated final L1 ambiguities according to Scenario V based on AFM (left) and success rates [%] (right)

6.3.5 Least Square AMbiguity Decorrelation Adjustment (LAMBDA)

The last method implemented is the Least Square AMbiguity Decorrelation Adjustment (LAMBDA)[3]. The implementation cumulates the contribution of each epoch of observations until a cycle slip flag is set in the pre-processed observation file.

Subsequently the module for integer ambiguity determination is called and the

---

[3]The core software routines of the LAMBDA method are available in the public domain (*http://www.geo.tudelft.nl/mgp/lambda/software.html*). The routines originally coded in Fortan77 have been rewritten into standard ANSI C language

corresponding steps briefly described in Section 3.2.3, performed. For details on implementation aspects, the reader is referred to de Jonge and Tiberius [1994] and Strang and Borre [1998].

The method searches in a transformed integer valued ambiguity space. Subsequently the final output consists of backward transformed integer valued ambiguities. Again to minimise the impact of ionospheric refraction the method performs a stepwise approach solving for the wide-lane ambiguities (if applicable) first and then in a second step for the more precise L1 ambiguities.

The quality measure applicable to this method is the calculation of the success rate of the ambiguity determination. The value directly reflects the ratio between correct and wrong computed integer ambiguities.

Looking at the way the search space for this method is computed, the link with the geometry of the constellation is obvious. In a first step the computation is based on the variance covariance matrix Q_{XX} of an initial carrier-float solution. Hence a strong geometrical constellation will lead to a more precise determined search space and subsequently to higher success rates.

Similar effects may be observed based on residual errors (i.e. ionospheric refraction and multipath). Hence the success rates for the scenarios employing the ionospheric model are expected to be higher too.

Figure 6.16(left) and 6.16(right) show the success rates for the baselines HUXL⇒HYDE and HUXL⇒DEVI respectively for the Scenarios I-V.

It can be seen that the performance of the LAMBDA method and in particular for the longer baseline is superior to the performance of the methods described in Section 6.3.3 and 6.3.4. The reason can be seen in the utilisation of adjacent epochs (until occurrence of a cycle slip) to solve for the integer ambiguities.

Even for Scenario II where about 50% of the GPS satellites have been blocked the method recovers 95% of the original ambiguities. For the longer baseline (HUXL⇒DEVI) the utilisation of the GEO observation and the ionospheric model recovers almost 95%

of the original L1 ambiguities.
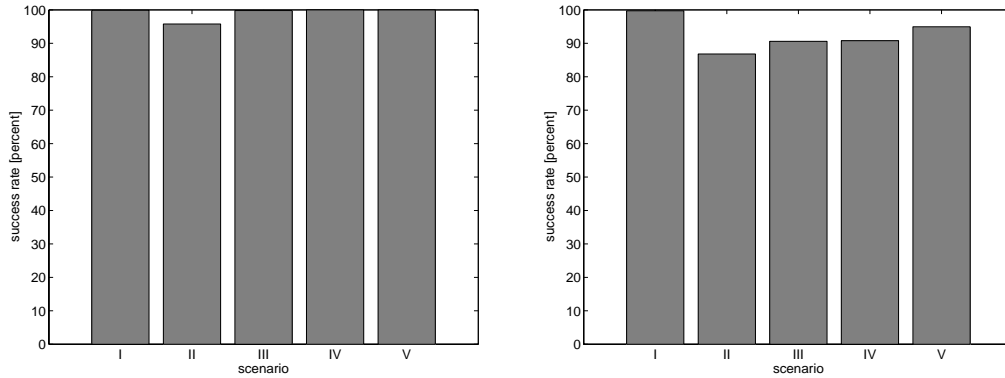
Figure 6.16: Success rates [%] for LAMBDA implementation for baseline
HUXL⇒HYDE (left side) HUXL⇒DEVI (right side)

6.3.6 Concluding remarks on results for ambiguity determination

The results presented in Sections 6.3.3 to 6.3.5 show the impact of additional GEO
observations for ambiguity determination using three different approaches. Further-
more, the benefits of the station specific local ionospheric model (SSLIM) have been
presented. Various quality measures have been used to assess the performance of
three ambiguity determination methods.

The results show, that the LAMBDA method is superior to the Kalman filter and
the AFM, provided that the cycle slips have been detected and repaired successfully.
This is particularly true for longer baselines and short observation time spans. In
such cases the unknown parameters to be estimated are highly correlated.

Based on these results the final baseline vectors have been computed using the
LAMBDA method utilising the station specific local ionospheric models (SSLIM).
The results are discussed in Section 6.4.

6.4 Integrated kinematic positioning for short and medium lengths baselines - final results

The main aim of this research was to evaluate the beneficial impact of additional GEO code and carrier-phase observations, particularly in harsh engineering environments. These environments have been simulated by the introduction of artificial masking, blocking satellites in a controlled way.

It has been shown that the additional GEO observations are more effective when GPS satellites are blocked than in the open sky. It has been shown also that the benefit of the station specific local ionospheric models (SSLIM) developed increases with baseline length. A comparative assessment of three ambiguity determination techniques has shown the superiority of the LAMBDA approach, provided that the problem of cycle slip is dealt with.

This section summarises the results for all the baselines (short, medium and long) used within the test network.

Table 6.2 is a compilation of final standard deviations [cm] of the residual vector components (σ_{North}, σ_{East}, σ_{Height}) for the baselines computed using all GPS satellites in view and for the Scenarios I to V.

The results clearly show the correlation between the number of satellites used, baseline length, ionospheric residual error and the remaining residuals of the computed baseline components.

For baselines shorter than 30 kilometre the double-differencing approach removes the effect of the ionospheric delay to a high extent due the correlation of this error source between reference and rover. In these cases the utilisation of the computed ionospheric model for all satellites (Scenario V) may introduce an additional error source due the uncertainties in the previously computed ionospheric model. The corresponding values of $\sigma_{height} = 2.3cm$ for Scenario IV and of $\sigma_{height} = 3.5cm$ for Scenario V show the significant difference.

175

In the case that the GEO observations are used in conjunction with all available GPS satellites, the relatively low GEO satellites introduce another source of uncertainty.

Table 6.2: Compilation of final standard deviations [cm] of the residual vector components (σ_{North}, σ_{East}, σ_{Height}) for processed baselines based on computation using all GPS satellites in view and on Scenarios I-V

		HUXL⇒HYDE ($\approx 1.1km$) [cm]	**HUXL⇒WATE** ($\approx 25.6km$) [cm]	**HUXL⇒DEVI** ($\approx 70.7km$) [cm]
GPS only	σ_{North}	0.3	0.4	1.2
	σ_{East}	0.3	0.5	1.1
	σ_{Hight}	0.9	1.1	2.4
Scenario I	σ_{North}	0.4	0.7	1.3
	σ_{East}	0.4	0.9	1.3
	σ_{Hight}	1.0	1.8	2.6
Scenario II	σ_{North}	1.5	2.4	3.9
	σ_{East}	2.1	3.5	7.6
	σ_{Hight}	3.9	6.8	10.2
Scenario III	σ_{North}	1.1	1.7	3.0
	σ_{East}	1.5	1.9	4.5
	σ_{Hight}	3.6	4.3	6.3
Scenario IV	σ_{North}	1.0	1.6	2.7
	σ_{East}	1.1	1.8	4.4
	σ_{Hight}	2.3	4.0	6.0
Scenario V	σ_{North}	1.0	1.9	2.2
	σ_{East}	1.2	2.1	4.3
	σ_{Hight}	3.5	4.5	5.8

For the short baseline HUXL⇒HYDE, Figure 6.17 shows the time series of the computed baseline residuals [cm] for the vector components, δ_{North}, δ_{East}, δ_{Height}. 2475 1Hz epochs have been processed. The different time series correspond to Scenarios I, II and IV.

The effects of un-modelled ionospheric errors and the constellation geometry can be seen in the uncertainty in the quality of baseline computation. The corresponding values δ_{North}, δ_{East}, δ_{Height}, for the longest computed baseline HUXL⇒DEVI are illustrated in Figure 6.18. In this case the benefits of the stronger geometry as result
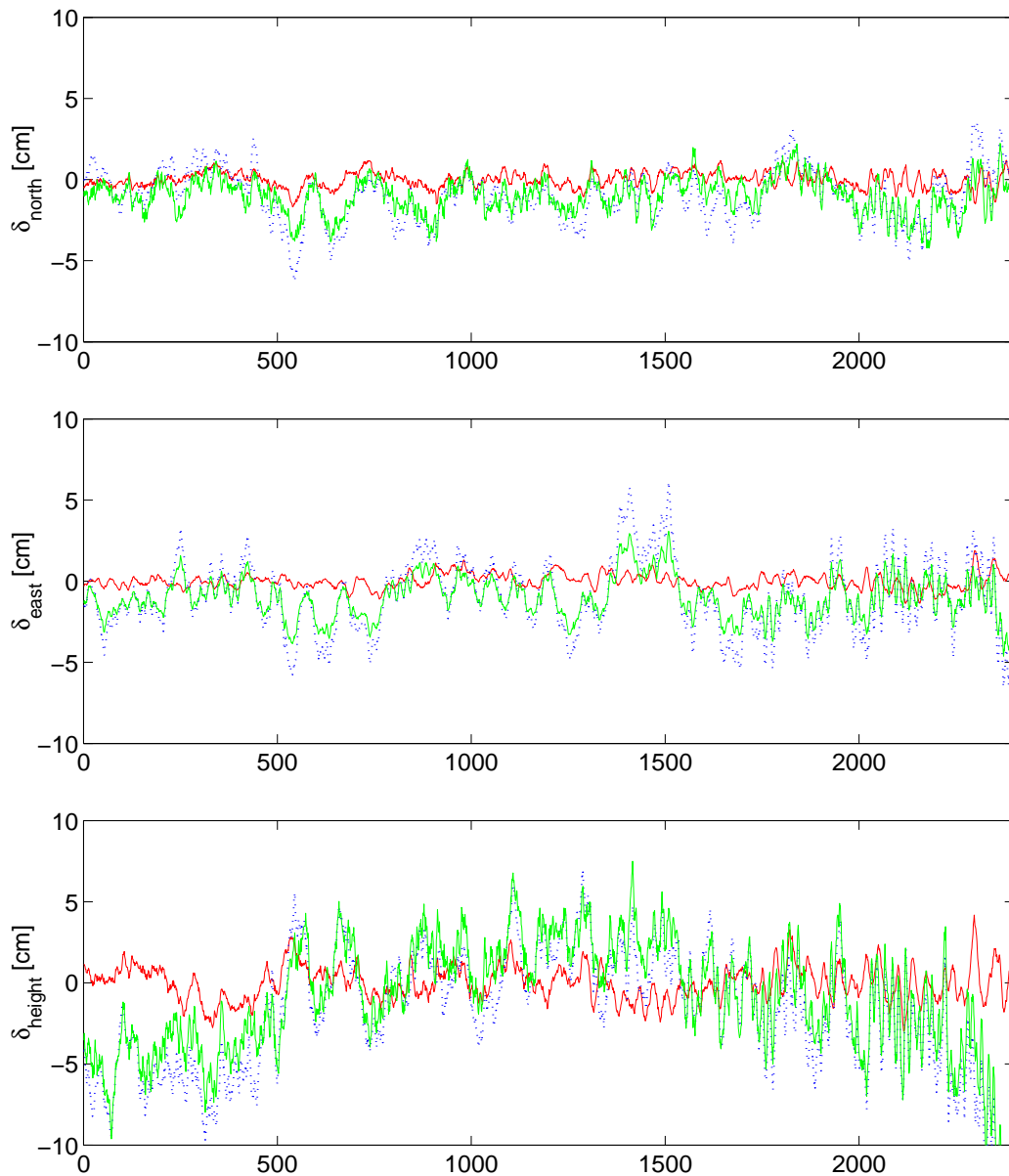
Figure 6.17: Time series of residual vector components [cm] (δ_{North}, δ_{East}, δ_{Height}) baseline HUXL⇒HYDE. Red line denotes residuals based on Scenario I, blue dotted line Scenario II and green line Scenario IV.

of the additional GEO based observations in particular for the scenarios where almost 50% of GPS satellites have been disabled can be seen.
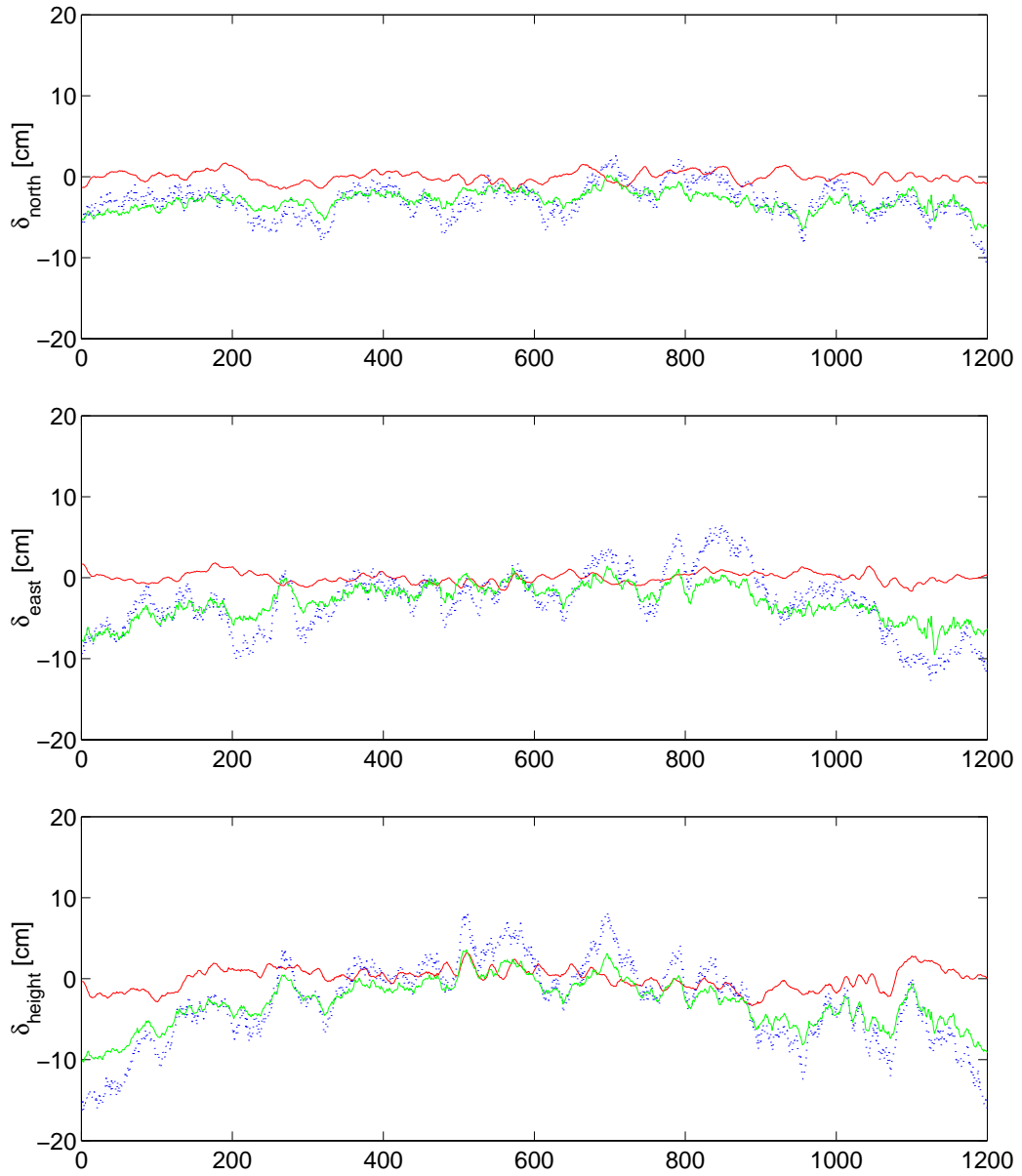
Figure 6.18: Time series of residual vector components [cm] (δ_{North}, δ_{East}, δ_{Height}) baseline HUXL⇒DEVI. Red line denotes residuals based on Scenario I, blue dotted line Scenario II and green line Scenario IV.

Chapter 7

Conclusions and recommendations

7.1 Conclusions

GPS will remain the main tool for satellite based positioning and precise baseline surveying over the next decade.

The first part of this thesis has addressed the recent developments in the modernisation programm of GPS. Furthermore, specific initiatives by the civil sector to enhance the performance of GPS using space based augmentation systems such as the US WAAS and Europe's EGNOS, have been explored.

The output of this part of the research has been the development of a framework to enable a reliable prediction of the GPS constellation so that an analysis of the impact of planned systems (augmentation or stand-alone) could be carried out. An example of such studies has been the impact of a combined use of GPS and Galileo after the latter achieves full operational capability in 2008. The results have been published in Ochieng et al. [2001].

Implications of expected technical parameters such as carrier-phase processing using three carrier frequencies as proposed for modernised GPS and for Galileo have been discussed briefly.

The second part of the thesis has addressed the more *"practical"* issues and attempted the specific issue of:

*"How to improve GPS positioning performance especially under difficult
urban and engineering conditions"*

The thesis has documented the successful attempt to enhance positioning performance of GPS by utilising EGNOS code and carrier-phase observations. The problems as connected with such integration process have been addressed and thoroughly analysed. The benefits of using GPS and EGNOS pseudo-ranges for single point positioning and navigation have been analysed and quantified. It has been shown that in cases where GPS may fail as navigation system EGNOS pseudo-ranges present a *"quick-to-achieve"* solution. The results presented in Chapter 4 show a significant gain in terms positioning quality and availability using additional EGNOS ranges within the positioning solution. Therefore, 20% increased positioning quality can be observed for the worst case of 50% GPS satellite blockage. The implications for the computation of satellite parameters especially for geostationary satellites, weighting strategies and necessary error corrections have been discussed in depth.

Encouraged by the promising results for single point positioning and navigation with pseudo-ranges, the research was taken one step further. The feasibility and benefit of integrating EGNOS L1 carrier-phase observations for kinematic baseline processing have been evaluated.

Since carrier-phase processing requires even more accurate modelling of all navigation system errors, an exhaustive study of the required correction models has been carried out and presented in the thesis. The corresponding implementation issues have been discussed in depth.

Since the GEO satellites transmit on the L1 frequency only, commonly used dual-frequency algorithms to account for ionospheric refraction are not directly relevant. Therefore, the physical properties of the ionosphere as well as algorithms for the derivation of ionospheric models have been studied in detail. Based on these findings a Kalman filter algorithm in conjunction with an algorithm for a 2-D parametrisation of ionospheric delays based on dual-frequency GPS data have been developed.

The model generated has been referred to as the *Station Specific Local Ionospheric Model (SSLIM)*. The SSLIM was subsequently tested for its impact on kinematic positioning with GPS and EGNOS carrier phase data, both in terms of the determination of carrier phase ambiguities and baseline computation. Three algorithms, the Least Squares Filtering, the Ambiguity Function Method (AFM) and the Least Square AMbiguity Decorrelation Adjustment (LAMBDA) method, have been investigated.

The comparison of the results show that, assuming cycle slips have been detected successfully, the LAMBDA method is superior to the others. There are two major reasons for this: the exhaustive use of all available information (past and current) and the ingenious method used to reduce and reshape the original ambiguity space.

The results with the Least Square AMbiguity Decorrelation Adjustment (LAMBDA) approach incorporating the SSLIM show significant gains in the quality of baseline computation when EGNOS GEO observations have been used. This is particularly true for long baselines, in cases when not enough GPS satellites are available or the geometric constellation is poor. Examples can be given with a 20% increase in success rate for ambiguity determination for the one kilometre baseline in the worst case of geometry and about 30% increase for the 70 kilometre baseline.

Finally it is important to note that although this research has made a significant contribution, ambiguity determination under harsh engineering conditions remains difficult. The approach presented here based on combining GPS and EGNOS GEO data and using a local ionospheric model leads to promising results. However further research is still required to realise the dream of reliable and continuous ambiguity resolution on-the-fly.

Assuming Galileo and/or modernised GPS (GPS III) achieve FOC, the third (fourth) carrier-frequency would enable faster and more reliable ambiguity determination.

7.2   Recommendations for further research

The research presented has shown promising results based on the utilisation of EG-NOS code and carrier-phase observations. The application of the proposed iono-spheric model has led to increased success rates in terms of ambiguity determination and quality of baseline computation.

As a result of the experience gained during this research, the following issues are recommended for further research in the field of carrier-phase processing using EGNOS observations and the computation of local ionospheric models:

- **Investigation of differential code and carrier biases:** This should involve an in depth evaluation of satellite and receiver code biases leading to an improved weighting function. The role of zero baseline tests in this should be investigated. This could lead to a weighting function with a general validity and contribute to an improved ionospheric model.

- **Investigation of network based solutions using multiple reference stations:** The evaluation of network-based ionospheric modelling could lead to high accuracy ionospheric estimates as well as to higher success-rates for ambiguity determination. An enhanced approach based on the virtual reference station (VRS) concept [cf. Vollath et al., 2000] could be a very good framework for local ionospheric modelling.

- **Investigation of possibilities for multipath calibration:** Based on different geometrical configurations for geostationary and medium orbit satellites it is may be possible to set up a procedure to adjust for station specific multipath patterns. The expectation is that GPS multipath should in general show more stochastic tendencies whereas GEO multipath should be largely deterministic.

- **Investigation of influence of different temporal and geodetic reference frames:** This depends on the availability of time offset estimates (ENT - GPS time) as proposed by EGNOS in the year 2003 and to be included in the SBAS

message type 12. Hence errors introduced by discrepancies in the temporal reference frames could be isolated and eliminated.

- **Re-evaluation of the EGNOS ionospheric model after Advanced Operational Capability (AOC) is achieved**: When EGNOS achieves AOC the GIVE value is expected to be 0.5 m (1σ). The date for the *"Operational Readiness Review"* is expected to be in April 2004. An ionospheric model of this quality available in real-time should be useful for "iono-seeding" to develop a local ionospheric model as proposed in this research. The filter convergence as well as the reliability of the SSLIM could be enhanced significantly. This would lead to enhanced availability and reliability of ambiguity determination. This technique could be used either for network based RTK solutions as well as for single baseline RTK.

- **Communication network based transmission of EGNOS messages:** It should be possible to set up a service to distribute EGNOS messages via any means of communication (ie. TCP/IP[1] as implemented in SISNET or GPRS[2]). One advantage here would be that the user does not require a GEO satellite to be visible. Hence there would be no need for a receiver capable of operating in SBAS mode. In this case ionospheric modelling capability for network based RTK systems could be enhanced greatly, by making use of the EGNOS ionospheric model.

- **Ionospheric modelling with GALILEO and modernised GPS:** Assuming GALILEO becomes a reality and/or that GPS is moderised within the next decade, ionospheric modelling could be enhanced greatly. This is particularly because of the availability of high quality code and carrier observations on at least three frequencies. It would be possible to implement new linear

---

[1]Transmission Control Protocol/Internet Protocol, the suite of communications protocols used to connect hosts on the Internet. TCP/IP uses several protocols, the two main ones being TCP and IP. It is de-facto standard for transmitting data over networks.

[2]General Packet Radio Service, a standard for wireless communications which runs at speeds up to 115 kilobits per second

combinations which are optimal in terms of error and ionospheric propagation. This could be used together with the algorithms implemented in the research to develop a local ionospheric model (to correct the single frequency EGNOS observation) with a very high level of accuracy and quality.

References

Al-Hafi, Y. M. (1998), Performance evaluation of GPS single epoch On-the-Fly ambiguity resolution, *Navigation: The Journal of the Institute of Navigation*, 4(44):pages 479–487.

Aurenhammer, F. (1991), Voronoi diagrams - a survey of a fundamental geometric data structure, *ACM Computing Surveys*, 23:pages 345–405.

Balthazor, R. L. and Moffett, R. J. (1997), A study of atmospheric gravity waves and travelling ionospheric disturbances at equatorial latitudes, *Annales Geophysicae*, 15:pages 1048–1056.

Barnes, J. B., Ackroyd, N., and Cross, P. A. (1998), Stochastic modelling for very high precision real time kinematic GPS in an engineering environment, Technical report, Department of Geomatic Engineering, University College London.

Bent, R. B., Llewellyn, S. K., and Schmid, P. E. (1972), A highly successful empirical model for the worldwide ionospheric electron density profile, Technical report, DBA Systems, Melbourne, Florida.

Beser, J. and Parkinson, B. (1982), The application of NAVSTAR differential GPS in the civilian community, *Journal of Navigation*, 29(2):pages 107–136.

Bilitza, D. (2001), International reference ionosphere 2000, *Radio Science*, 36(2):pages 261–275.

Bisnath, S. B., Collins, J. P., and Langley, R. B. (1997), GPS multipath assessment of the Hiberina oil platform, Technical report, Geodetic Research Laboratory, Department of Geodesy and Geomatics Engineering, University of New Brunswick.

Black, H. D. (1978), An easily implemented algorithm for tropospheric range correction, *Journal of Geophysical Research*, 83(B4).

Blewitt, G. and Lichten, S. (1992), GPS carrier phase ambiguity resolution up to 12000 km: Results from the GIG'91 experiment, in *Sixth International Geodetic Symposium on Satellite Positioning*, pages 462–471, Columbus, Ohio.

Bonillo-Martínez, C., Toledo-López, M., and Romay-Merino, M. (1999), The benefits of the GPS three frequencies on the ambiguity resolution techniques, in *Proceedings of The 12th International Technical Meeting of the Satellite Division of the Institute of Navigation*, pages 1737–1746, Nashville, TN.

Braasch, M. S. (1996), Multipath effects, in Parkinson, B. W. and Spilker, J. J. (Editors), *Global Positioning System: Theory and Applications*, volume 1, pages 547–568, American Institute of Aeronautics and Astronautics, Inc., Washington, D.C., U.S.A.

Braun, J., Rocken, C., and Ware, R. (2001), Validation of line-of-sight water vapor measurements with GPS, *Radio Science*, 36:pages 459–472.

Brown, R. G. and Hwang, P. Y. C. (1983), A Kalman filter approach to precision GPS geodesy, *Navigation: The Journal of The Institute of Navigation*, 30(4):pages 338–349.

Brown, R. G. and Hwang, P. Y. C. (1997), *Introduction to Random Signals and Applied Kalman Filtering : With MATLAB Exercises and Solutions*, John Wiley & Sons, New York, Chichester, 3 edition.

Brunner, F. K. and Gu, M. (1991), An improved model for dual frequency ionospheric correction of GPS observations, *Manuscripta Geodetica*, 16:pages 205–214.

Clynch, J. R., Coco, D. S., Coker, C., and Bishop, G. (1989), A versatile GPS iono- spheric monitore: High latitude measurements of TEC and scintilation, in *Pro- ceeding of The 2th International Technical Meeting of the Satellite Division of the Institute of Navigation*, pages 445–450, Institut of Navigation, Colorado Springs.

Collins, J. P. and Langley, R. B. (1997), Estimating the residual tropospheric delay for airborne GPS positioning - a summary, in *Presented at the 1997 Scientific Assembly of the IAG*, International Association for Geodesy, Rio de Janeiro, Brazil.

Comp, C. J. and Axelrad, P. (1996), An adaptive SNR-based carrier phase multipath mitigation technique, in *Proceedings of The 9th International Technical Meeting of the Satellite Division of the Institute of Navigation*, pages 683–697, Institute of Navigation, Kansas City, Missouri.

Corbett, S. J. and Cross, P. A. (1995), GPS single epoch ambiguity resolution, *Survey Review*, 33(257):pages 149–160.

Counselman, C. C. and Gourevitch, S. A. (1981), Miniature interferometer terminals for Earth Surveying: Ambiguity and multipath with Global Positioning System, *IEEE Transactions on Geoscience and Remote Sensing*, GE-19(4):pages 244–252.

CSIC (1998a), GLONASS interface controll document, Technical report, Coordina- tion Scientific Information Center.

CSIC (1998b), Parameters on Earth 1990 PZ-90, Technical report, Coordination Sci- entific Information Center (CSIC), Moscow, Russia.

Davies, K. (1990), *Ionospheric Radio*, Peter Peregrinus Ltd., London.

de Jonge, P. (1994), GPS ambiguity resolution for navigation, rapid static surveying, and regional networks.

de Jonge, P. (1998), *A Processing Strategy for the Application of the GPS in Networks*, Ph.D. thesis, Department of Mathematical Geodesy and Positioning, Technical University Delft.

de Jonge, P. and Tiberius, C. (1994), The LAMBDA method for integer ambiguity estimation: Implementation aspects, number 12 in LGR-Series, Delft geodetic computing centre.

Dierendonck, A. J. V., Fenton, P., and Ford, T. (1992), Theory and performance of narrow correlator spacing in a GPS receiver, *Journal of Navigation*, 39(3).

DoD (1995), *Global Positioning System: Standard Positioning Service Signal Specification*, United States Department of Defense.

DoD (2001a), *Global Positioning System: Interface Control Document*, United States Department of Defense.

DoD (2001b), *Global Positioning System: Standard Positioning Service Signal Specification*, United States Department of Defense.

Dong, D. and Bock, Y. (1989), Global positioning system network analysis with phase ambiguity resolution applied to crustal deformamtion studies in california, *Journal of Geohyical Research*, 94(B4):pages 3949–3965.

Euler, H. J. and Goad, C. C. (1991), On optimal filtering of GPS dual frequency observations without using orbit informations, *Bulletin Géodésique*, 65:pages 130–143.

Euler, H. J. and Landau, H. (1992), Fast ambiguity resolution on-the-fly for real time applications.

Feltens, J., Dow, J., Martin-Mur, T., Romero, I., and Garcia-Martinez, C. (1999), Routine production of ionosphere TEC maps at ESOC, in *Proceedings of the IGS Analysis Centers Workshop*, La Jolla, California,.

Feltens, J. and Schaer, S. (1998), IGS products for the ionosphere, in *IGS Analysis Centers Workshop*, Darmstadt, Germany.

Frei, E. (1991), GPS - fast ambiguity resolution approach "FARA": Theory and application, in *XX General Assembly of the IUGG, IAG Symposium GM1/4*, Vienna.

Frei, E. and Beutler, G. (1990), Rapid static positioning based on the fast ambiguity resolution approach (FARA): Theory and first results, *Manuscripta Geodetica*, 15(6):pages 325–356.

Frei, E. and Schubernigg, M. (1992), GPS surveying using the "Fast Ambiguity Resolution Approach (FARA)", in *34th Australian Surveyors Congress and the 18th National Surveying Converence*, Cairns, Australia.

FRNP (1999), Federal radionavigation plan (FRNP), Technical report.

Gelb, A. (1974), *Applied Optimal Estimation*, M.I.T. Press, Cambridge, Mass., London.

Goad, C. (1992), Robust techniques for determining GPS phase ambiguities, in *Proceedings Int. Geod. Symp. On Satellite Positioning*, pages 245–254, Columbus, Ohio.

Goad, C. and Yang, M. (1994), On automatic precision airborne GPS positioning, in *Proceedings of KIS'94*, pages 131–138, Banff.

Goad, C. C. (1990), Optimal filtering of pseudoranges and phases from single-frequency GPS receiver, *Journal of Geodesy*, 37(3):pages 249–262.

Grejner-Brzezinska, D. A., Da, R., and Toth, C. (1998), GPS error modeling and OTF ambiguity resolution for high-accuracy GPS/INS integrated system, *Journal of Geodesy*, 72:pages 626–638.

Gross, R. S., Eubanks, T. M., Steppe, J. A., Freedman, A. P., Dickey, J. O., and Runge, T. F. (1998), A Kalman-filter-based approach to combining independent earth-orientation series, *Journal of Geodesy*, 72:pages 215–235.

Gurtner, W. (2000), RINEX: Receiver independent exchange format version 2.10, Technical report, Astronomical Institute, University of Berne.

Han, S. (1997), Quality-control issues relating to instantaneous ambiguity resolution-for real-time GPS kinematic positioning, *Journal of Geodesy*, 71:pages 351–361.

Hansen, A. J., Blanch, J., Walter, T., and Enge, P. (2000), Ionospheric correlation analysis for WAAS: Quiet and stormy, in *Proceedings of The 12th International Technical Meeting of the Satellite Division of the Institute of Navigation*, Institute of Navigation, Salt Lake City, Utah.

Hansen, A. J., Walter, T., and Enge, P. (1997), Ionospheric correction using tomography, in *Proceedings of The 10 thInternational Technical Meeting of the Satellite Division of the Institute of Navigation*, Institute of Navigation, Kansas City, Missouri.

Hein, W. G., Godet, J., Issler, J. L., C., M. J., Erhard, P., Lucas-Rodrigues, R., and Pratt, T. (2002), Status of Galileo frequency and signal design, Technical report, European Commission, Galileo Signal Task Force, Brussels.

Hernández-Pajares, M., Juan, J. M., and Sanz, J. (1999), New approaches in global ionospheric determination using ground GPS data, *Journal of Atmospheric and Solar-Terrestrial Physics*, 61:pages 1237–1247.

Hernández-Pajares, M., Juan, J. M., Sanz, J., and Colombo, O. L. (2000), Application of ionospheric tomographe to real-time GPS carrier-phase ambiguity resolution, at scales of 400-1000 km and with high geomagnetic activity, *Geophysical Research Letters*, 27(13):pages 2002–2012.

Hoffmann-Wellenhof, B., J.Collins, and Lichtenegger, H. (1997), *GPS Theory and Practice*, Springer-Verlag, New York.

Hopfield, H. (1969), Two-quartic tropospheric refractivity profile for correcting satellite data, *Journal of Geophysical Research*, 74(18).

Iz, H. B., Ge, M., and Chen, Y. Q. (1998), Grid point search algorithm for fast integer ambiguity resolution, *Journal of Geodesy*, 72:pages 639–643.

Joosten, P., Teunissen, P., and Jonkman, N. (1999), GNSS three carrier phase ambiguity resolution using the LAMBDA-method, Mathematical Geodesy and Positioning Delft University of Technology.

Kim, D. and Langley, R. B. (1999), An optimized least-squares technique for improving ambiguity resolution and computational efficiency, in *Proceedings of the 12th International Technical Meeting of the Satellite Division of the Institute of Navigation*, pages 1579–1588, Institute of Navigation.

Klobuchar, J. A. (1987), Ionospheric time-delay algorithm for single-frequency GPS users, *IEEE Transactions on Aerospace and Electronic Systems*, AES-23(3):pages 325–331.

Komjathy, A. (1997), *Global Ionospheric Total Electron Content Mapping Using the Global Positioning System*, Ph.D. thesis, University of New Bruswick, Fredericton, NB, Canada, UNB Technical Report 188.

Kunches, J. M. (2000), In the teeth of cycle 23, in *Proceeding of The 13th International Technical Meeting of the Satellite Division of the Institute of Navigation*, Institute of Navigation, Salt Lake City, UT.

Langley, R. (1998), *Propagation of the GPS Signals. in Teunissen and Kleusberg [1998]*, chapter 2, pages 103–140, Springer Verlag, New York.

Leick, A. (1995), *GPS Satellite Surveying*, John Wiley & Sons Inc., New York.

Li, Z., Schwarz, K. P., and El-Mowafy, A. (1993), GPS multipath detection and reduction using spectral techniques, in *Proceedings of the General Meeting of IAG*, International Association for Geodesy.

Lollock, R. M. (2001), Global positioning system (GPS) modernisation, Presentation given at the NATO GPS Technical Workshop.

Mader, G. A. (1992), Rapid static and kinematic global position system solutions using the ambiguity function technique, *Journal of Geophysical Research*, 97(B3):pages 3271–3283.

Malys, S., Larezos, M., Gottschalk, S., Mobbs, S., Feess, W., Merrigan, M., and Mathon, W. (1997), The GPS accuracy improvement initiative, in *Proceeding of The 10th International Technical Meeting of the Satellite Division of the Institute of Navigation*, pages 375–384, Institute of Navigation, Kansas City, Missouri.

Mannucci, A. J., Wilson, B. D., and D., E. C. (1993), A new method for monitoring the Earth's ionospheric content using the GPS global network, in *Proceeding of The 6th International Technical Meeting of the Satellite Division of the Institute of Navigation*, pages 1323–1332, Institut of Navigation, Salt Lake City.

McNally, A. (1997), *Internationaler Atlas*, Rand McNally & Westermann, Braunschweig.

Melbourne, W. G. (1985), The case for ranging in GPS based geodetic systems, in *Proceedings of the First International Symosium on Precise Positioning Using the Global Positioning System*, Rockville, MD, USA.

Merrigan, M., Swift, E., Wong, R., and Jaffel, J. (2002), A refinement to the World Geodetic System 1984 reference frame, in *Proceeding of The 15th International Technical Meeting of the Satellite Division of the Institute of Navigation*, Institute of Navigation, Portland, OR.

Mevart, L. (1995), *Ambiguity Resolution Techniques in Geodetic and Geodynamic Applications of the Global Positioning System*, Ph.D. thesis, Astronomical Institute, University of Bern, Switzerland.

Mohamed, A. H. and Schwarz, K. P. (1999), Adaptive Kalman filtering for INS/GPS, *Journal of Geodesy*, 73:pages 193–203.

Montenbruck, O. and Gill, E. (2000), *Satellite Orbits, Models Methods Applications*, Springer, Berlin, Heidelberg, New York.

NovAtel Inc. (1997), *ProPak II^{TM} OM-20000020*, Calgary, Canada, 2 edition.

NovAtel Inc. (1998), *MiLLennium GPSCard Software Version 4.50 Command Descriptions Manual*, Calgary, Canada.

Ober, P. B. (2001), SBAS integrity concept - Towards SBAS validation, Technical report, Eurocontrol.

Ochieng, W., Sauer, K., Cross, P. A., Sheridan, K., Iliffe, J., Lannelongue, N., S.and Ammour, and Petit, K. (2001), Potential performance levels of a combined Galileo/GPS navigation system, *Royal Institute of Navigation Journal of Navigation*, 2(54):pages 186 –197.

ORD (1998), *Civil Positioning Velocity, and Timing Requirements*, chapter GPS Operational Requirements Document (ORD), Appendix F, pages 1–12.

Parkinson, B. W., Spilker Jr., J. J., Axelrad, P., and P., E. (Editors) (1996), *Global Positioning System: Theory and Applications*, volume 1-2, AIAA, Washington.

Press, W. H., Teukolsky, S. A., Vetterling, W. T., and Flannery, B. P. (1992), *Numerical Recipes in C: The Art of Scientific Computing*, Cambridge University Press, Cambridge, New York, Port, Chester, Melbourne, Sydney.

Raquet, J. F. (1998), *Development of a Method for Kinematic GPS Carrier-Phase Ambiguity Resolution Using Multiple Reference Receivers*, Ph.D. thesis, University of Calgary, Department of Geomatics Engineering.

Rawer, K., Bilitza, D., and Ramakrishnan, S. (1978), Goals and status of the international reference ionosphere, *Geophysical Review*, 16:pages 177–181.

Remondi, B. W. (1984), *Using the Global Positioning System (GPS) Phase Observable for Relative Geodesy: Modelling, Processing, and Results*, Ph.D. thesis, Center of Space Research, University of Texas at Austin.

Remondi, B. W. (1986), Performing centimeter level surveys in seconds with GPS carrier phase: Initial results, in *Fourth Internatinal Geodetic Symposium on Satellite Positioning*, Austin, TX.

Remondi, B. W. (1992), Real-time centimeter-accuracy GPS without static initialization, National Gedodetic Survey.

Rothacher, M. and Mevart, L. (1996), *Bernese Software Version 4.0*, Astronomical Institute University of Berne.

Roturier, B., Chatre, E., and Ventura-Traveset, J. (2001), The SBAS integrity concept standardised by ICAO - application to EGNOS, in *Proceedings of GNSS 2001*, Sevilla, Spain.

RTCA-DO-299 (1996), Minimum operational performance standards for GPS wide area augmentation system airborne equipment - Change 1, Technical Report RTCA/DO-229, Radio Technical Commission for Aviation.

Saastamoinen, J. (1973), Contribution to the theory of atmospheric refraction, *Bulletin Géodésique*, 107(1):pages 13–14.

Sandhoo, K., Turner, D., and Shaw, M. (2000), Modernization of the Global Positioning System, in *Proceedings of The 13th International Technical Meeting of The Satellite Division of The Institute of Navigation*, pages 2175–2183, Institute of Navigation, Salt Lake City, Utah.

Sandwell, D. T. (1987), Biharmonic spline interpolation of GEO-3and seasat altemeter data, *Geophysical resarch letters*, 14(2):pages 139–147.

Sauer, K. (2000), Integrated kinematic positioning models using GPS/GLONASS/GEO observations, Technical report, Imperial College of Science and Technology, Centre for Transport Studies, London, United Kingdom.

Sauer, K. and Ochieng, W. Y. (2002a), Integrated use of GPS and EGNOS carrier phase observations for high precision kinematic positioning, in *Proceeding of The 15th International Technical Meeting of the Satellite Division of the Institute of Navigation*, Institute of Navigation, Portland, OR, in print.

Sauer, K. and Ochieng, W. Y. (2002b), Integrated use of GPS and EGNOS carrier phase observations for high precision kinematic positioning - first experiences, *Journal of Geospatial Engineering*, 4(1):pages 59–67.

Schaer, S. (1999), *Mapping and Predicting the Earths Ionosphere Using the Global Positioning System*, Ph.D. thesis, Universität Bern.

Schaer, S., Beutler, G., Mevart, L., Rothacher, M., and Wild, U. (1995), Global and regional ionosphere models using the GPS double difference phase observable frequency, in *Proceedings of the 1995 IGS Workshop*, Silver Spring, MD, USA.

Schaer, S., Gurtner, W., and Feltens, J. (1998), IONEX: The IONosphere map EXchange format version, in *Proceedings of the 1998 IGS Analysis Centers Workshop*, Darmstadt, Germany.

Seeber, G. (1993), *Satellite Geodesy*, Walter de Gruyter, Berlin and New York.

Spofford, P. R. and Remondi, B. W. (1993), The national geodetic standard GPS format SP3, Technical report, US National Geodetic Survey, Silver Spring, Maryland.

Strang, G. and Borre, K. (1998), *Linear Algebra, Geodesy and GPS*, John Wiley & Sons, Inc., New York.

Suard, N. (2000), ESTB SIS user interface description, Technical report, European Space Agency, GNSS-1 Project Office.

Teunissen, P. J. G. (1993), Least-squares estimation of the integer GPS ambiguities, International Associaton of Geodesy, Beijing, China.

Teunissen, P. J. G. (1997), The geometry free GPS ambiguity search space with weighted ionosphere, *Journal of Geodesy*, 71:pages 541–551.

Teunissen, P. J. G. (1998), Success probability of integer GPS ambiguity rounding and bootstrapping, *Journal of Geodesy*, 72:pages 606–612.

Teunissen, P. J. G. and de Jong, C. D. (1998), Reliability of GPS cycle slip and outlier detection, in *Proceedings INSMAP98*, Melbourne, FL, USA,.

Teunissen, P. J. G., de Jonge, P., and Tiberius, C. (1995), The LAMBDA method for fast GPS surveying, pages 1–8, Presented at the International Symposium"GPS Technology Applications" Bucharest, Romania, September 26-29.

Teunissen, P. J. G., de Jonge, P. J., and Tiberius, C. C. J. M. (1997a), The least-squares ambiguity decorrelation adjustment: Its performance on short GPS baselines and short observation spans, *Journal of Geodesy*, 71:pages 589–602.

Teunissen, P. J. G., de Jonge, P. J., and Tiberius, C. C. J. M. (1997b), Performance of the LAMBDA method for fast GPS ambiguity resolution, *Navigation: The Journal of The Institute of Navigation*, 44(3):pages 373–383.

Teunissen, P. J. G. and Kleusberg, A. (Editors) (1998), *GPS for Geodesy*, Springer Verlag, New York.

Teunissen, P. J. G. and Tiberius, C. (1994), Integer least-squares estimation of the GPS phase ambiguities, in *International Symposium on Kinematic Systems in Geodesy, Geomatics and Navigation, Banff, Alberta, Canada, Aug 30 – Sept 2, 1994*.

Tiberius, C. and de Jonge, P. (1995), Fast positioning using the LAMBDA method, Delft Geodetic Computing Centre (LGR) Faculty of Geodetic EngineeringDelft University of TechnologyThijsseweg 11, NL-2629 JA Delft.

Torge, W. (1991), *Geodesy*, W. de Gruyter, Berlin-New York, 2nd edition.

Townsend, B. R. and Fenton, P. C. (1994), A practical approach to the reduction of pseudorange multipath errors in a L1 GPS receiver, in *Proceedings of ION 1994*, Institute of Navigation, Salt Lake City.

Townsend, B. R., Nee, D. J. R. V., Fenton, P. C., and Dierendonck, K. J. V. (1995), Performance evaluation of the multipath estimating delay lock loop, in *ION National Technical Meeting*, Anaheim. California,.

Vaniček, P. and Krakiwski, E. (1982), *Geodesy: The Concepts*, North-Holland, Amsterdam-New York.

Vollath, U., Birnbach, S., Landau, H., and Fraile-Ordoñez, J. (1999), Analysis of three-carrier ambiguity resolution technique for precise relative positioning in GNSS-2, *Journal of Navigation*, 46(1):pages 13–23.

Vollath, U., Buecherl, A., Landau, H., Pagels, C., and Wagner, B. (2000), Multi-base RTK positioning using virtual reference stations, in *Proceedings of ION GPS 2000*, pages 123–131, Institute of Navigation, Salt Lake City, UT.

Wanninger, L. and May, M. (2000), Carrier phase multipath calibration of GPS reference sites, in *Proceeding of The 13th International Technical Meeting of the Satellite Division of the Institute of Navigation*, pages 132–144, Institute of Navigation, Salt Lake City, Utah.

Watson, D. F. (1992), *Contouring - Aguide to the Analysis and Display of Spatial Data*, volume 10 of *Computer Methods in Geosciences*, Pergamon Press, Oxford, New York, first edition.

Welch, G. and Bishop, G. (2002), An introduction to the Kalman filter, Technical report, Department of Computer ScienceUniversity of North Carolina, Department of Computer Science University of North Carolina at Chapel Hill Chapel Hill, NC 27599-3175.

WHPR (2000a), Improving the civilian global positioning system, White House Press Release.

WHPR (2000b), Statement by the president regarding the united sates decision to stop global positioning system accuracy degradiation, White House Press Release.

Wild, U. (1994), *Ionosphere and Geodetic Satellite Systems: Permanent GPS Traking Data for Modelling and Monitoring*, Ph.D. thesis, Universität Bern.

Woodward, P. (1964), *Probability and Information Theory with Applications to Radar*, Pergamon Press., Oxford, 2nd edition.

Wübbena, G. (1985), Software developments for geodetic positioning using TI-4100 code and carrier measurements, in *Proceedings of the First International Symosium on Precise Positioning Using the Global Positioning System*, Rockville, MD, USA.

Frequently used acronyms

AFM Ambiguity Function Method

AOC Advanced Operational Capability

AOR-E Atlantic Ocean Region East

AS Anti Spoofing

BMCS Backup Master Control Station

CDMA Code Division Multiple Access

CODE Center for Orbit determination in Europe, Berne, Switzerland

CS Control segment

DCB Differential Code Bias

DoD United States Department of Defence

DOP Dilution of Precision

DoT United States Department of Transport

ECAC European Civil Aviation Conference

EGNOS European Geostationary Navigation Overlay Service

ENT EGNOS Network Time

ESA European Space Agency

ESTB EGNOS System Test Bed Test facility for EGNOS

BIPM Bureau International des Poids et Mesures

FDMA Frequency Division Multiple Access

FOC Full Operational Capability

FRNP United States Federal Radio Navigation Plan

GIVD Grid Ionospheric Vertical Delay

GIVE Grid Ionospheric Vertical Error

GLONASS GLObalnaya NAvigatsionnaya Sputnikovaya Sistema

GPS Global Positioning System

GNSS Global Navigation Satellite Systems

HMI Hazardously Misleading Information

ICAO International Civil Aviation Organisation

IGP Ionospheric Grid Points

IGS International GPS Service for Geodynamics

IGU International Geophysical Union

IOC Initial Operational Capability

IONEX IONOsphere EXchange Format

IOR Indian Ocean Region

JPL Jet Propulsion Laboratory, Pasadena, United States

LAMBDA Least Square AMbiguity Decorrelation Adjustment

MCC Mission Control Centre

MCS Master Control Station

MEO Medium Earth Orbit

NASA National Aeronautic and Space Administration

NATO North Atlantic Treaty Organisation

NIMA National Imagery and Mapping Agency

NLES Navigation Land Earth Stations

NPA Non Precision Approach

NRCan Natural Resources Canada, Ottawa, Ontario

NSE Navigation System Error

OAC-I Oceanic Area Control Center I

PPS Precise Positioning Service

PRN Pseudo Random Noise

RIMS Ranging and Integrity Monitoring Stations

RINEX Receiver Independent EXchange

RMS Root Mean Square

RTCA Radio Technical Commission for Aviation

RTCM Radio Technical Commission for Marine Services

SA Selective Availability

SARPS Standards and Recommended Practices

SBAS Spaced Based Augmentation Systems

SIS Signal-in-Space

snr signal-to-noise ratio

SPP single point positioning

SPS Standard Positioning Service

TEC Total Electron Content

UDRE User Differential Range Error

UDREI User Differential Range Error Indicator

UERE User Equivalent Range Error

UIRE User Ionospheric Range Error

URE User Range Error

UPC Polytechnical University of Catalonia, Barcelona, Spain

USNO United States Naval Observatory

UTC Coordinated Universal Time

VDE Vertical Delay Estimate

WAAS Wide Area Augmentation System

WAD Wide Area Differential

Appendix A

Data encryption and processing algorithms

A.1 Decryption for NovAtel data logs

A.1.1 Description of applicable NovAtel logs

The used NovAtel Millennium WAAS receiver is capable of output a continuous data stream containing the a-priory specified data logs. The communication between the used Windows PC and the receiver is either realised via a firmware terminal (GP-Sonl32) or the Windows hyper terminal. The corresponding commands are uploaded to the receiver in a ASCII[1] symbol stream. The downstream data in form of NovAtel data logs is directly stored in the specified location.

A complete overview about all applicable commands and data logs is given in NovAtel Inc. [1998]. The data logs as relevant for the research are described as follow:

A.1.1.1 Framed Raw Navigation Data ($FRMA/B)

This message contains the raw framed navigation data (i.e. SBAS data). For each tracked PRN an individual message is issued. The message is updated with each acquired new frame.

Table A.1 contains the corresponding log content. Whereas the channel tracking status specifies possible faults in the satellite tracking, the applicable carrier frequency and the system identifier. The corresponding symbols in the framed raw data are decrypted according to Section A.1.2.

---

[1]American Standard Code for Information Interchange. The recently implemented version is based on the ISO-646-US-ASCII norm

Table A.1: $FRMA log content [cf. NovAtel Inc., 1998]

Field number	Field type	Data Description
1	$FRMA	Log header
2	week	GPS week number
3	seconds	GPS seconds into the week
4	prn #	PRN of satellite from which data originated
5	cstatus	Channel Tracking Status
6	# of transmitted bits	# of bits transmitted in the message. 250 for SBAS, 300 for GPS and 85 for GLONASS.
7	framed raw data	One field of raw framed navigation data.
8	*xx	Checksum
9	[CR][LF]	Sentence terminator
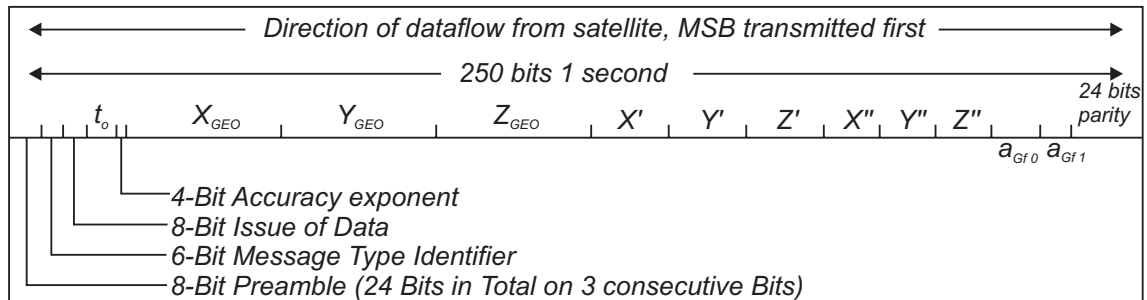
Figure A.1: Message type 9 (Geo navigation) format [cf. RTCA-DO-299, 1996]

These data set contain the SBAS-relevant information. Hence they are broken down further into:

A.1.1.1.1 **Message type 9**   Message type 9 contains the components as necessary to compute the satellite positions of the geostationary satellites and the corresponding satellite clock and frequency offsets. The binary data stream containing 250 bits per second is represented as a hexadecimal sequence. Whereas each binary record is encrypted according to RTCA-DO-299 [1996] as depicted in Figure A.1.

A.1.1.1.2 **Message type 18**   This message type contains the specified locations of the Ionospheric Grid Points (IGP). The location is kept flexible to facilitate possible changes to account for large variations in the ionospheric model as computed by ESTB
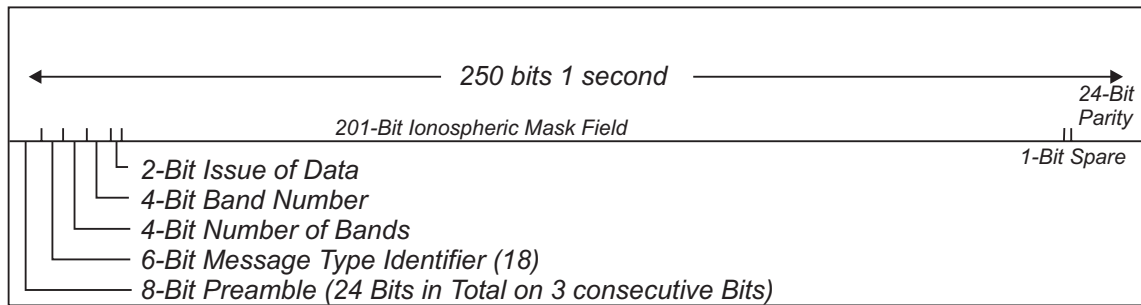
Figure A.2: IGP grid point positions [cf. RTCA-DO-299, 1996]
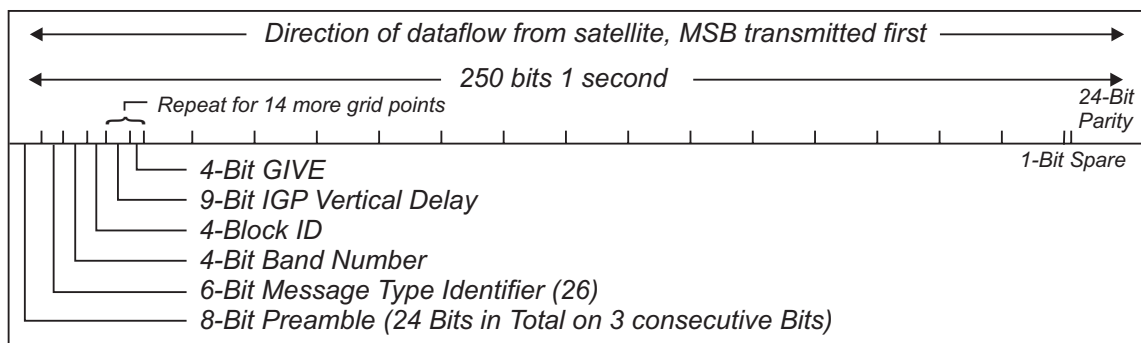
Figure A.3: Message type 26 IGP vertical delays and GIVE format [cf. RTCA-DO-299, 1996]

[cf. RTCA-DO-299, 1996, Chapter 4.4.9 p.32]. Figure A.2 contains the applicale components of the data stream.

A.1.1.1.3 **Message type 26** Message type 26 contains the ionospheric correction message. It provides the user with vertical delay estimates and the corresponding accuracy estimate (2σ). The geographic location of the values is in accordance with in message type 18 transmitted grid point locations. The data stream within message type 26 is given in Figure A.3.

A.1.1.2 **Channel Range Measurements ($RGEA)**

$RGEA contains the channel range measurements for the currently observed satellites. Furthermore it contains an estimate for the tracking error of the pseudo-range and carrier phase observable. Furthermore it contains a channel tracking status describing further applicable information about carrier frequency, system, correlator spacing, code type and tracking status etc. The corresponding software module in the devel-

oped *GNSSLab* environment extracts the pseudo-range, carrier-phase measurements and the corresponding error estimates.

Table A.2 gives the complete content of the used $RGEA log.

Table A.2: $RGEA log content [cf. NovAtel Inc., 1998]

Field number	Field type	Data Description
1	$RGEA	Log header
2	week	GPS week number
3	seconds	GPS seconds into the week
4	# obs	Number of satellite observations with information to follow
5	rec status	Receiver self-test status
6	prn	Satellite PRN # (1-130) of range measurement
7	psr	Pseudorange measurement (m)
8	psr std	Pseudorange measurement standard deviation (m)
9	adr	Carrier phase, in cycles (accumulated Doppler range)
10	adr std	Estimated carrier phase standard deviation (cycles)
11	dopp	Instantaneous carrier Doppler frequency (Hz)
12	C/N_0	Signal to noise density ratio $C/N_0 = 10(log_{10}(S/N_0))$ (dB-Hz)
13	locktime	Number of seconds of continuous tracking (no cycle slipping)
14	ch-tr-status	Hexadecimal number indicating phase lock, channel number and channel tracking state
...	...	Next PRN #, psr, psr std, adr, adr std, dopp, C/N_0, locktime, ch-tr-status
...	...	...
...	...	Last PRN #, psr, psr std, adr, adr std, dopp, C/N_0, locktime, ch-tr-status
variable	*xx	Checksum
variable	[CR][LF]	Sentence terminator

A.1.1.3 Raw GPS Ephemeris ($REPA)

This log contains the raw binary information for the GPS navigation message subframes one, two and three for the corresponding satellite [DoD, 2001b]. First the data stream (hexadecimal symbols) is converted to a binary data stream according

to Section A.1.2 and subsequently it is decrypted according to DoD [2001b] to a complete set of GPS epheris data.

Table A.3: $REPA log content [cf. NovAtel Inc., 1998]

Field number	Field type	Data description
1	$REPA	Log header
2	prn	PRN of satellite from the data is originated
3	subframe1	Subframe 1 of ephemeris data (60 hex characters)
4	subframe2	Subframe 2 of ephemeris data (60 hex characters)
5	subframe3	Subframe 3 of ephemeris data (60 hex characters)
6	*xx	Checksum
7	[CR][LF]	Sentence terminator

A.1.2 Decryption of hexadecimal represented binary data

A part of the NovAtel logs was encrypted as hexadecimal binary data the bit length, scale factors and least significant bits (LSB) as applicable for each data are described in Section A.1.1.1. The following Table A.4 is implemented in code to encrypt a sequence of hexadecimal symbols to a sequence of binary symbols. The applicable

Table A.4: Hexadecimal - binary equivalents

HEX	BIN	HEX	BIN
0	0000	8	1000
1	0001	9	1001
2	0010	A	1010
3	0011	B	1011
4	0100	C	1100
5	0101	D	1101
6	0110	E	1110
7	0111	F	1111

data stream was parsed and on a symbol-by-symbol basis encrypted.

Appendix B

Used data formats for observations, combined orbit and ionospheric information

B.1 Adapted RINEX and SP3 file format

Two well-known data formats have been used to accommodate the changes because of the utilisation of GEO satellite PRN numbers. For this purpose the RINEX format [cf. Gurtner, 2000] and the SP3 format [cf. Spofford and Remondi, 1993] were slightly adapted.

Since both file format do not support three-digit PRN numbers, 50 was subtracted from the corresponding PRN number for the geostationary satellite (i.e. 120 and 122). Throughout all applicable software modules PRN bigger than 50 have been assumed to be geostationary. This must kept in mind in case GLONASS data is planned to be used.

The following Figures B.1 and B.2 give examples (header information and first data set) of the adapted version of the RINEX and the SP3 format respectively.

B.2 IOnosphere EXchange data format IONEX

The IONOsphere EXchange Format (IONEX) file format has been used to represent the local ionospheric models as implemented and derived throughout the research. The following Figures B.3 and B.4 show examples for the header part and the data part of one IONEX file respectively.

```
    2.10            OBSERVATION DATA      M (MIXED)       RINEX VERSION / TYPE
  GNSSLab2rinex.m                  ICEGG   21-Jun-2001 16:43  PGM / RUN BY / DATE
                                              HUXL     MARKER NAME
    Knut Sauer                                ICEGG    OBSERVER / AGENCY
          00000   Novatel ProPac OEM3                  REC # / TYPE / VERS
          00000   Novatel A502 Choke                   ANT # / TYPE
         3978707.2657   -12167.3143   4968408.6634     APPROX POSITION XYZ
              0.0000         0.0000         0.0000      ANTENNA: DELTA H/E/N
      1     1                                           WAVELENGTH FACT L1/2
      6    P1    L1    D1    P2    L2    D2             # / TYPES OF OBSERV
     2001     3    22     8    13   30.0000             TIME OF FIRST OBS
     2001     3    23     0     0    0.0000             TIME OF LAST OBS
                                                        END OF HEADER
 01  3 22   8 13 30.0000000  0 11G 4G 5G 6G 9G14G20G24G25G29G30S72
  23958081.660   125900528.722        1650.338     23958085.930      98104338.023
      1286.009
  21053665.367   110637738.839        2013.908     21053666.062      86211255.987
      1569.284
  21418582.472   112555427.856       -2298.842     21418582.372      87705532.807
     -1791.306
  24692118.210   129757865.304        3710.519     24692124.259     101110024.000
      2891.318
  22618726.599   118862177.313        2462.128     22618728.204      92619845.475
      1918.543
  25434456.209   133658969.878         780.426     25434458.318     104149859.763
       608.110
  23095177.164   121365990.945        -683.196     23095181.314      94570970.618
      -532.363
  22847441.583   120064094.951       -2868.760     22847441.452      93556431.021
     -2235.366
  22214137.749   116736040.683        1652.672     22214138.069      90963086.183
      1287.798
  20055816.205   105394027.164          42.483     20055816.352      82125219.388
        33.107
  40272473.156   211633279.931          -5.677         0.000             0.000
         0.000
                                    .
                                    .
                                    .
```

Figure B.1: Adapted RINEX 2.10 header information and one epoch worth of data

```
#  2001  3 23  0 11 38.00000000   -99999     U IER85 FIT  BRD
## 1106 432698.00000000   250.00000000    81 0.7447685185185
+   25     2  3  4  5  6  7  8  9 10 13 14 17 18 20 21 23 24
+         25 26 27 28 29 30 31 72  0  0  0  0  0  0  0  0  0
+          0  0  0  0  0  0  0  0  0  0  0  0  0  0  0  0  0
+          0  0  0  0  0  0  0  0  0  0  0  0  0  0  0  0  0
+          0  0  0  0  0  0  0  0  0  0  0  0  0  0  0  0  0
++         0  0  0  0  0  0  0  0  0  0  0  0  0  0  0  0  0
++         0  0  0  0  0  0  0  0  0  0  0  0  0  0  0  0  0
++         0  0  0  0  0  0  0  0  0  0  0  0  0  0  0  0  0
++         0  0  0  0  0  0  0  0  0  0  0  0  0  0  0  0  0
++         0  0  0  0  0  0  0  0  0  0  0  0  0  0  0  0  0
%c cc cc ccc ccc cccc cccc cccc cccc ccccc ccccc ccccc ccccc
%c cc cc ccc ccc cccc cccc cccc cccc ccccc ccccc ccccc ccccc
%f  0.0000000  0.000000000  0.00000000000  0.000000000000000
%f  0.0000000  0.000000000  0.00000000000  0.000000000000000
%i    0    0    0    0       0       0       0       0        0
%i    0    0    0    0       0       0       0       0        0
/* ORBIT COMBINATION FROM GPS AND GEOSTATIONARY NAV PAYLOAD
/* GPS orbits are based on smoothed brd orbits
/* GEO orbits are based on integrated WAAS orbits
/* LCGR London Center for GNSS Resarch
*  2001  3 23  0 11 38.00000000 19
V  2  24246.277713   8623.137048  -6878.205365   -356.525246
V 72  24840.522596 -34078.076885      2.416100      0.049953
                              .
                              .
                              .
                              .
```

Figure B.2: Adapted SP3 file format header information and satellite parameters

```
     1.0            IONOSPHERE MAPS    GPS                 IONEX VERSION / TYPE
GPSEST V4.3         AIUB              31-MAR-01 22:04      PGM / RUN BY / DATE
CODE'S GLOBAL IONOSPHERE INFO FOR DAY 087, 2001           COMMENT
The global ionosphere maps are generated on a daily basis DESCRIPTION
by the Center for Orbit Determination in Europe (CODE),   DESCRIPTION
University of Berne, Switzerland.                          DESCRIPTION
The TEC is modeled with a spherical harmonic expansion up DESCRIPTION
to degree 12 and order 8 referring to a solar-geomagnetic DESCRIPTION
reference frame. The 12 2-hour sets of 149 ionosphere     DESCRIPTION
parameters per day are derived from GPS data of the global DESCRIPTION
IGS (International GPS Service) network.                   DESCRIPTION
Contact address: stefan.schaer@aiub.unibe.ch             DESCRIPTION
Web site: http://www.aiub.unibe.ch/ionosphere.html        DESCRIPTION
  2001     3    28     1     0     0                       EPOCH OF FIRST MAP
  2001     3    28    23     0     0                       EPOCH OF LAST MAP
  7200                                                     INTERVAL
    12                                                     # OF MAPS IN FILE
  COSZ                                                     MAPPING FUNCTION
    10.0                                                   ELEVATION CUTOFF
One-way carrier phase leveled to code                     OBSERVABLES USED
   139                                                     # OF STATIONS
    29                                                     # OF SATELLITES
  6371.0                                                   BASE RADIUS
     2                                                     MAP DIMENSION
   450.0 450.0    0.0                                      HGT1 / HGT2 / DHGT
    87.5 -87.5   -2.5                                      LAT1 / LAT2 / DLAT
  -180.0 180.0    5.0                                      LON1 / LON2 / DLON
    -1                                                     EXPONENT
TEC/RMS values in 0.1 TECU; 9999, if no value available   COMMENT
List of stations:                                         COMMENT
ajac albh algo alic alme amc2 ankr aoml areq artu auck bahr COMMENT
bako bili bogo bor1 brmu brus cas1 cedu chat chur coco cord COMMENT
cro1 dav1 delf dgar dour drao dubo ebre eisl fair flin fort COMMENT
gala glsv gode gold gope gras guam harb helg hers hflk hob2 COMMENT
hofn hrao ineg irkt jama joen joze karr kely kerg kir0 kodk COMMENT
kokb kosg kstu kunm kwj1 lama mac1 madr mag0 mar6 mas1 mate COMMENT
maw1 mcm4 mdo1 mdvo medi mets mkea monp nico nklg nlib not1 COMMENT
noum npld nrc1 nssp nya1 ohig onsa pdel penc petp pie1 pimo COMMENT
pol2 pots ptbb ramo reyk riog sant sch2 sele sey1 shao sjdv COMMENT
soda stjo suth suwn syog ters thti thu1 tidb tixi tlse tow2 COMMENT
tro1 urum usno usud vaas vil0 vill wes2 whit will wsrt wtzr COMMENT
wuhn yakz yar1 yell yssk zeck zimm                        COMMENT
DIFFERENTIAL CODE BIASES                                  START OF AUX DATA
    01    -0.979     0.037                                 PRN / BIAS / RMS
    02    -2.646     0.039                                 PRN / BIAS / RMS
                             .
                             .
    27    -0.508     0.037                                 PRN / BIAS / RMS
    28     3.629     0.039                                 PRN / BIAS / RMS
    29     1.366     0.039                                 PRN / BIAS / RMS
    30     1.531     0.038                                 PRN / BIAS / RMS
    31     0.605     0.038                                 PRN / BIAS / RMS
DCB values in ns; sum of all values constrained to zero   COMMENT
DIFFERENTIAL CODE BIASES                                  END OF AUX DATA
                                                          END OF HEADER
```

Figure B.3: IONEX data file: header information

```
   1                                                     START OF TEC MAP
2001     3    28     1     0     0                       EPOCH OF CURRENT MAP
  87.5-180.0 180.0     5.0 450.0                         LAT/LON1/LON2/DLON/H
155   154   154   154   153   153   152   151   151   150   149   148   147   146   145   144
143   141   140   139   138   136   135   134   133   132   131   130   129   128   127   127
126   126   126   126   126   126   126   127   127   128   129   130   131   132   133   134
136   137   138   140   141   142   144   145   146   147   149   150   151   152   152   153
154   154   155   155   155   155   155   155   155
  85.0-180.0 180.0     5.0 450.0                         LAT/LON1/LON2/DLON/H
166   165   164   164   163   162   161   160   159   158   156   155   154   152   150   148
146   144   142   140   137   135   132   129   127   124   122   120   118   116   114   113
112   111   110   110   110   110   111   112   113   114   116   118   120   122   125   127
130   133   135   138   141   144   146   149   151   154   156   158   160   162   163   164
165   166   167   167   167   167   167   166   166
  82.5-180.0 180.0     5.0 450.0                         LAT/LON1/LON2/DLON/H
174   173   172   171   170   169   168   167   166   165   164   163   161   160   158   155
153   150   146   143   139   135   131   127   123   119   115   111   108   105   102   100
 98    97    96    95    95    95    96    98    99   102   104   107   110   113   117   120
124   128   132   136   139   143   147   151   154   158   161   164   167   170   172   173
175   176   176   176   176   176   175   175   174
  80.0-180.0 180.0     5.0 450.0                         LAT/LON1/LON2/DLON/H
179   178   177   176   176   175   175   175   174   174   173   172   171   169   167   164
161   157   152   147   142   136   131   125   120   114   109   104   100    96    92    89
 87    85    83    82    82    83    84    86    88    91    94    98   102   105   110   114
118   122   127   131   136   140   145   149   154   158   163   167   170   174   177   179
181   182   182   183   182   182   181   180   179
  77.5-180.0 180.0     5.0 450.0                         LAT/LON1/LON2/DLON/H
183   182   182   182   182   182   183   183   184   184   183   183   182   180   177   174
169   164   158   151   144   137   129   122   115   109   103    98    93    88    84    81
 78    76    74    73    73    73    75    77    80    83    87    91    95    99   103   108
112   116   120   124   129   133   138   143   148   153   159   164   169   173   177   180
183   184   185   185   185   185   184   183   183
  75.0-180.0 180.0     5.0 450.0                         LAT/LON1/LON2/DLON/H
186   187   188   190   191   193   194   195   196   197   196   196   194   192   188   183
177   170   161   152   143   133   124   116   108   102    96    91    87    82    79    75
 72    70    68    67    66    67    69    71    74    77    81    86    90    94    98   102
106   109   113   116   120   124   128   133   138   144   150   157   163   169   174   178
181   183   185   186   186   186   186   186   186
  72.5-180.0 180.0     5.0 450.0                         LAT/LON1/LON2/DLON/H
192   195   198   201   205   208   210   212   213   213   212   211   208   204   198   192
183   173   161   149   137   125   114   105    97    91    87    83    81    78    75    72
 70    67    65    64    63    64    65    68    71    74    78    82    86    90    94    97
100   102   105   107   109   112   116   120   125   132   139   146   154   161   167   173
177   180   183   184   185   187   188   190   192
  70.0-180.0 180.0     5.0 450.0                         LAT/LON1/LON2/DLON/H
201   207   213   219   224   229   232   234   234   233   231   227   222   216   208   198
186   173   157   141   125   110    98    88    81    77    75    75    75    75    74    72
 70    67    65    64    63    64    65    67    70    73    76    80    83    86    89    92
 94    96    97    98   100   101   104   107   113   119   127   136   145   154   162   168
174   178   181   184   186   189   192   196   201
  67.5-180.0 180.0     5.0 450.0                         LAT/LON1/LON2/DLON/H
215   224   232   241   249   255   259   260   260   256   251   244   236   227   216   203
188   170   151   130   110    92    78    67    62    61    62    66    69    72    73    73
 71    69    67    66    65    66    67    69    71    73    75    77    80    82    85    87
 89    90    91    92    92    93    95    98   103   111   119   129   140   150   160   168
175   180   184   188   192   196   201   208   215
  65.0-180.0 180.0     5.0 450.0                         LAT/LON1/LON2/DLON/H
234   245   256   267   277   285   289   290   288   282   273   262   250   237   223   207
189   167   144   119    95    73    57    46    42    44    50    58    65    71    74    75
 74    72    70    69    69    70    71    73    74    75    75    75    76    77    79    82
 84    86    88    89    90    91    93    96   102   110   120   131   144   156   167   177
184   190   195   199   204   209   216   224   234
  62.5-180.0 180.0     5.0 450.0                         LAT/LON1/LON2/DLON/H
```

Figure B.4: IONEX data file: one epoch worth of ionospheric data

Appendix C

Curriculum vitae and publications

C.1 Curriculum vitae

Knut Sauer was born in Hoyerswerda (former East Germany) on 25 February 1971. In 1990 he finished his pre-university education in Johanngeorgenstadt. The first part of his university education was at the Technical University Clausthal in the field of Geological Survey. In 1997 he graduated in the field of geodetic network control and deformation analysis at the Technical University Freiberg(Saxony) in Germany.

In 1998 he worked as systems engineer for geographic information systems in Switzerland where he and Pia Schwarzwälder were married.

Between 1999 and 2002 he commenced his PhD studies at the Centre of Transport Studies at Imperial College London, where he was involved in several projects within the Galileo definition phase and the application of GPS within civil aviation.

In 2002 while finishing his PhD thesis he was employed in Switzerland as system engineer for optical network testing where he gained extensive experiences in the field of digital signal processing.

Since January 2003 he has been working as research and development engineer with TRIMBLE-TerraSat in Munich, Germany in the field of four carrier-ambiguity determination for the future GNSS Galileo.

C.2   Publications

Ochieng, W.Y., **Sauer, K.**, Cross, P.A., Sheridan, K. and Ilife, J. (2000), *"Performance potential of a combined Galileo/GPS navigation system"*, Final Report to Alcatel Space Industries, Toulouse

Ochieng, W.Y., **Sauer, K.**, Cross, P.A., Sheridan, K. and Ilife, J. (2000), *"Analysis of the GPS modernisation process"*, Final Report to Alcatel Space Industries, Toulouse

Ochieng, W.Y., **Sauer, K.**, Cross, P.A., Sheridan, K., Iliffe, J., Lannelongue, S., Ammour, N. and Petit, K. (2001), *"Potential performance levels of a combined Galileo/GPS navigation system"* in RIN Journal of Navigation Vol .54 Number 2, pp.186-197

Ochieng, W.Y. and **Sauer, K.** (2001), *"Urban Road Transport Navigation: Performance of GPS after Selective Availability (SA)"* Journal of Transportation Research - Part C on Emerging Technologies (January, 2001).

Sheridan, K., Ochieng, W.Y., **Sauer, K.**, Cross, P.A., Iliffe, J., Lannelongue, S., Ammour, N. and Petit, K., (2001), *"Performance potential of a combined Galileo/GPS navigation system"*, Proceedings of GNSS 2001 Seville, Spain; May 2001.

Ochieng, W.Y., **Sauer, K.**, Sheridan, K., Han, X., Cross, P.A., J., Lannelongue, S., Ammour, N. and Petit, K. (2002) *"An Assessment of the RAIM Performance of a Combined Galileo/GPS Navigation System using the Marginally Detectable Errors (MDE) Algorithm "*. GPS Solutions, Vol. 5, Number 3 2002 .

Sauer, K. , Ochieng, W.Y. (2002), *"Integrated use of GPS and EGNOS Carrier Phase Observations for High Precision Kinematic Positioning - first experiences"*, Proceedings of GNSS 2002 Copenhagen; May 2002

Sauer, K. , Ochieng, W.Y. (2002), *"Integrated use of GPS and EGNOS Carrier Phase Observations for High Precision Kinematic Positioning"*, Hong Kong Journal of Geospatial Engineering, Vol. 4 Number 1; June 2002

Ochieng, W.Y., **Sauer,K.**, Walsh, D., Griffin, S. and Denney, M. *"GPS Integrity and potential Impact on Aviation Safety"*, excepted for publication in RIN Journal of Navigation; January 2003

Sauer, K. , Ochieng, W.Y. (2002), *"Integrated use of GPS and EGNOS Carrier Phase Observations for High Precision Kinematic Positioning"*, Proceedings of the 15th International Meeting of the Satellite Division of the Institute of Navigation, September 25-27 2002, Portland Oregon